UNIVERSITY OF CALIFORNIA, SAN DIEGO

SAN DIEGO STATE UNIVERSITY

Microalgae Rupture Energy and Ultrasound Biomass Processing

A dissertation submitted in partial satisfaction of the requirements for the degree of Doctor of Philosophy

in

Engineering Sciences (Mechanical and Aerospace Engineering)

by

Rory James Klinger

Committee in charge:

University of California, San Diego

Professor Daniel Tartakovsky, Co-Chair
Professor Peter Asbeck

San Diego State University

Professor Temesgen Garoma, Co-Chair
Professor Asfaw Beyene
Professor Julio Valdes

2017

The Dissertation of Rory James Klinger is approved, and it is acceptable in quality and form for publication on microfilm and electronically:

Co-Chair

Co-Chair

University of California, San Diego

San Diego State University

2017

DEDICATION

To my wife Derlin and to my parents for their kindness and support.

EPIGRAPH

"Ever tried. Ever failed. No matter. Try again. Fail again. Fail better."

- Samuel Beckett

"Genius is patience."

- Isaac Newton

"Keep moving forward."

- Walt Disney

TABLE OF CONTENTS

SIGNATURE PAGE iii
DEDICATION iv
EPIGRAPH v
TABLE OF CONTENTS vi
LIST OF SYMBOLS ix
LIST OF FIGURES xiii
LIST OF TABLES xvi
ACKNOWLEDGEMENTS xviii
VITA xx
ABSTRACT OF THE DISSERTATION xxiv
Chapter 1 - Introduction 1
1.1 MOTIVATION 1
1.1.1 Energy Alternatives 2
1.1.2 Algae Biofuels 4
1.1.3 Processing and Co-Products 5
1.2 PRETREATMENT OF MICROALGAE BIOMASS 8
1.2.1 Pretreatment Taxonomy 9
1.2.2 Measures of Effectiveness 12
1.2.3 Optimization 18
1.2.4 Physical and Chemical Characteristics 20
1.2.5 Models of Physical and Chemical Effects 23
1.2.6 Mechanisms 24
1.3 OUTLINE AND CONTRIBUTIONS 25
Chapter 2 - Energy Requirements and Ultrasound Processing 28
2.1 CONSTITUTIVE MODEL OF CELL RUPTURE 28
2.1.1 Introduction 28
2.1.2 Conceptual Framework 30
2.1.3 Model Derivation 32
2.1.4 Derivation Outline 38
2.1.5 Generic Functions 40
2.1.6 Parameterization 45

2.1.7 Integrals and Model Synthesis 50
2.1.8 Calculation 52
2.1.9 Results and Discussion 54
2.1.10 Conclusions 56
2.2 Ultrasound System Calorimetry 57
2.2.1 Introduction 57
2.2.2 Theory 59
2.2.3 Experimental Approach 60
2.2.4 Materials and Methods 61
2.2.5 Results and Discussion 63
2.2.6 Conclusions 70
2.3 Ultrasound Processing of Chlorella vulgaris 72
2.3.1 Introduction 72
2.3.2 Experimental Approach 73
2.3.3 Materials and Methods 73
2.3.4 Results and Discussion 75
2.3.5 Conclusions 78
Chapter 3 - Sensitivity Analysis 80
3.1 Introduction 80
3.2 Sensitivity Analysis of Constitutive Model 81
3.2.1 Methods 81
3.2.2 Results and Discussion 83
3.2.3 Conclusions 90
3.3 Cell Diameter Measurement and Monte Carlo Simulations of Cell Strength 92
3.3.1 Materials and Methods 92
3.3.2 Results and Discussion 94
3.3.3 Conclusions 101
Chapter 4 - Growth Media Selection and Power Ultrasound Processing 102
4.1 Introduction 102
4.2 Materials and Methods 104
4.3 Results and Discussion 109
4.4 Conclusions 118
Chapter 5 - Theoretical Kinetics and Mechanism of Cell Disruption 120
5.1 Introduction 121
5.2 Reactor Model 122
5.3 Elementary Reaction Model 124

5.4 Reaction Mechanism and Critical Distance 129
5.5 Rate Constant Mapping 135
5.6 Prediction of Cavitation Rate 139
5.7 Treatment of PDF Inputs 141
5.8 Conclusions 142
Chapter 6 – Conclusions 144
6.1 Summary 144
6.2 Conclusions 145
6.3 Future Directions 149
Bibliography 150

LIST OF SYMBOLS

English Symbols

Symbol	Meaning	Units
a	Scaling factor	-
A_{cs}	Wall cross section area	m^2
$A_{cs,c}$	Cell cross sectional area	m^2
$A_{cs,int}$	Internal cross sectional area	m^2
b	Vertical axis intercept	-
b,c	Ellipse axial half lengths	m
C_c	Cell mass concentration	$kg \cdot m^{-3}$
$Circ_c$	Cell circumference	m
C_{vl}	Constant volume specific heat of the liquid	$J \cdot kg^{-1} \cdot {}^oC^{-1}$
D	Fraction of cells disrupted	-
d_c	Diameter of cell	m
e	Energy per volume solution	$J \cdot m^{-3}$
E_{90}	90^{th} percentile rupture energy	J
e_c	Energy per cell	J
e_{cw}	Energy per volume of cell wall	$J \cdot m^{-3}$
$e_{d,m}$	Energy per volume disrupted material	$J \cdot m^{-3}$
E_T	Total energy input	J
f	Frequency	Hz
$F_{c,ng}$	Fraction of unsuccessful cultures	-

f_f	Fraction of cells in suspension meeting f_s	-
f_s	Fraction of circumference separation	-
f_w	Mass fraction water	-
h	Offset distance	m
h	Horizontal shift	-
I_{RMS}	RMS current	A
k	Vertical shift	-
k	Cell disruption rate constant	m^{-3}
l	Length of a cylinder	m
l_c	Critical distance	m
M	Lumped parameter	-
m	Slope	-
$m_{c,d}$	Dry mass per cell	kg
M_k	Number rate of cell disruption	s^{-1}
N_c	Concentration of whole cells	m^{-3}
N_d	Concentration of disrupted cells	m^{-3}
N_o	Initial whole cell concentration	m^{-3}
N_p	Number of pure cultures	-
P	Power	W
P	Probability	-
p	Perimeter	m
$p(t)$	Driving pressure	Pa

$P_{apparent}$	Apparent power	V·A
p_b	Solvent vapor pressure	Pa
P_c	Internal pressure	$N \cdot m^{-2}$
P_{diss}	Power dissipated to solution	W
P_v	Vapor pressure	Pa
Q	Thermal energy	J
Q	Volumetric flow rate	$m^3 \cdot s^{-1}$
r	Intrinsic growth rate	d^{-1}
R, r	Radius	m
r_b	Radius of cavitation buble	m
t	Time	s
T	Temperature	ºC
T_{cw}	Wall thickness	m
TS_{cw}	Tensile strength	$N \cdot m^{-2}$
V	Volume	m^3
V_c	Volume of a cell	m^3
$V_{d,m}$	Volume of disrupted material	m^3
V_{RMS}	RMS voltage	V
x	Mole fraction	-
X	Extent of reaction	-
Y	Young's modulus	$N \cdot m^{-2}$
Y_{cw}	Young's modulus of the cell wall	$N \cdot m^{-2}$

Greek Symbols

Symbol	Meaning	Units
α	Material elongation fraction	-
β	e_{dm} scaling factor	-
ε	Strain	-
ε_f	Failure Strain	-
ε_m	Measured strain	-
ε_y	Yield strain	-
η	Efficiency	-
μ_l	Solvent viscosity	$kg \cdot m^{-1} \cdot s^{-1}$
ρ_c	Single cell bulk density, wet	$kg \cdot m^{-3}$
$\rho_{c,d}$	Single cell bulk density, dry	$kg \cdot m^{-3}$
ρ_{cw}	Cell wall material bulk density	$kg \cdot m^{-3}$
ρ_l	Solvent density	$kg \cdot m^{-3}$
σ	Stress	$N \cdot m^{-2}$
σ_y	Yield stress	$N \cdot m^{-2}$
ϕ	Cavitation rate	s^{-1}
ψ_c	Probability of critical interaction	-

LIST OF FIGURES

Figure 1.1 – Biorefinery process categories and their feed stocks. Adapted from [5, 9, 20, 22, 25-30] 7

Figure 1.2 – Pretreatment Methods. Adapted from [33, 35-40] 10

Figure 2.1 – Cell wall separation geometry and constitutive cell rupture model foundations 33

Figure 2.2 – Rupture energy model derivation outline 39

Figure 2.3 – Characteristic stress-strain curves and necking behavior 40

Figure 2.4 – Parameterized stress-strain curves: a) ductile, b) slightly ductile brittle, c) plastic, d) brittle, e) highly elastic 47

Figure 2.5 – Model output confirmation of parameterized stress strain curves 53

Figure 2.6 – Cumulative energy transferred to solution by Q55 sonotrode at setting of 100 using 1/8 inch microtip immersed1.5cm in specified volume of tap water and reactor. Horizontal error bars are one standard deviation of time lumped for visualization, but not for regression 64

Figure 2.7 – Categorization of reactors according to non-linear interactions 66

Figure 2.8 – Apparent power draw of Q55 sonotrode over full performance range using 1/8 inch microtip immersed 1.5cm in 500ml tap water reservoir 68

Figure 2.9 – Cumulative energy transferred to solution by Q55 sonotrode at setting of 100 using 1/8 inch microtip immersed1.5cm in 50ml in 50ml Kimble jacketed beaker using new and eroded sonotrode tips 69

Figure 2.10 – Cell disruption over time under power ultrasound 76

Figure 2.11 – First order empirical cell disruption model 77

Figure 2.12 – Model predicted versus measured marginal rupture energy per cell over time under power ultrasound treatment 78

Figure 3.1 – Constitutive model cell rupture energy versus cell diameter for 15 model variants: (a) assumed height of material at h = 100nm, (b) circumference fraction of material at $\alpha = 0.01$, (c) strain based fraction of material at $\varepsilon_f = 0.25$ 84

Figure 3.2 – Frequency distribution of cumulative order of influence of input scaling under 3 constitutive cell rupture energy model variants 86

Figure 3.3 – Cell rupture energy (J) output contours of constitutive cell rupture model over input space of cell diameter and failure strain: (a) assumed height model h = 100E-9m, (b) set fraction height model $\alpha = 0.01$. (c) strain based height model $f_s = 0.25$ 87

Figure 3.4 – Scatter plots of cell rupture energy versus tensile strength and versus wall thickness for linear elastic constitutive model with uniform random variation of all other inputs: (a and d) assumed height of material at h = 100nm, (b and e) circumference fraction of material at $\alpha = 0.01$, (c and f) strain based fraction of material at $\varepsilon_f = 0.25$ 88

Figure 3.5 – Scatter plots of cell rupture energy versus split fraction and versus failure strain for linear elastic constitutive model with uniform random variation of all other inputs: (a and d) assumed height of material at h = 100nm, (b and e) circumference fraction of material at $\alpha = 0.01$, (c and f) strain based fraction of material at $\varepsilon_f = 0.25$ 89

Figure 3.6 – Scatter plot of cell rupture energy versus cell diameter for linear elastic constitutive model with uniform random variation of all other inputs: (a) assumed height of material at h = 100nm, (b) circumference fraction of material at $\alpha = 0.01$, (c) strain based fraction of material at $\varepsilon_f = 0.25$ 90

Figure 3.7 – Graphical Q-Q test for normality of a) raw cell diameter distribution and b) log transformed cell diameter distribution 95

Figure 3.8 – Scatter plots of Monte Carlo simulation outputs for assumed normal distributions of all inputs: (a) assumed height of material at h=100E-9, (b) circumference fraction of material at $\alpha = 0.01$, (c) strain based fraction of material $\varepsilon_f = 0.25$. Cell diameter versus rupture energy plots are presented as representative of observed results 96

Figure 3.9 – Cumulative distribution functions of cell rupture energy for all Monte Carlo simulation outputs with fully assumed normal input distributions 97

Figure 3.10 – Scatter plots of Monte Carlo simulation outputs for measurement based cell diameter input. Cell diameter versus rupture energy plots are presented as representative of observed results: : (a) assumed height of material at h = 100nm, (b)

circumference fraction of material at $\alpha = 0.01$, (c) strain based fraction of material at $\varepsilon_f = 0.25$ 98

Figure 3.11 – Cumulative distribution functions of cell rupture energy for all Monte Carlo simulation outputs with measurement based cell diameter input distribution ... 98

Figure 3.12 – E_{90} values for cell rupture from Monte Carlo simulations. (prefixes: AH = assumed height; AF = assumed fraction; SB = strain based) (suffixes: LE = linear elastic; D = ductile; SDB = slightly ductile brittle; P = plastic; HE = highly elastic) . 99

Figure 4.1 – Sample spectrophotometric absorbance spectrum of *Chlorella vulgaris* grown in BBM medium 109

Figure 4.2 – Intrinsic growth rates (r) of *Chlorella vulgaris* grown in specified media. Sample size is indicated by n, defined as the number of cultures that reached an observable maximum growth rate within 31 days without crash due to contamination. Error bars are one standard deviation 110

Figure 4.3 – Power ultrasound effect on % viability of *Chlorella vulgaris* grown in specified media. Change in *Chlorella vulgaris* % cell viability as PI fluorescence after power ultrasound treatment. Error bars are one standard deviation. Minimum viability of cultures prior to treatment was 98.2% 114

Figure 4.4 – Solvation of *Chlorella vulgaris* COD in specified media by power ultrasound. Soluble fraction of COD before and after power ultrasound treatment of 50ml volume. Error bars are one standard deviation 114

Figure 5.1 – Cell disruption rate constant over frequency and cavitation rate 136

Figure 5.2 – Cell disruption rate constant over bubble radius and cavitation rate..... 137

Figure 5.3 – Cell disruption rate constant over cell radius and cavitation rate 137

Figure 5.4 – Cell disruption rate constant over bubble radius and frequency 138

Figure 5.5 – Cell disruption rate constant over cell radius and frequency 138

Figure 5.6 – Cell disruption rate constant over cell radius and bubble radius..... 139

Figure 5.7 – Cavitation rate as a function of bubble radius and streaming flow rate for known reactor rate constant 141

LIST OF TABLES

Table 2.1 – Index notation key for Equations 2.3 44

Table 2.2 – Inputs for model calculation 53

Table 2.3 – Spherical Cells Solution Rupture Energy [(J/m^3) / (pJ/cell)]. (Bold indicates values within a factor of 2 of the AFM measured value, corrected for cell diameter.) 54

Table 2.4 – Cylindrical Cells Solution Rupture Energy [(J/m^3) / (pJ/cell)] 54

Table 2.5 – Rupture Energy per Cell Comparison. (d_c = 8.84μm) 55

Table 2.6 – Experimental Design 63

Table 2.7 – Linear regression coefficients for cumulative energy transfer and average power transfer efficiency (η). Power transfer to solution is given by the slope, and mixing delay is given by the x-intercept 67

Table 2.8 – Linear regression coefficients for cumulative energy transfer and average power transfer efficiency (η). Power transfer to solution is given by the slope, and mixing delay is given by the x-intercept 69

Table 3.1 – Input Ranges for Sensitivity Analysis 82

Table 3.2 – Model Sensitivity Order by Variable in Volume of Disrupted Material .. 83

Table 3.3 – Simplified model order of dependence on inputs: TS_{cw} / T_{cw} / f_s / ε_f / d_c ... 84

Table 3.4 – Monte Carlo Simulation Input Distribution Descriptors 94

Table 4.1 – Intrinsic growth rates and frequency of contamination and non-growth of *Chlorella vulgaris* in specified media. The mean intrinsic growth rate (r) is presented ± one standard deviation. $F_{c,ng}$ is the combined frequency of contamination and non-growth. N_p is the number of algae dominant culture growths 112

Table 4.2 – Growth Rate, Biomass Yield, and Energy Conversion Potential of *Chlorella vulgaris* in specified media. Values are mean ± one standard deviation ... 113

Table 4.3 – Paired differences of change in % viability of *Chlorella vulgaris* after power ultrasound between growth media. Read table as 'column' shows 'value' higher

change in % viability than ‘row’. Values are the mean difference ± Fisher’s LSD 95% confidence intervals..... 115

Table 4.4 – Significant differences between media in COD solvation by power ultrasound. Values are mean difference ± Fisher’s LSD 95% confidence interval ... 116

Table 4.5 – *Chlorella vulgaris* culture end conditions. pH, EC, and ORP of Chlorella vulgaris cultures at the end of 31 days growth in selected media. Values are mean ± one standard deviation..... 117

ACKNOWLEDGEMENTS

I would like to thank my advisor, Dr. Temesgen Garoma, for his support and encouragement of my independence in pursuing this work. He, the rest of my committee members, and many fellow students, staff, and faculty members at both SDSU and UCSD provided invaluable support and guidance at key points in my personal and professional development over the course of my studies, research, and teaching work. I would not have made it through without them.

Chapter 2, in part, has been submitted for publication of the material as it may appear in Biomass & Bioenergy, 2017, Klinger, Rory; Garoma, Temesgen, Elsevier, 2017; and in Ultrasonics Sonochemistry, 2017, Klinger, Rory; Garoma, Temesgen, Elsevier, 2017. The dissertation author was the primary investigator and author of this material.

Chapter 3, in part, is currently being prepared for submission for publication of the material. Klinger, Rory; Garoma, Temesgen. The dissertation author was the primary investigator and author of this material.

Chapter 4, in full, has been accepted for publication of the material as it will appear in Proceedings of ECOS 2017 - 30th International Conference on Efficiency, Cost, Optimization, Simulation and Environmental Impact of Energy Systems, 2017. Klinger, Rory; Garoma, Temesgen. The dissertation author was the primary investigator and author of this material.

Chapter 5, in part, has been submitted for publication of the material as it may appear in Ultrasonics Sonochemistry, 2017, Klinger, Rory; Garoma, Temesgen,

Elsevier, 2017. The dissertation author was the primary investigator and author of this material.

VITA

2004-2005	Process Control Intern, Metro Biosolids Center, San Diego, CA
2005	Bachelor of Science, Biology and Environmental Systems, University of California San Diego, San Diego, CA
2006	Junior Environmental Scientist, Lee International, Sacramento, CA
2006-2009	Environmental Scientist and Technician, BBC Environmental, San Diego, CA
2010	Outstanding Leader Award, Engineers Without Borders, San Diego State University
2011	Master of Science, Civil Engineering (Environmental Engineering), San Diego State University, San Diego, CA
2011-2016	Teaching Associate, San Diego State University, San Diego, CA
2017	Doctor of Philosophy, Engineering Sciences (Mechanical and Aerospace Engineering), University of California, San Diego and San Diego State University, San Diego, CA

PEER REVIEWED PUBLICATIONS

Klinger, R.; Garoma, T., 2017. Growth media selection: the relationship between growth medium used for microalgal cultivation and the susceptibility of cells to disruption by low frequency power ultrasound. In *Proceedings of ECOS 2017 - 30th International Conference on Efficiency, Cost, Optimisation, Simulation and Environmental Impact of Energy Systems*. July 2-July 6, 2017, San Diego, California, USA. (Accepted)

Klinger, R.; Garoma, T., 2017. Constitutive Models of Algal Cell Rupture: Derivation and Inference of Material Behavior. *Biomass & Bioenergy*. (Under Review)

Klinger, R.; Garoma, T., 2017. Energy perspectives on power ultrasound test systems and ultrasound processing of *Chlorella vulgaris*. *Ultrasonics Sonochemistry*. (Under Review)

Klinger, R.; Garoma, T., 2017. Theoretical kinetics and mechanism of cell disruption under ultrasound induced cavitation. *Ultrasonics Sonochemistry*. (Under Review)

Klinger, R.; Garoma, T., 2017. Sensitivity analysis of a constitutive model of cell rupture with input measurement and Monte Carlo simulations of cell strength. (In Progress)

Garoma, T.; Matsumoto, S.A.; Wu, Y.; Klinger, R., 2010. Removal of Bisphenol A and its Reaction-Intermediates from Aqueous Solution by Ozonation. *Ozone Science & Engineering* 32, no. 5 (2010): 338-343.

PRESENTATIONS

Klinger, R; Garoma, T., 2016. Power ultrasound treatment of microalgae for energy generation and growth media effects on performance. 6th International Conference on Algal Biomass, Biofuels and Bioproducts, June 26-29, 2016, San Diego, California.

Klinger, R., 2016. Power ultrasound treatment of microalgae for energy generation and growth media effects on performance. San Diego State University Student Research Symposium, March 4-5, 2016, San Diego, California.

Klinger, R., 2015. Research Based Teaching in Environmental Engineering – Resources, Tools, and Practices. ASCE-EWRI 2015 World Environmental and Water Resources Congress, May 17-21, 2015, Austin, Texas.

Klinger, R., 2015. Outcome Mapping: A Bloom's Taxonomy Heat Map for Integrated and Consistent Student, Instructor, and Course Assessment. CIRTL Forum 2015 Center for the Integration of Research, Teaching and Learning, April 12-14, 2015, College Station, Texas.

Klinger, R., 2015. Separation of turbidity and chemical absorbance signals from UV-Vis absorbance spectra of *Chlorella vulgaris* to monitor stability of cultures during storage. San Diego State University Student Research Symposium, March 6-7, 2015, San Diego, California.

Klinger, R., 2014. Cell disruption efficiency of biomass pretreatment processes as a function of theoretical specific energy requirements. San Diego State University and University of California, San Diego Joint Doctoral Program Research Symposium, December 5, 2014, San Diego, California.

Klinger, R., 2012. Algae Biorefinery Process: Development and Optimization of Stochastic Model with Broader Applications. San Diego State University and University of California, San Diego Joint Doctoral Program Research Symposium, December 4, 2012, San Diego, California.

Klinger, R.; Garoma, T., 2011. Effect of Environmental Conditions on the Development of Antibiotic Resistance in *E. coli* Exposed to Trace Levels of Ciprofloxacin. ASCE-EWRI 2011 World Environmental and Water Resources Congress, May 22-26, 2011, Palm Springs, California.

Klinger, R., 2011. Ciprofloxacin Contamination of Natural Waters: Developing Pollution Limits to Minimize Environmental Reservoirs of New Antibiotic Resistance. San Diego State University Student Research Symposium, March 4-5, 2011, San Diego, California.

Garoma, T.; Klinger R.; Allen M., 2010. Application of Ozonation for Oxidation of Micropollutants from Aqueous Solutions. The 16th International Conference on Advanced Oxidation Technologies for Water and Air Remediation, November 15-18, 2010, San Diego, California.

OTHER WORKS

Chirnside, A.E.M.; Kulkarni, T.S.; Hart, M.; Rose, S.V.; Klinger, R. 2017. 2014 Duke Energy Dan River Steam Station Coal Ash Spill - Eden, NC - Part IV. *EWRI Currents* 19, no. 1 (2017): 4-10.

Chirnside, A.E.M.; Kulkarni, T.S.; Hart, M.; Klinger, R. 2016. 2014 Duke Energy Dan River Steam Station Coal Ash Spill - Eden, NC - Part III. *EWRI Currents* 18, no. 3 (2016): 4-9.

Klinger, R.; Chirnside, A.E.M.; Kulkarni, T.S., 2016. 2014 Duke Energy Dan River Steam Station Coal Ash Spill - Eden, NC - Part II. *EWRI Currents* 18, no. 2 (2016): 6-10.

Klinger, R.; Gunsch, C.K.; Churnside, A.E.M., 2016. Coal and Coal Ash: Real and Potential Hazards to Environmental Health and Water Quality. *EWRI Currents* 18, no. 1 (2016): 4-5.

Klinger, R., 2011. Investigation of Resistance Development from Residual Contamination of Ciprofloxacin (Master's Thesis). San Diego State University, San Diego, CA.

Klinger, R. (Ed.) 2011. Community Needs Assessments, Dominican Republic. Humanitarians and Sustainability, San Diego State University, San Diego, CA.

FIELDS OF STUDY

Major Field: Environmental Engineering

Studies in: Environmental Biotechnology, Environmental Process Modeling, Environmental Hydrology, Aqueous Chemistry, Applied Mathematics, Numerical Methods, and Fluid Mechanics.

ABSTRACT OF THE DISSERTATION

Microalgae Rupture Energy and Ultrasound Biomass Processing

by

Rory James Klinger

Doctor of Philosophy in Engineering Sciences

(Mechanical and Aerospace Engineering)

University of California, San Diego, 2017
San Diego State University, 2017

Professor Temesgen Garoma, Co-Chair
Professor Daniel Tartakovsky, Co-Chair

Continually rising energy needs in conjunction with negative externalities of fossil fuel use demand the diversification of energy resources. However, fossil hydrocarbons are also used as raw materials for a vast web of manufacturing of

industrial and consumer goods. The use of plant based raw materials as substitutes for fossil materials in fuels and manufacturing has been demonstrated successfully, and microalgae are an extremely diverse and promising resource in this category. One of the chief challenges in the implementation of a bio-economy is efficient processing and conversion of biomass to platform chemicals. In order to maximize extraction efficiency, pretreatment is employed to effect cell rupture. Many pretreatment processes have been implemented using empirical operating curves, but the fundamental energy requirements of the cell disruption process have not been thoroughly explored. To fill this void, a constitutive model of cell rupture energy is derived here and implemented for low frequency power ultrasound processing of *Chlorella vulgaris*. A sensitivity analysis of the constitutive model is performed, identifying cell diameter as a high sensitivity input. Measured distribution of microalgae cell diameters is then used as a fixed input to Monte Carlo simulations of cell rupture energy from the constitutive model. The influence of growth media on microalgal growth rate is then investigated, and the resultant biomass subjected to power ultrasound processing to determine the effect of media choice on processing efficiency. The theoretical kinetics of cell rupture via power ultrasound induced cavitation is developed next. A reactor model is introduced to convert reactor kinetics to reaction zone kinetics. An elementary reaction model is then developed in the context of the constitutive model, leading to the introduction of an alternative reaction mechanism employing a critical distance parameter to capture the relative energies and proximity of cells and cavitation bubbles. This reaction mechanism is extended to generate an explicit expression for the cell disruption first order rate constant in terms

of cell properties and power ultrasound operating parameters. This rate constant is mapped over the parameter space, then used to back-calculate cavitation rate, and finally extended to incorporate PDF parameter inputs.

Chapter 1 - **Introduction**

1.1 Motivation

Commoditized energy is a large part of the global economy and essential to modern everyday living. One part of securing the future of our energy driven society is the exploration of alternative fuels. An essential part of the biofuels branch of this exploration is the processing of microalgae biomass.

The United States (US) Department of Energy (DOE) estimates global energy use to have been 553 $x10^{18}$ J/yr in 2010, and projects it will reach 865 $x10^{18}$ J/yr in 2040 [1]. The US used 104 $x10^{18}$ J/yr in 2010 [2] and is projected to reach 112 $x10^{18}$ J/yr in 2040 [3]. This usage is segregated into sectors of: residential (21.2%), commercial (18.5%), industrial (32.1%), and transportation (28.2%) [3].

In 2012, the sources of energy providing for total US usage to these sectors were: petroleum and other liquids (37.7%), natural gas (27.6%), coal (18.2%), nuclear (8.47%), hydropower (2.81%), biomass (2.66%), other renewable energy (2.07%), and other sources (0.41%) [3].

The fossil resources that make up 83.5% of these energy sources are decreasing in availability (relative to increasing demand), stability, and extractability for a variety of reasons; and sources of the remaining balance each face their own

unique obstacles to fulfilling existing and future energy and material demands within economic, political, and environmental constraints [3].

1.1.1 Energy Alternatives

The resounding conclusion from many energy analyses has been that no single energy source will emerge as a predominant solution moving forward [3-5]. Thus a diverse set of energy solutions are required, including: conventional fossil fuel resources, new fossil fuel extraction technologies, nuclear power, alternative fuels, biofuels, alternative energy systems, carbon capture and sequestration, and efficiency measures in transportation, lighting, appliances, building codes, and industrial processes [6, 7].

Because of the projected decreases in availability relative to growing demand and increases in volatility of fossil fuel sources, campaigns have focused on replacing them with domestically produced non-fossil fuel and energy sources. However, the rate of increase in overall energy demand outpaces the rate of increase in capacity of non-fossil energy, so not only does the consumption of fossil fuels not decrease; it continues to increase, albeit at a slower rate than it otherwise would. These non-fossil energy sources include both direct power generation and solid, liquid, and gas fuels derived from renewable sources.

Direct power generation has the most potential to displace fossil fuel consumption by replacing the combustion of coal to generate electricity. Renewable energy sources that directly produce electricity in stationary plants include: solar, wind, hydro, tidal, geothermal, and nuclear (a non-renewable mineral source) [8].

While natural gas is increasing its market share as the fuel of choice for electricity generation, coal is still the largest fuel source for this purpose [3]. Renewable resources can also be tapped to produce fuels that take the place of fossil fuels in these stationary combustion plants (hydrogen, biomass, and biogas) [8].

Renewable fuels and direct power generation are also used in mobile platforms, most significantly in transportation. Because these fuels are "better defined by their performance specifications than by the sum of specific molecules," [5] they can in some cases be engineered to be direct drop-in substitutes for fossil fuels, with no required or minor equipment alterations. These include: biodiesel, bio-jet fuel, ethanol, and bio-gasoline.

While the most significant displacement of fossil fuels can be accomplished through efficiency increases and grid-scale renewable electricity generation, global transportation is a significant fraction of energy demand [1]. Transportation runs predominantly on an existing liquid fuel infrastructure. The efficiencies inherent in utilizing existing infrastructure make renewable liquid fuels worth pursuing; and biologically derived fuels comprise a large sector under investigation.

During the late 20th century, liquid biofuels production emphasized corn based ethanol, cellulosic ethanol, biodiesel, and bio-jet fuel. Controversial aspects of food crop based ethanol and technical difficulties of cellulosic ethanol led to a limiting of their production. Biodiesel and bio-jet fuel gained only limited adoption in boutique and military test applications. In the early 21st century, focus has shifted away from biofuels that are largely used in mixes with petroleum based fuels (such as those listed

above), and more toward drop-in purely biologically based substitutes for liquid petroleum [9, 10]. The keys to this shift have been to 1) focus on bio-oil extraction/generation rather than fermentation and 2) transition to high density aquatic biomass production rather than land based crop production [5, 9, 11]. The crop that fits these requirements is microalgae.

1.1.2 Algae Biofuels

Investigations into the use of algae in fuels in the US began in the middle of the 20th century, with the investigation of their use to produce methane via anaerobic digestion [12, 13] under the DOE Marine Biomass Program [5]. From 1968 to 1990, the feasibility of cultivating, harvesting, and anaerobically digesting macroalgae (California kelp) to produce methane as a substitute for natural gas was investigated. The conclusion was that this process would not be cost-competitive with fossil based natural gas at the time of the study [14].

Spurred forward by the OPEC oil embargo, investigation into algae as a feedstock for biofuels had a major acceleration in the United States in the 1970s with the Aquatic Species Program. This program cataloged, characterized, and preserved cultures of over 3,000 microalgae species from the continental US with the goal of identifying those species with potential for biofuels development. The initial focus of the program was on hydrogen production, but switched to biodiesel (liquid fuels) in the 1980's. The discovery of oil droplet accumulation in algae cells under certain conditions had been made in the 1940's, with further investigations in the 50's and 60's, but this phenomenon wasn't linked to energy production until the 1970's [5].

The results of the Aquatic Species Program (1978 - 1996) were summarized in the program closeout report [15], and created the foundation for many ongoing investigations and commercial developments.

In 2007 the DOE Renewable Fuel Standards increased volumes of renewable liquid fuels required in the national blend over time. Towards accomplishing these goals, a major step forward was the National Algae Biofuels Technology Roadmap [5]. This report brought together all of the compartments of algae biofuels production, defining the state of technology and acting as a guide for scientific, engineering, policy, and economic collaboration to fill the gaps in solutions to make algae based biofuels viable.

In 2012 the IEA/OECD Renewable Energy Division (RED) determined that algae biomass was not sufficiently viable at the time to be considered in short term international energy decisions, but rather something to be encouraged for the future [16]. More recent efforts have emphasized integrating processes to maximize the net energy of the production chain. However, significant questions remain, including the operational details and limits of the component processes [17].

1.1.3 Processing and Co-Products

One approach to improving viability is expanding the value chain to co-products. A few of the additional materials produced from biomass include: oils, plastics, nutritional supplements, pharmaceuticals, foods, building materials, dyes, and fertilizers. The intersection in the production lines of fuels and co-products lies at a common set of source materials. In a bio-refinery, biomass can be used to produce

syn-gas (CO and H_2) and some of the same platform chemicals that have traditionally been extracted from petroleum. This allows the production of bio-plastics, bio-oils, and some biofuels; things that would otherwise have been produced using petroleum as feedstock [18-22].

Initiatives to replace fossil fuels with biofuels have recently become more comprehensive. Recognizing the variety of products produced from crude oil, efforts have begun to focus on "replacing the whole barrel" of crude oil by making biologically based crude oil replacements as "drop-in" solutions that can be directly substituted in existing infrastructure [9].

Bio-refinery and selected associated technologies for energy extraction and refinement are shown in Figure 1.1: liquefaction [22], gasification [18-20, 22, 23], anaerobic digestion [18, 20, 23], fermentation [18-20, 22, 23], hydrothermal carbonization[24], pyrolysis [18-20, 22, 23], and oil extraction [18, 19, 22].

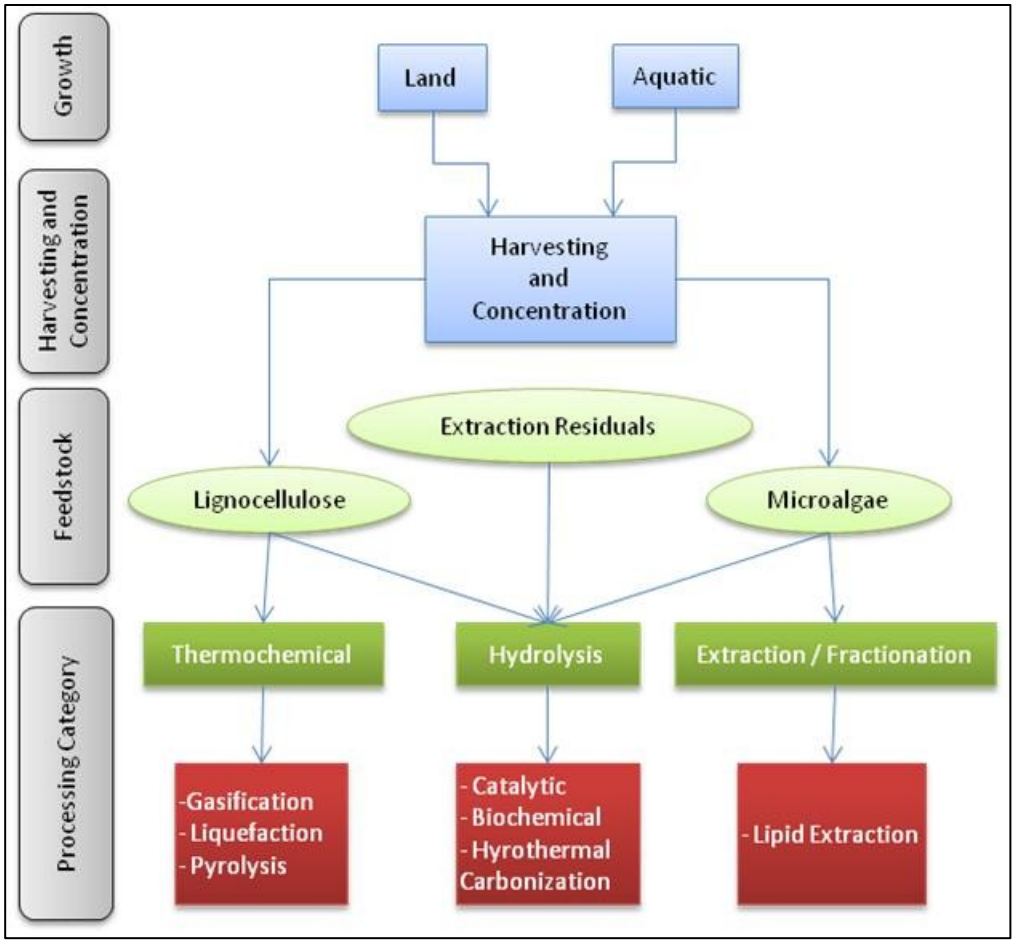

Figure 1.1 – Biorefinery process categories and their feed stocks. Adapted from [5, 9, 20, 22, 25-30]

After processing and extraction is complete, there exists a significant amount of reject material. In the case of chemical extraction, this reject material will in most cases be contaminated by extraction solvents. This contamination renders the material unusable for most purposes without further treatment, and investigations are underway to avoid this by the use of green solvents, non-solvent extraction processes, or whole cell utilization [9].

Waste stream challenges notwithstanding, the most significant challenges lie in the stages that occur prior to refining: growth; harvesting and dewatering; and pretreatment and extraction.

Among these 3 high potential areas, the pretreatment of microalgae biomass shows significant promise to increase the efficiency of harvesting of cell constituent materials. The investigation of technical aspects of this processing step has the potential to contribute significantly and positively to the techno-economic analyses (TEA) and energy return on investment (EROI) that are used to evaluate the viability of biofuels process trains [5, 19, 31, 32].

1.2 Pretreatment of Microalgae Biomass

This section presents a literature review summarizing the state of the field of pretreatment applied to microalgae biomass processing for biofuels production. The diversity of available pretreatments is introduced, and methods for their analysis are explored.

Mechanical oil extraction processes used for seed oil crops (i.e. presses) are ineffective on microalgae for the simple reason that the algae are so small [33]. Chemical methods of oil extraction compete with conflicting properties of microalgae. Those with high lipid content tend to have strong cell walls that keep the oil within the cell, and those with weak cellular structures tend to have low lipid fractions [34]. In order to access the oil within the cells of those tougher strains, the cells must be weakened or ruptured with a pretreatment step. Many pretreatment processes have

been developed, but their effectiveness is directly tied to how well they are customized to the biomass input.

1.2.1 Pretreatment Taxonomy

The design objective of biomass pretreatment is a mechanical failure of the cell wall and membrane. This objective can be accomplished with mechanical and/or non-mechanical mechanisms. The taxonomy of cell disruption technologies (Figure 1.2) begins with this distinction between mechanical and non-mechanical methods.

Mechanical methods of cell disruption are characterized by the direct application of surface force as solid and liquid shear. Three methods that fall into the solid shear category are bead milling, expeller pressing, and grinding with a mortar and pestle. Liquid shear methods are grouped here by the creation of highly localized pressure and velocity gradients within a fluid. These can be present alone, or they can be combined with a solid surface on which materials in the fluid impinge. Four groups of processes in this classification are homogenization, cavitation, microfluidization, and French press.

Non-mechanical methods of cell disruption are more diverse, being characterized by the absence of direct application of force as a surface force. These can be identified as the modification of the cells' environment to impart new, or take advantage of existing, body forces. These body forces then translate to surface forces in the context of a closed surface in local tension or compression, namely the cell wall and membrane. These non-mechanical methods can be categorized as: electromagnetic, thermodynamic, pressure, chemical, and biological.

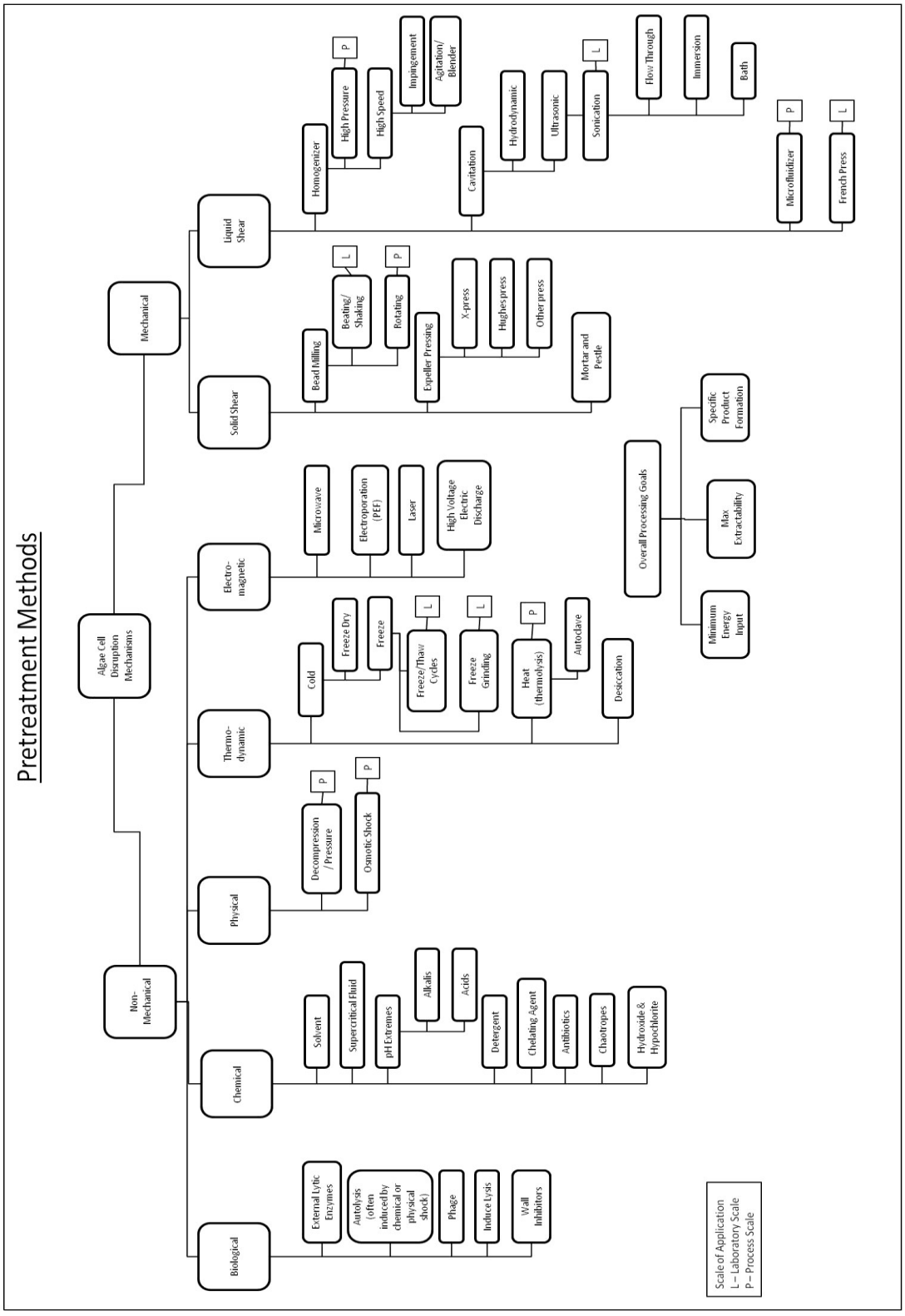

Figure 1.2 – Pretreatment Methods. Adapted from [33, 35-40]

Pretreatment and microalgae combinations are nearly as diverse as the number of papers in the literature on the subject. Many pretreatments are applied simply as a method of preparing the sample for analysis. Two of the most prevalent pretreatment methods are freeze drying [41-56] and grinding [41, 44-46, 48, 51, 52, 54, 55, 57, 58]. However, these two methods are the standard sample preparation steps for extraction of lipids by supercritical fluid. The next most prevalent method is sonication [42, 46, 57, 59-71], followed by microwave [46, 58, 60, 66, 67, 72, 73], thermal [46, 67, 68, 70, 73-77], high pressure homogenization [63, 64, 78, 79], and autoclaving [60, 61, 80]. All of these methods disrupt cells, and their appropriateness is application dependent.

The pretreatments applied to microalgae are selected based on the desired extraction product. A significant portion of the literature related to microalgae pretreatment for extraction surrounds food processing and nutritional supplement extraction. These extraction products are sensitive to contamination and modification by the pretreatment process [50]. The cost and efficiency of the pretreatment process is also less of a determinant of viability for the production of these products. Nutritional supplements and similar products can command a high price on the market, justifying the expense of inefficient extraction methods. When considering fuel products extraction, the contamination and byproducts limitations are somewhat removed. Fuel products are also awash in a sea of alternatives with low immediate financial cost, making the efficiency of their extraction a prime driver of their

viability. Excluding these non-fuel extraction studies decreases the variety of pretreatments considerably.

1.2.2 Measures of Effectiveness

As the extracted product varies, so too do measures of effectiveness in microalgae pretreatment. Outputs and inputs are measured directly, and calculated parameters have been useful for extrapolation in the context of the whole processing chain.

The extraction products considered when making energy products from microalgae include oil products, methane gas from anaerobic digestion, and ethanol from fermentation. As was noted above, the extraction of oil products for feed into biorefineries is a dominating force in microalgae energy research. Accordingly, much of the reviewed literature focuses on these products, which occur in the lipid fraction of the cell. The products that can be formed depend not only on the total lipid yield, but also on the composition of that lipid.

The total lipid yield is measured in several ways in the literature. Gravimetrically, the crude lipid yield is measured as either percent of ash free dry weight of algae cell mass [41, 62] or, more simply, as percent of dry weight of algae cell mass [42, 45-47, 57, 60, 61, 72-74, 81]. This crude lipid yield has also been measured by a calibrated spectrophotometric absorbance from 200nm to 800nm [64]. When the composition of the lipid is considered, a lipid yield can be calculated as the sum of the concentrations of individual lipid components or their derivatives. For fatty acid methyl esters (FAME), the feedstock to biodiesel production, this yield has been

measured by gas chromatography (GC) with either flame ionization detector (GC-FID) [41, 43, 66, 82] or mass spectrometer (GC-MS) [58, 81]. Di- and Tri-acyl-glyceride [57, 73] and soluble volatile fatty acids (VFA) [68] yields have also been determined via GC-FID. Triacylglycerol yield has been determined by liquid chromatography (LC) with mass spectrometry (LC-MS) [41]. Triglyceride yield has been determined by both nuclear magnetic resonance (H-NMR) [45] and LC with triple-quadrupole mass spectrometry (LC-QqQ MS) [64]. Oil yields have been described by a first order extraction curve [73].

The FAME profile is quantified to determine appropriateness of the lipid fraction for a certain application, but in many cases this is done without the calculation of total yield from the profile. These FAME profiles are measured by either GC-FID [41, 43, 46, 47, 57, 60-62, 66, 82] or GC-MS [58, 72, 73, 81]. The triacylglycerol profile has been determined via LC-MS [41] and the triglyceride profile via LC-QqQ MS [64].

The same distinction between yield and composition is made when considering methane in biogas generated by anaerobic digestion of microalgae biomass. Biogas yields are measured as a volume of biogas generated [83] or the change in headspace pressure [68, 70] in laboratory bioreactors. The biogas composition has been measured by GC with thermal conductivity detector (GC-TCD) [68, 84] and as methane fraction via methane exclusion by NaOH reaction [83].

Bioethanol yield from fermentation of microalgae biomass has been measured by both GC-FID [75] and high pressure liquid chromatography (HPLC) [76, 85].

Cell disruption is considered a very important preliminary step for both chemical extraction and biochemical transformation of products from microalgae. As such, the performance of pretreatment methods can be measured as their effectiveness in rupturing cells. The ability of the cell wall and membrane to maintain the separation of intracellular and extracellular products is the fundamental underlying behavior. However, the measurements of cell disruption correspond to degrees of not only this behavior, but also of the availability of cell materials for extraction. This degree of availability is the more significant indicator of performance, leading many studies of cell disruption to continue treatment beyond the threshold of cell permeability all the way to complete cell material disintegration.

Cell permeability can be measured by absorbance of an indicator dye. This has been performed with trypan blue [83], where stained cells can be counted in a hemocytometer on a standard light microscope. SYTOX Green staining has also been used, where cell counts are performed by dual fluorescence on a light microscope with a fluorescein filter [68] or via fluorescence quantified by either a fluorescence microscope or flow cytometry [82].

Cell permeability is an indicator of cell death, or viability. This has been approached from the perspective of growth inhibition, measured as decreased growth in subsequent cultures [59] and as the reduction of observed colony forming units (CFU) on inoculated plates [82].

Contents released from the cell are good indicators of failure of the cell wall and have been analyzed without further extraction by employing optical methods.

Lipid released from microalgae after treatment has been measured as fluorescence after staining with Nile Red dye [65]. A corollary performed in that study was the prediction of lipid extractability via spectrophotometric absorbance of pigments released from the microalgae [65]. Microcystin release has been quantified [59], and protein release has been measured via colorimetry using the Bradford reagent [78]. The release of general intracellular contents has been measured as UV absorbance at 260nm [78].

The degree of disintegration of cell material is usually an excellent indicator of availability of cell contents for further processing. Large qualitative changes in cell wall integrity are observable directly via light microscope [41, 65] and TEM [58, 72, 82]; and in cases of whole cell disintegration can be quantified as the reduction in the number of whole cells counted in either a hemocytometer [59, 63, 64, 78] or bright field microscope [67, 82]. The qualitative changes in the cell surface have been quantified for comparison as the fractal dimension (box-counting dimension) of binarized scanning electron micrograph (SEM) images of pretreated cells [72]. The degree of disruption in bulk solution has been measured as turbidity via absorbance at 750nm [78]. The size distribution of remaining particles, including cells and debris, has been measured using the electric sensing zone method in a Coulter counter [41] and optically via laser diffraction [68, 78] and dynamic light scattering [63]. However, the laser diffraction determinations are discounted by their authors based on the likelihood of false assumptions of cell shape after disruption.

Cell disruption has been described by a first order kinetic model [86]. The first order disruption rate constant has been measured in an algae biofuels context [64], however this analysis does not appear frequently in the literature.

Pretreatments can be implemented to improve performance at various stages of biomass processing. The majority of the reviewed literature that measured parameters not having directly to do with cell disruption or extraction had to do with biochemical conversion. These additional parameters affect the metabolism of microorganisms employed, and so are important predictors of conversion performance. Hence the effect of pretreatment on these parameters is also important. The effect has been studied for: total solids (TS) [68, 70], volatile solids (VS) [68, 70], total Kjeldal nitrogen (TKN) [68], chemical oxygen demand (COD) [68, 70], soluble chemical oxygen demand (SCOD) [68, 70, 82, 83], ammonium via ion chromatography (IC-conductivity) [68], phosphate via IC-conductivity [68], sugar profile via HPLC [75, 76], and reducing sugar concentration via phenol-sulfuric acid method as UV absorbance [75]. The effect of pretreatment of microalgae biomass on moisture removal rate has also been investigated [61].

When considering the viability of energy products, the energy input required is important as both a practical concern as financial cost and a more theoretical concern related to net energy. Several studies have measured or calculated energy inputs for pretreatment. Three convenient forms for analysis are: mechanical energy [58], thermal energy [58, 72, 83], and total extraction energy [58].

Energy inputs are all calculated values intended for use in either process comparison or extrapolation of energy requirements. The most direct of these is the calculation of electrical energy per solution volume [67]. The total disruption energy has been calculated as the input energy required to reach a specified level of cell disruption for a given pretreatment method [64, 72]. This figure is then transformed to disruption energy per cell using measured microalgae cell concentrations [64, 72]. A "figure of merit" was presented in one study as the percent cell disrupted over the product of energy per volume and treated volume fraction [67].

One calculation step not often employed in direct microalgae pretreatment studies is the expression of output as an energy value. For the extraction of oils bound for a biorefinery, this would be a complicated accounting, and so is reasonably left to larger scale studies. However, where a single or few final products are to be created, an energy value can be easily generated as the chemical potential energy of the extracted products. This has been done as the energy of additional methane produced by anaerobic digestion as its higher heating value (HHV) [83].

One interpretation of efficiency used commonly in the reviewed literature is that of performance as either a fraction of the total (or maximum) performance or a ratio of production mass to source mass. In terms of cell disruption this appears as fraction of undisrupted cells remaining and fraction of total metabolite not released [78]. Lipid extraction efficiency is also shown as percent dry weight of lipid in the performed extraction divided by the percent dry weight of total lipid in the algae as determined by alternate analysis [45, 73]. In the biochemical conversions, this

interpretation of efficiency has been presented as: enhancement of production of methane by anaerobic digestion (% over control) [83], steady state methane yield divided by maximum theoretical methane yield (m^3 CH_4/kg COD) [70], biochemical methane potential (BMP) (ml CH_4 / g VS algae)[84], biodegradability efficiency as measured versus theoretical BMP [84], ethanol yield (g ethanol/g algae dry weight) [75], ethanol production efficiency (unspecified basis) [85], and percent biodegradability (unspecified basis) [68]. The interpretation of efficiency in the literature begins to shift toward energy with the calculation of performance as lipid yield per ultrasonic dosage (kWh/m^3) [65].

As mentioned above, very few papers in the reviewed literature present their results in units of energy at the scale of a single treatment process. A correspondingly small number of studies are then able to present results in terms of even a limited energy balance to translate to energy efficiency of the process. Net energy of a pretreatment process as the difference between energy of additional methane produced by anaerobic digestion as higher heating value (HHV) and pretreatment energy input was determined in [83]. This is converted to a form of energy efficiency for the process as the ratio of the HHV of additional methane produced by anaerobic digestion to pretreatment energy input.

1.2.3 Optimization

Much of the reviewed literature does not include any explicit optimization. Optimization is foregone in favor of exploration of the parameter space for select pretreatments and/or comparison of performance between select pretreatments. These

are done as planned experiments with explicitly stated variables and outcomes to be measured, but without explicitly stated objective functions or statistically designed experiments. The few exceptions that performed designed experiments and/or optimizations employed response surface methodology (RSM) [58], central composite design (CCD) [75], and orthogonal analysis technique [85]. Interesting exceptions include the estimation of optimal pretreatment conditions based on kinetics of acid hydrolysis as an irreversible first order model with Arrhenius type temperature dependence [76] and the stated intention of minimizing free radical formation during ultrasonication [65], though no quantitative optimization was performed in either case. Studies that evaluated only two levels of a given variable were not considered optimizations, as they would only generate major effects plots.

For both enzyme and acid pretreatments, time [75, 76, 85], temperature [75, 76, 85], and concentration [75, 76, 84, 85] were common parameters explored. The most common variable was treatment time, occurring for pretreatments by blender homogenizer [67], water bath [67, 73], sonication [57, 59, 63, 64, 67], and microwave [58, 67, 72]. Two other variables that are operationally varied by treatment time are number of passes in a high pressure homogenizer [63, 64, 78] and treatment intensity in pulsed electric field [82, 83]. Additional variables that have been explored include: water bath temperature [74], drying temperature [57, 61], cell number concentration [64], microalgae mass concentration [75, 83], ratio of biomass to accompanying solvent during pretreatment [58, 82], high pressure homogenizer pressure [78],

ultrasound amplitude [65], ultrasonic power [68], catalyst concentration [58], ionic strength (IS) [83], and pH [83].

With so many variables to monitor, attempts have been made to simplify comparisons through the introduction of lumped and/or calculated parameters such as: sonication power density (W/ml) [59], ultrasonic dosage (kWh/m^3) [59, 65], specific supplied energy ($Es = (P*t)/(V*TS_0)$) [68], combined severity factor (CSF) [76], and treatment intensity (TI) [82, 83].

1.2.4 Physical and Chemical Characteristics

Characterization of microalgae strains is performed to determine their suitability for use in biofuel production. Information about the composition and physical and chemical behavior of microalgae species is used to screen newly isolated strains and select strains for comparison in further processing. The most important compositional determination related to biofuels is the ratio between the three classes of biological macromolecules: lipids, carbohydrates, and proteins.

The lipid fraction of microalgae biomass is important in biofuels for the production of oil and liquid fuel products. The chemical profile of the lipid fraction, as mentioned above is still relevant, but is not used as an initial screening tool. Determinations of the total lipid include gravimetric measurements of ash free dry weight [41, 58, 62], lipid yield as percent of ash free dry weight [41], and lipid yield as percent of dry weight [42, 46, 47, 57, 58, 69]. Gravimetric determinations are labor intensive, and faster indicator tests have been demonstrated, such as lipid content via *in vivo* fluorescence of Nile Red stain [42] and lipid content via fluorescence of Nile

Red stained extracted lipid phase [46]. The staining of the extracted fraction does not save much labor, as the extraction must still be carried out. Another important determination to make is the lipid distribution in cells. Lipids stored in different structures of the cell will have different availability and susceptibility to pretreatment and extraction. This distribution has been determined by inspection of transmission electron micrograph (TEM) images [58].

The carbohydrate fraction of microalgae biomass is most important in biofuels for the production of ethanol and methane by fermentation and anaerobic digestion, respectively. Total cell carbohydrate has been determined by anthrone reagent colorimetry [76, 85], with starch content measured by iodo-starch reaction [76, 85] and monomeric sugars measured by HPAEC [85]. Dextrin (a short chain sugar) and glucose (a monomer) have also been measured by HPLC [85]. The distinction between monomers and starches is important to make. While many simple sugars are easily digested in fermentation and anaerobic digestion, the complex starch fraction may include refractive materials that do not readily biodegrade, negatively affecting yields.

The protein fraction of microalgae biomass is only important in biofuels in negative ways. A high protein fraction takes away from the fractions in lipids and carbohydrates. Protein is not directly extractible as a fuel product and it biodegrades more slowly than sugars. Protein also has higher nitrogen content than lipids and carbohydrates, contributing to ammonia formation under reducing conditions. Measurements related to protein in microalgae include TKN as a fraction of COD

[68], ammonium fraction of TKN [68], and total intracellular protein via Bradford reagent colorimetry [76, 85].

COD of microalgae is an important determination for energy calculations relating to biofuels. Because COD is an approximation of the maximum capacity for oxidation of a material, it is used as an experimental benchmark for oxidation processes. The biofuels generated from microalgae will eventually be combusted, completing their oxidation to carbon dioxide, so the starting point at the level of the cell is relevant. The change of its soluble fraction has been measured as an indicator of performance of pretreatment [83] and the ratio of COD of substrate to VS of inoculums is employed in anaerobic digestion [68].

Solids measurements are carried out on microalgae cultures used for biofuel. They serve to indicate mass concentrations for mixing of solutions (TS and TSS) [82, 83], but in combination with other measurements such as VS [83] and COD [68] can provide indications of biomass composition and density of oxidation potential.

In addition to the chemical characteristics mentioned above, physical characteristics must be considered. The shape and size of cells along with the structure and material behavior of their cell walls will have a strong influence on how they react to pretreatments intended to rupture the cell wall.

Particle size of microalgae has been measured by Coulter counter [41], dynamic light scattering [63], laser diffraction [68], and visual inspection under a

microscope [46]. Cell shape of microalgae has been extensively determined, and is easily observed by microscopy.

The detailed physical characteristics of the cell wall are not easily determined using light microscopy. The large scale qualitative integrity of the cell wall, however, can be seen [41, 65]. A more detailed picture requires electron microscopy, where both SEM and TEM are useful. In terms of composition, SEM provides a qualitative elemental analysis of the cell surface when combined with energy-dispersive X-ray spectroscopy (EDS) [58]. TEM provides a cross section view that identifies structural patterns and quantifies cell wall thickness [58] and pore size [72]. Microalgae cell wall structure and composition have been determined, as summarized in [72]. Material properties of the microalgae cell wall have been characterized by rupture experiments via nitrogen decompression [87], direct physical compression, and atomic force microscopy [88].

1.2.5 Models of Physical and Chemical Effects

Models of pretreatment effects in the reviewed literature are mostly empirical or speculative in nature. Kinetic models have been applied to thermal degradation [46, 58] and cell disruption [64, 89]. A less formal curve fitting procedure is more the norm, as applied for solvent effects on extraction via linear solvation energy relationship (LSER) [47], disruption decay parameters [78], and cell disruption fraction as a function of number of HPH passes [78]. The more speculative proposed model is exemplified by the assertion that microwave duty cycle (heating cycle) has a fatigue effect on cell walls, decreasing failure energy [67].

Theoretical models of cell fracture are more extensively documented for higher plants than for microalgae, related specifically to food processing and structural lumber products [90-92]. Microalgae cell fracture has been modeled in a limited fashion in [38, 64], and these are only developed to the extent required to make a rudimentary energy calculation. The two approaches presented are those of cell wall tensile strength and hydrogen bond strength. Both of these approaches rely on extensive assumptions that, while good for initial approximations, prevent the prudent use of their results for any further application.

1.2.6 Mechanisms

The mechanisms of pretreatment are not discussed in depth, or at all, in most direct pretreatment studies. The mechanism of extraction is occasionally addressed, as in the case of a lipid mass transfer kinetic diffusion model and mass transfer coefficient from microalgae cells to super-critical CO_2 (SCCO2) [81]. There are qualitative descriptions of the macroscopic structural mechanisms observed [67], but only two nanoscale models were found: a structural biochemical mechanism of cell wall disintegration due to microwave [72]; and a mathematical model for the radial dynamics of cavitation bubbles with which the magnitudes of the microturbulence velocity and pressure amplitude of the shock waves was estimated [69].

The diversity of studies seen in microalgae pretreatment for biofuels is an encouraging indication of the resources being applied to this problem. However, this diversity is also the result of a lack of a systematic and cohesive approach in the field.

The data are not sufficiently consistent to allow the reliable prediction of performance through the process train or between studies.

1.3 Outline and Contributions

This research focuses on the responses of microalgae to pretreatment by power ultrasound, and the potential created by those responses, in order to better understand the energy relationships involved. Chapter 1 has presented the broader context and motivation for the work followed by a brief review of the literature on pretreatment of microalgae biomass. Chapter 2 addresses the issue of energy requirements through the development of a constitutive model of cell rupture energy. The energy transferred to solution in power ultrasound systems is then explored as a measure of energy input to solution. The constitutive model predicted energy requirements are then compared to experimental pretreatment performance using a selected power ultrasound pretreatment system.

The sensitivity of the constitutive model is evaluated in Chapter 3. The high sensitivity variable of cell diameter is then measured to decrease uncertainty in the Monte Carlo Simulations of cell rupture energy that follow. Chapter 4 addresses the selection of microalgae growth media for cultivation and the growth program during cultivation. The effect of growth medium on apparent cell strength as resistance to ultrasound pretreatment is then evaluated, and the implications for energy extractability are explored.

The kinetics and mechanism of cell disruption are developed in Chapter 5 under two theoretical frameworks that couple the cell constitutive model with cavitation dynamics in cell-cavitation interactions. Chapter 6 summarizes the conclusions of the study.

The contributions of this work to scientific knowledge supporting microalgae based biofuel development are summarized below:

- Expansion of the functionality of cell rupture prediction models through the development of a constitutive model of cell rupture energy;
- Improved characterization of potential error in the extrapolation of single cell rupture energy via identification of high sensitivity variables for cell rupture pretreatment of unicellular biomass;
- Extension of the concept of cell rupture energy from single value determinations to distributions with multiple dimension of statistical uncertainty;
- Presentation of a method to evaluate the envelope of cell rupture energies for a given species with known physical characteristics;
- Introduction of the concept that growth conditions have a potential impact on susceptibility to pretreatment and experimental evaluation of those effects;

- Expansion of the understanding of cavitation dynamics by linking a kinetic model of reaction, reactor model, constitutive cell rupture model, and proximity parameterized energy threshold.

Chapter 2 - Energy Requirements and Ultrasound Processing

2.1 Constitutive Model of Cell Rupture

2.1.1 Introduction

The efficient processing of unicellular biomass for extraction of products is a central requirement of the growing bio-economy. An often employed strategy to improve extraction performance is the rupture of cells to encourage the release of intracellular materials. In order to evaluate the theoretical limits of the efficiency of cell rupture, a theoretical framework of the physical mechanism of cell rupture is required. This work develops part of that framework.

Detailed models have been produced to infer the molecular level mechanics of membranes and cell walls. The physics of membranes of various geometries under stress is summarized well by [93] and tied to measurements of membrane elasticity and buckling behavior. However, it is also noted that dynamic stresses existing in complex environments, such as those encountered in most biomass pretreatment systems, tends to confound these models as they currently exist. A more applied vision is explored in models of the composition, composite structure, and mechanics of cell walls in higher plants [91, 94]. These analyses are directly aimed at strength and processing requirements of food, lumber, and other products, which makes them

slightly more suitable to the dynamic processing of microalgae. However, the mechanical efficiency of cell walls in organism level tissue structures exists in a completely different boundary scheme than that of a single cell in suspension. Thus the characterization of cell wall decomposition and fracture for populations of single cells in suspension requires a different approach.

Two 'back-of-the-envelope' approaches to calculating specific cell rupture energy were provided in [38] based on the tensile strength of a cell wall modeled as a thin shell and based on hydrogen bond energy of a cell wall modeled as 100% composed of hydrogen bond pairing atoms. This type of approach accomplishes its aim of being both quick and easy to understand, but the simplifying assumptions generate somewhat misleading results. Variations in cell properties require validation, and direct extrapolation to industrial scale poses risk of large error.

Specialized material testing procedures are required to measure the properties of single cells to validate model parameters, and experimental studies measuring cell rupture energy have employed both direct and indirect approaches. Bridging between tissue and individual cell tests, micro-penetration has been applied to individual cells in cubes of potato parenchyma [95]. For cell suspensions, gas decompression has been applied to *Chlamydamonas eugametos* [87] to correlate cell rupture with pressure change to reveal the rupture pressure of the cells. Atomic force microscopy [88] has been employed to measure cell surface deflection in response to applied force in *Tetraselmis suecica*, but the requirement of a semi-rigid surface limits this test's applicability.

The current work modifies and extends the basic constitutive model of [38]. The objective of the model extension is to determine the range of energy required for microalgae cell rupture. This is done by exploring the stress-strain behavior of a cell wall material in assumed cell geometries. The minimum energy required for rupture is important as a benchmark for energy efficiency calculations, and a range will provide more useful estimates of industrial performance than single value extrapolation.

2.1.2 Conceptual Framework

The aspects of cell rupture that require definition and development for energy analysis are: cell geometry, material, applied force, failure threshold, and failure mechanism.

Cell geometry defines the general shape of the cell and the thickness of its wall material (T_{cw}). The two most appropriate approximations to cell shape in microalgae are a sphere and a cylinder. Both of these will have an associated diameter (d_c) defining a circumference ($Circ_{cell}$), but the cylinder will also have length (l).

Material can be thought of on two scales. At the scale of a suspension of many cells, the concentration of cells on a dry mass (C_c) or number (N_c) basis per volume of solution is a defining characteristic. This will be used in the extrapolation to overall energy, but is not required for the initial modeling of a single cell. The second scale is that of the single cell and the material of its cell wall. The density of material can be seen as the bulk cell material density (wet basis ρ_c, or dry basis $\rho_{c,d}$) or more focused as the density of only the cell wall material (ρ_{cw}). A further complication arises when the composition of the cell wall material is defined in terms of mass fraction of its

constituent chemical components and the microstructure they form. The cell wall material can be considered as a composite, defined by non-uniform material distribution and, perhaps, grain size. The truth of the cell wall structure is more complex, with constituent components forming something like a woven laminate composite at the molecular level [91]. At this level of structural definition layer composition and orientation, internal molecular structure and cross-linking, and binding agents holding the lamina together could be considered. While the composition and structure of the material are important, the factors that we are more concerned with, from an energy perspective, are its physical and mechanical properties. A simplifying assumption of homogeneity is applied to eliminate these complications. The wall is also assumed to be smooth, isotropic, and of uniform thickness for modeling purposes.

The applied force can be considered as either internally or externally applied. For an internally applied force, the modes of action are by internal volume expansion or contraction causing tension or compression in the constraining wall. Any compression in this scenario would likely be extremely transient with the end result being folding rather than rupture due to buckling. Thus, internal force leads to failure due to tension. Even though these are called internally applied forces, they are still caused by changes in externally applied stimuli. Externally applied forces, however, can act directly through tension, shear, or compression. Localized tension will be expressed in the wall as tension and/or shear, depending on the relative spatial scale of the force application area and the cell size. Because a fluid matrix is partially defined

by its continuous deformation under shear, the ability to apply a shear force to a cell in suspension is questionable. Any attempt to apply a shear force to the cell would simply result in displacement within the fluid. Shear forces within flowing fluid would be experienced as pressure differentials around the cell, leading to tension within the wall material. Shock waves or solid surface impingement on the cell would be a compression on the scale of the whole cell, but due to the contiguous pressure vessel nature of the cell would be expressed as tension force in the wall material. From this discussion it can be seen that one only need model failure in tension.

When determining the total amount of energy expended to cause a material to fail, the mechanism by which the failure occurs is important. This failure mechanism and energy are related through the stress-strain behavior of the material. The material is first assumed here to exhibit linear elastic (brittle) behavior. The failure threshold resulting in cell rupture is assumed to be achieved when the cell wall material reaches its failure strain (ε_f). Without knowing the failure mechanism it is difficult to directly model the expected energy of failure. However, because of the short time scale of cavitation bubble interactions with cells, a sudden catastrophic failure is assumed.

2.1.3 Model Derivation

The constitutive model is derived here as a variation of that presented in [38]. The analytical forms and resulting energy values are compared. The conceptual framework of the previous section and additional specifications referenced in the derivation that follows are summarized graphically in Figure 2.1.

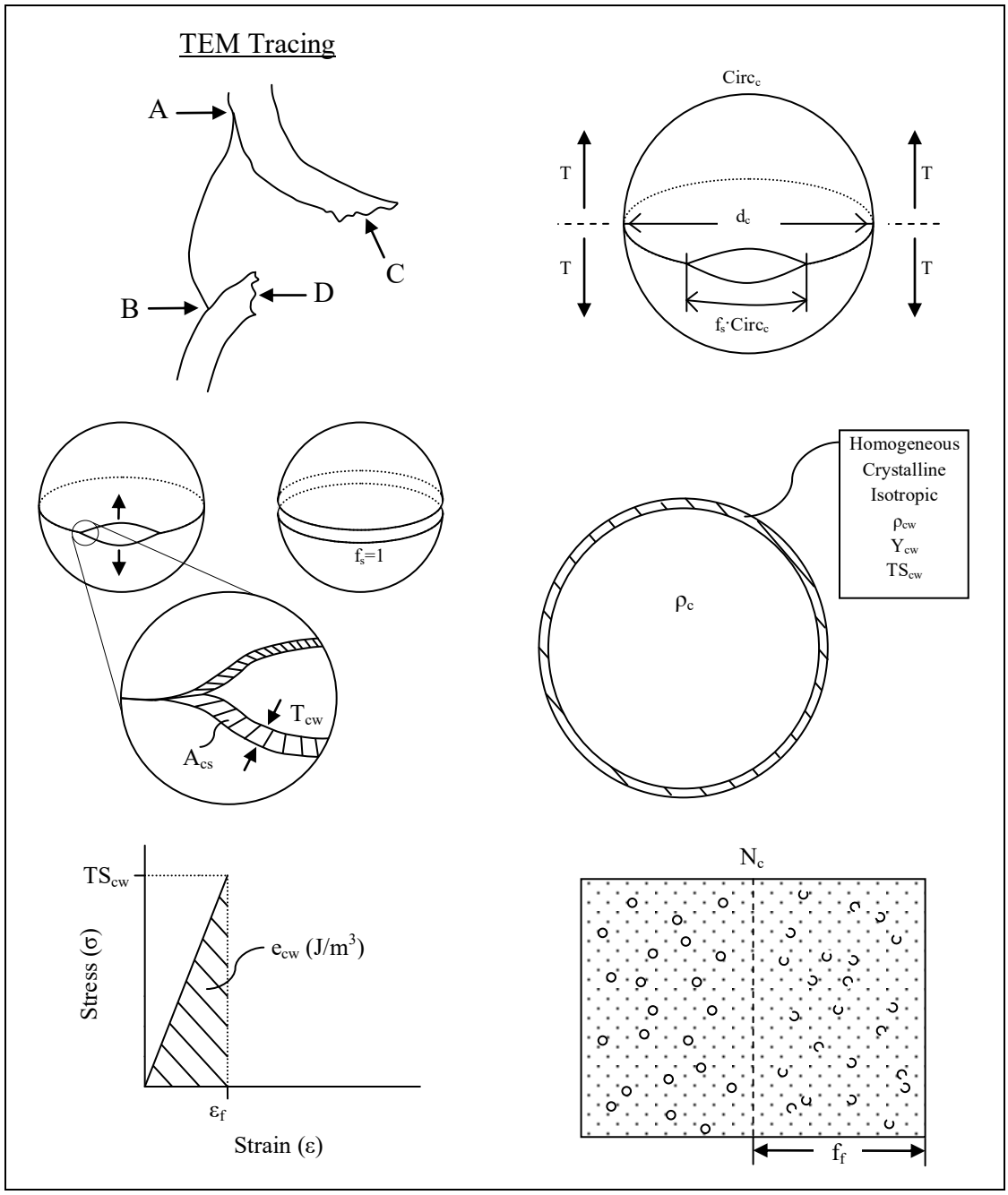

Figure 2.1 – Cell wall separation geometry and constitutive cell rupture model foundations

The objective of this model is to calculate the energy required per unit of volume of solution to achieve rupture of a fraction of cells. Total energy (E_T) = energy per volume solution (e) x volume of solution (V).

$$E_T = e * V$$

Energy per volume solution = energy per cell (e_c) x number of cells per volume of solution (N_c) x fraction ruptured (f_f).

$$e = e_c * N_c * f_f$$

Number of cells per volume of solution = dry mass concentration of cells per volume of solution (C_c) / dry mass per cell ($m_{c,d}$). Additional variables defined for a cell are: volume (V_c), diameter (d_c), dry weight density ($\rho_{c,d}$), water mass fraction (f_w).

$$V_c = \frac{4}{3}\pi\left(\frac{d_c}{2}\right)^3$$

$$N_c = \frac{C_c}{m_{c,d}}$$

$$= \frac{C_c}{\left(\rho_{c,d} * V_c * (1 - f_w)\right)}$$

$$= \frac{C_c}{\left(\rho_{c,d} * \left(\frac{4}{3}\pi\left(\frac{d_c}{2}\right)^3\right) * (1 - f_w)\right)}$$

$$= \frac{6C_c}{\pi {d_c}^3 \rho_{c,d} * (1 - f_w)}$$

Energy per cell = Energy per volume of disrupted material (e_{dm}) x volume of disrupted material (V_{dm}).

$$e_c = e_{dm} * V_{dm}$$

Volume of disrupted material = fraction of circumference separation (f_s) x wall cross section area (A_{cs}) x failure strain (ε_f) x ½ circumference of cell ($Circ_c$) (assuming cylindrical separation at equator).

$$V_{dm} = \frac{1}{2} f_s * A_{cs} * \varepsilon_f * Circ_c$$

Energy per volume of disrupted material = Area under the stress (σ) – strain (ε) curve for cell wall material.

$$e_{dm} = \int \sigma \, d\varepsilon$$

Assuming a linear elastic region for a brittle material with Young's modulus (Y_{cw}) and tensile strength (TS_{cw}) gives:

$$\sigma = Y_{cw} \varepsilon$$

$$e_{dm} = \int_0^{\varepsilon_f} Y_{cw} \varepsilon \, d\varepsilon = \frac{1}{2} TS_{cw} * \varepsilon_f$$

Substituting into the equation for energy per volume of solution gives:

$$e = \frac{6C_c}{\pi {d_c}^3 \rho_{c,d} * (1 - f_w)} * \left(\frac{1}{2} f_s * A_{cs} * \varepsilon_f * Circ_c\right) * \left(\frac{1}{2} TS_{cw} * \varepsilon_f\right) * f_f$$

The circumference and cross sectional area are then determined:

$$Circ_c = \pi d_c$$

$$A_{cs} = \frac{\pi}{4} {d_c}^2 - \frac{\pi}{4}(d_c - 2T_{cw})^2$$

$$= \frac{\pi}{4}\left(4 d_c T_{cw} - 4 {T_{cw}}^2\right) \; ; \quad assume \; T_{cw} \ll d_c$$

$$= \pi d_c * T_{cw}$$

Substituting these terms gives:

$$e = \frac{6C_c}{\pi {d_c}^3 \rho_{c,d} * (1 - f_w)} * \left(\frac{1}{2} f_s * (\pi d_c * T_{cw}) * \varepsilon_f * (\pi d_c)\right) * \left(\frac{1}{2} TS_{cw} * \varepsilon_f\right) * f_f$$

This simplifies to Equations 2.1 below:

$$e = f_f f_s \left[\frac{3\pi * C_c * T_{cw} * TS_{cw} * {\varepsilon_f}^2}{2 * d_c * \rho_{c,d} * (1 - f_w)}\right] \quad e_c = f_s \left[\frac{\pi^2 * TS_{cw} * T_{cw} * d_c^2 * \varepsilon_f^2}{4}\right] \qquad (2.1)$$

Whereas the equations of [38] in equivalent variables simplify to Equations 2.2 below:

$$e = f_s^2 \left[\frac{6\pi * C_c * T_{cw} * TS_{cw} * \varepsilon_f}{d_c * \rho_{c,d} * (1 - f_w)}\right] \quad e_c = f_s^2 \left[\pi^2 * TS_{cw} * T_{cw} * d_c^2 * \varepsilon_f\right] \qquad (2.2)$$

The differences between these results are summarized as:

$$e_{2.1} = e_{2.2}\left(\frac{f_f \varepsilon_f}{4 f_s}\right) \qquad e_{c,2.1} = e_{c,2.2}\left(\frac{\varepsilon_f}{4 f_s}\right)$$

Under the present derivation, the energy requirement shifts from dependence on the square of the split fraction to the square of the failure strain of the cell wall material.

This is interesting because our assumed stress-strain behavior limits the value of the strain to a very low value. The standard assumed value for the elastic-plastic transition for a stiff material is ε = 0.002 [96]. A very rough numerical value can be calculated from the numbers used in [38] and [87], and the value of ε assumed here.

$$f_f = 0.5;\ f_s = 0.25;\ C_c = 5\frac{kg}{m^3};\ T_{cw} = 100 * 10^{-9}m;\ TS_{cw} = 638 * 10^6\frac{N}{m^2};$$

$$\varepsilon_f = 0.002;\ d_c = 15 * 10^{-6}m;\ \rho_{c,d} = 1000\frac{kg}{m^3};\ f_w = 0.9$$

$$e = 5.01 * 10^{-1}\frac{J}{m^3};$$

It should be noted that the value used in [38] for ε was 0.3. A measurement from the published image gives an unrounded value of 0.25 for ε. If this number is used here, then the value for e becomes e=7.83*10^3 J/m^3, which reflects the 4 order of magnitude increase we expect based on the quadratic dependence of energy on strain. It should also be noted that this value is approximately 6x the value of 1.31*10^3 J/m^3 produced in [38]. One of the reasons for this discrepancy is a failure in [38] to normalize the hemispherical force to the wall cross sectional area when determining tensile strength from [87].

These energy values may be somewhat unreliable because of their quadratic dependence on strain, and the difficulty of actually measuring strain at the scale of a cell wall. To determine whether this issue can be avoided, the next section explores variations of the model derivation.

2.1.4 Derivation Outline

The objective of this section is to first visually outline the derivation presented in the previous section, and then use this outline to identify functions that can take alternative mathematical forms based on different assumptions, called generic functions here. The energy equation is then generalized in terms of these generic functions with the intention that combinations of these functions will yield the extrema of ranges of total energy.

Figure 2.3 presents a visual outline of the model derivation. Generic functions are boxed.

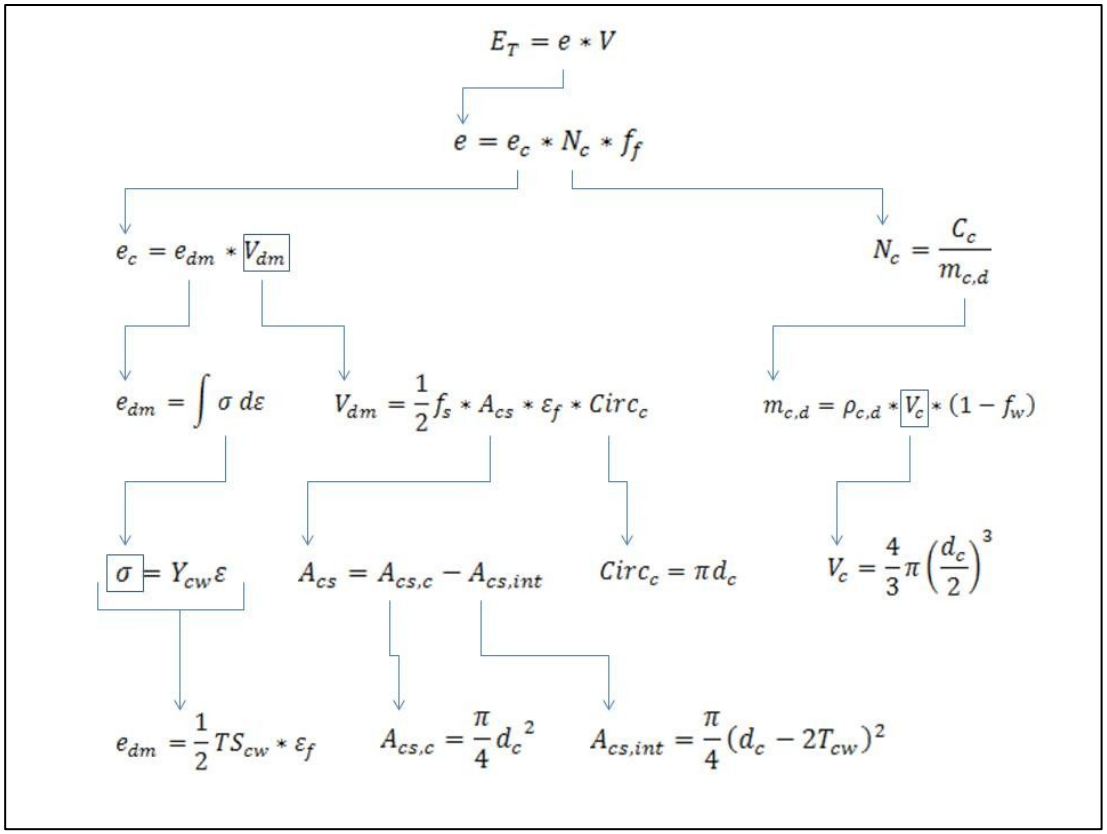

Figure 2.2 – Rupture energy model derivation outline

Generalizing the energy equation in terms of these generic functions gives:

$$e = \left[\int_0^{\varepsilon_f} \boldsymbol{\sigma} \, d\varepsilon\right] * \boldsymbol{V_{dm}} * \frac{C_c}{\rho_{c,d} * \boldsymbol{V_c} * (1 - f_w)} * f_f$$

Generic Functions

$\sigma(\varepsilon)$: stress-strain curve behavior

V_{dm} : volume of disrupted material

V_c : volume of the cell

2.1.5 Generic Functions

The stress-strain behavior generic function can describe 5 basic categories of material reaction under an applied load: brittle, slightly ductile brittle, ductile, plastic, and highly elastic. Characteristic stress-strain curve shapes for each of these categories, along with necking behaviors, are presented in Figure 2.4 (adapted from Callister, 2007, p. 525, 147, 209) [96].

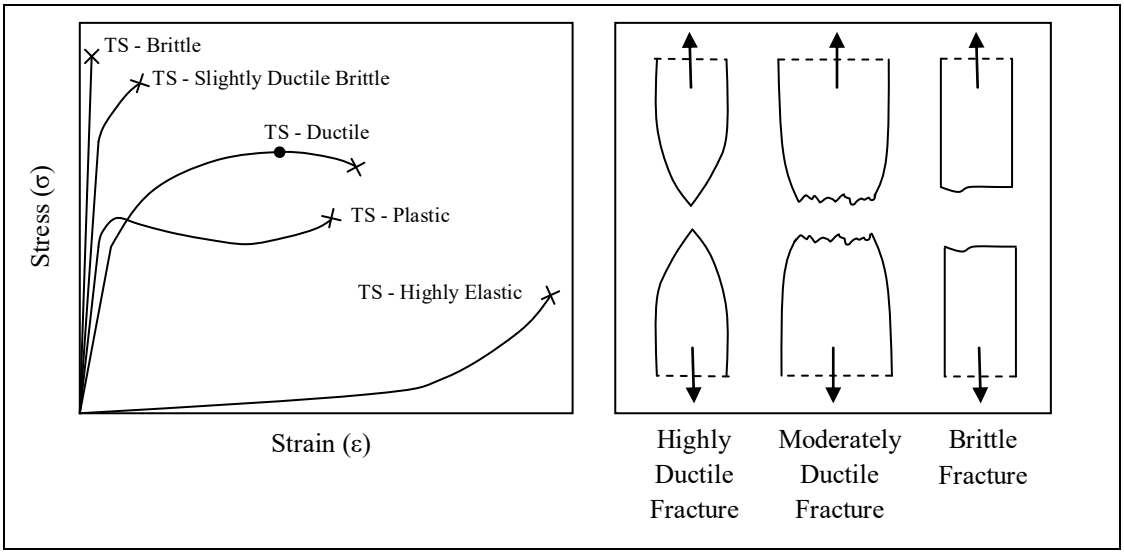

Figure 2.3 – Characteristic stress-strain curves and necking behavior

These curves can be represented by piecewise functions to reflect the difference in behavior between the elastic and plastic deformation regions. The functions presented in this section are only starting points for derivation. Parameterization is presented in the next section.

A brittle material will have a linearly elastic behavior up until rupture. It is represented by a linear stress-strain curve with a slope equal to the Young's modulus (Y) for the material.

Brittle: $$\sigma(\varepsilon) = Y\varepsilon$$

The slightly ductile brittle material in plastic deformation exhibits a high initial slope until the yield strain (ε_y) followed by a continuous decrease in that slope, visually approaching, but never reaching, zero. This can be represented as a square root function.

Slightly Ductile Brittle: $$\sigma(\varepsilon) \approx \begin{Bmatrix} Y\varepsilon & | 0 \leq \varepsilon \leq \varepsilon_y \\ \sqrt{\varepsilon} & | \varepsilon_y < \varepsilon \leq \varepsilon_f \end{Bmatrix}$$

Ductile material behavior in plastic deformation exhibits a characteristic positive decreasing slope that continues to decrease beyond an apex point. This is also characteristic of a parabola, so this curve will be described with a quadratic function.

Ductile: $$\sigma(\varepsilon) \approx \begin{Bmatrix} Y\varepsilon & | 0 \leq \varepsilon \leq \varepsilon_y \\ \varepsilon^2 & | \varepsilon_y < \varepsilon \leq \varepsilon_f \end{Bmatrix}$$

The characteristic shape of a stress-strain curve for a plastic material is a linearly elastic region, followed by an oscillatory function in plastic deformation. The oscillation displays an increasing period with increasing strain and an upward overall slope. An initial approximation of this oscillation can be given by a modified sine wave with an upward sloping center line. However, it should also be considered that our final purpose in this model is to produce the integral of the function. Because this is the case, the integral may be more easily determined from a linear approximation that would yield approximately the same integral value.

$$\sigma(\varepsilon) \approx \begin{cases} Y\varepsilon & \left| 0 \le \varepsilon \le \varepsilon_y \right. \\ \sin(\varepsilon) + Y_2\varepsilon & \left| \varepsilon_y < \varepsilon \le \varepsilon_f \right. \end{cases}$$

Plastic:

-- or --

$$\sigma(\varepsilon) \approx \begin{cases} Y\varepsilon & \left| 0 \le \varepsilon \le \varepsilon_y \right. \\ Y_2\varepsilon & \left| \varepsilon_y < \varepsilon \le \varepsilon_f \right. \end{cases}$$

Highly elastic behavior is characterized by continued large strain with very little stress, up to a point. Beyond this point the slope of the curve begins to drastically increase until failure of the material. This shape can be represented as an exponential function shifted down to meet the origin on the graph.

Highly Elastic: $\sigma(\varepsilon) \approx e^{\varepsilon} - 1$

The functions for the volume of disrupted material (V_{dm}) generic function can assume either a constant or changing volume over the course of deformation. Within each of these, the treatment will vary based on the cell geometry. However, an evaluation of a changing volume would require direct measurement, so, for now, constant volume is assumed.

In a spherical or cylindrical cell, it is assumed that the equatorial circumference expands into a cylindrical section with a height determined one of three ways. First, the height (h) can be assumed as a surface region within a fixed distance from the circumference of the undisturbed cell.

$$V_{dm} = f_s * A_{cs} * 2h$$

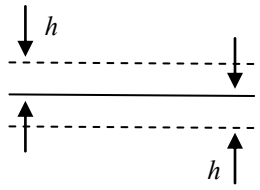

This distance can take an assumed value, or it can be taken as a fraction (α) of the material length in the direction of elongation. In the case of a sphere and cylinder we have, respectively:

$$V_{dm} = f_s * A_{cs} * \alpha * \frac{1}{2} Circ_c \qquad V_{dm} = f_s * A_{cs} * \alpha * l$$

If, however, we calculate the height of disrupted material as being proportional to the actual strain (at failure or some other point) we have, for a sphere and cylinder, respectively:

$$V_{dm} = f_s * A_{cs} * \varepsilon * \frac{1}{2} Circ_c \qquad V_{dm} = f_s * A_{cs} * \varepsilon * l$$

The volume of the cell (V_c) generic function will assume a simple geometry described by average literature values for a given species. The equations for the volumes of a sphere and cylinder are, respectively:

$$V_c = \frac{4}{3}\pi\left(\frac{d_c}{2}\right)^3 \qquad V_c = \pi\left(\frac{d_c}{2}\right)^2 * l$$

Now that the forms have been stated, the permutations of these generic functions to form energy equations of different material behavior, geometry, and

assumptions are presented. The energy equation is restated below with subscripts to identify combinations of the generic functions (Equations 2.3). All combinations will result in 30 equations.

$$e_{i,j,k} = \left[\int_0^{\varepsilon_f} \boldsymbol{\sigma_i}\, d\varepsilon\right] * \boldsymbol{V_{dm_{j,k}}} * \frac{C_c}{\rho_{c,d} * \boldsymbol{V_{c_k}} * (1 - f_w)} * f_f \tag{2.3}$$

Table 2.1 – Index notation key for Equations 2.3

σ(ε)	V_{dm}	V_c
(i=1) – Brittle (i=2) – Slightly Ductile Brittle (i=3) – Ductile (i=4) – Plastic (i=5) – Highly Elastic	(j=1) – Assumed Height (j=2) – Surface Fraction (j=3) – Strain Based	(k=1) – Sphere (k=2) – Cylinder

The expressions for cell volume and volume of disrupted material can be combined into six pairings in $H_{(j,k)}$ in the non-integral portions of the energy equation.

$$H_{(j,k)} = V_{dm_{j,k}} \frac{C_c}{\rho_{c,d} * V_{c_k} * (1 - f_w)} * f_f$$

Substituting and simplifying in this expression gives:

$$H_{(1,1)} = 12 f_f f_s \frac{h T_{cw} C_c}{\rho_{c,d} {d_c}^2 (1 - f_w)} \qquad H_{(1,2)} = 8 f_f f_s \frac{h T_{cw} C_c}{l \rho_{c,d} d_c (1 - f_w)}$$

$$H_{(2,1)} = 3\pi f_f f_s \frac{\alpha T_{cw} C_c}{\rho_{c,d} d_c (1 - f_w)} \qquad H_{(2,2)} = 4 f_f f_s \frac{\alpha T_{cw} C_c}{\rho_{c,d} d_c (1 - f_w)}$$

$$H_{(3,1)} = 3\pi f_f f_s \frac{\varepsilon_f T_{cw} C_c}{\rho_{c,d} d_c (1 - f_w)} \qquad H_{(3,2)} = 4 f_f f_s \frac{\varepsilon_f T_{cw} C_c}{\rho_{c,d} d_c (1 - f_w)}$$

These $H_{(j,k)}$ terms can be factored to separate the common terms as $M = \frac{f_f f_s T_{cw} C_c}{\rho_{c,d} d_c (1 - f_w)}$.

$$H_{(1,1)} = 12 \frac{h}{d_c} * M \qquad H_{(1,2)} = 8 \frac{h}{l} * M$$

$$H_{(2,1)} = 3\pi\alpha * M \qquad H_{(2,2)} = 4\alpha * M$$

$$H_{(3,1)} = 3\pi\varepsilon_f * M \qquad H_{(3,2)} = 4\varepsilon_f * M$$

2.1.6 Parameterization

Before the energy equations can be evaluated, the stress strain curves must be parameterized to the available data. In order to reasonably compare the curve integrals (energy values), it is first required that the shared parameters between the curves be reconciled. If results are to be compared, they must be calculated using the same parameter values. This choice implies overlap in the elastic region and at critical yield and failure points.

This creates a problem for several parameters because of their fundamental difference under different stress-strain regimes. Young's modulus, yield stress, yield strain, tensile strength, and failure strain must all be reconciled.

Tensile stress is the maximum point on the stress-strain curve, occurring at either an end point (failure) or an internal point. In Brittle, Slightly Ductile Brittle, and Highly Elastic behavior, the maximum stress coincides with the end point of the curve at failure. In Ductile behavior, the tensile stress is defined as the apex of the curve, occurring before failure. In Plastic behavior, however, we may have a maximum stress at either an internal apex or the end point. An initial slope transition leads to the internal apex, and strain hardening later leads to an increase in stress before failure, which may or may not lie at a higher stress value than the internal apex.[97]

In the type of blind loading performed on single cells in solution to determine material properties (i.e. decompression test), the only measured data are the post relaxation strain and the maximum applied stress. Therefore, these must be our limiting parameters that must coincide for all models. Recall from above that it may be appropriate to simplify analysis of the Plastic curve by approximating its non-linear region as linear. This is shown as a dashed line in Figure 2.5.

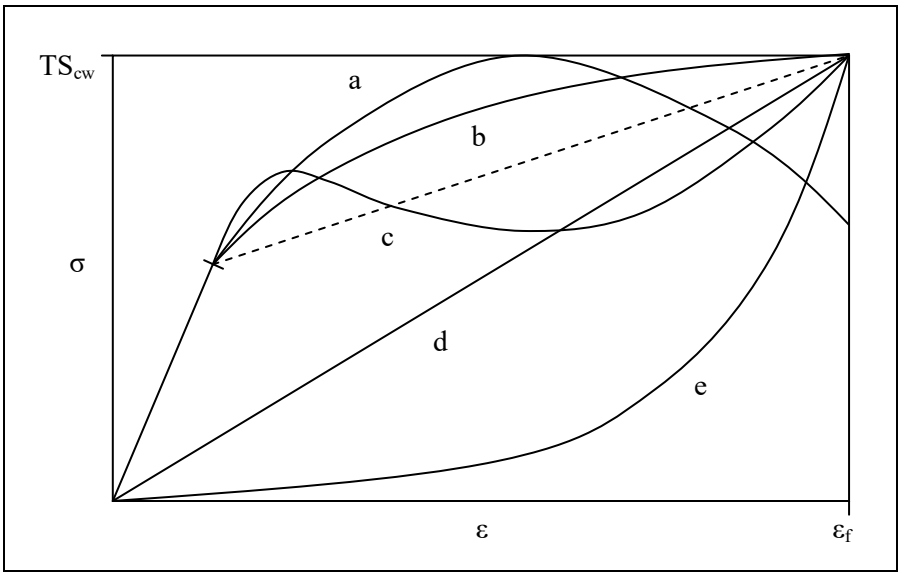

Figure 2.4 – Parameterized stress-strain curves: a) ductile, b) slightly ductile brittle, c) plastic, d) brittle, e) highly elastic

The next difficulty is the observation of post relaxation strain, not actual failure strain. With no method for direct determination of the Young's modulus in a separate test, we cannot correct our post relaxation strains to actual strain at failure. In this model, such a correction will be assumed to be negligible.

From the simple fact that we have a measurable elongation of a cell wall/membrane after failure [38], we can infer that the material does not behave as a purely linearly elastic Brittle material. Then, when the observed post relaxation failure strain lies to the right of some lower limit, any estimate of the Young's modulus that assumes this Brittle linear elasticity will be an underestimate. This limit can be shown, for purposes of thoroughness in the model, to be $\varepsilon_m = \left(\frac{TS*\varepsilon_y}{\sigma_y}\right)$ or $\varepsilon_f = \left(\frac{2TS}{\sigma_y}\right)\varepsilon_y$. Assuming this limit is met, we can use this underestimate as a lower bound for the range of the Young's modulus. However, with the possibility of Highly Elastic

behavior, the estimate of energy that would be calculated from the Brittle behavior cannot be used as a lower bound to the energy per volume value.

The Brittle behavior can be easily parameterized as the standard line $\sigma(\varepsilon) = m\varepsilon + b$. Figure 2.5 shows two model Young's moduli. The brittle model slope is distinguished as Y_B. The line passes through the two points (0,0) and (ε_f, TS). This results in the model equation below.

Brittle: $$\sigma(\varepsilon) = \frac{TS}{\varepsilon_y}\varepsilon$$

The non-linear segments of the Slightly Ductile Brittle, Ductile, and Plastic curves will be constrained by shared boundary conditions.

BC#1:	BC#2:	BC#3:
$\sigma(\varepsilon_y) = \sigma_y$	$\left.\frac{d\sigma}{d\varepsilon}\right\|_{\varepsilon=\varepsilon_y} = Y$	$\max(\sigma) = TS$

As stated above, the slightly ductile brittle non-linear segment will be modeled as a square root. The three boundary conditions require three parameters. The basic function is: $\sigma(\varepsilon) = \varepsilon^{1/2}$. Adding a coordinate shift gives: $\sigma(\varepsilon) = (\varepsilon - h)^{1/2} + k$. The incorporation of a scaling factor then gives the final parameter: $\sigma(\varepsilon) = a(\varepsilon - h)^{1/2} + k$.

By applying the shared boundary conditions (BC#1 – BC#3), the base function and parameter values are:

$$\sigma(\varepsilon) = a(\varepsilon - h)^{1/2} + k \qquad h = \frac{\left(TS - \sigma_y\right)^2}{4Y\left(TS - \sigma_y + Y\varepsilon_y - Y\varepsilon_f\right)} + \varepsilon_y$$

$$a = \frac{Y^{1/2}\left(TS - \sigma_y\right)}{\left(\sigma_y - TS + Y\varepsilon_f - Y\varepsilon_y\right)^{1/2}} \qquad k = \frac{\left(TS - \sigma_y\right)^2}{2\left(TS - \sigma_y + Y\varepsilon_y - Y\varepsilon_f\right)} + \sigma_y$$

The ductile non-linear segment will be modeled as a parabola. The three boundary conditions require three parameters. The basic function is: $\sigma(\varepsilon) = \varepsilon^2$. Adding a coordinate shift gives: $\sigma(\varepsilon) = (\varepsilon - h)^2 + k$. The incorporation of a scaling factor then gives the final parameter: $\sigma(\varepsilon) = -a(\varepsilon - h)^2 + k$. The three boundary conditions for this case are:

BC#1: $\sigma\left(\varepsilon_y\right) = \sigma_y$

BC#2: $\left.\frac{d\sigma}{d\varepsilon}\right|_{\varepsilon=\varepsilon_y} = Y$

BC#3a: $\left.\frac{d\sigma}{d\varepsilon}\right|_{\sigma=TS} = 0$

By applying the boundary conditions, the base function and parameter values are:

$$\sigma(\varepsilon) = -a(\varepsilon - h)^2 + k \qquad h = \varepsilon_y - \frac{2\left(\sigma_y - TS\right)}{Y}$$

$$a = \frac{-Y^2}{4\left(\sigma_y - TS\right)} \qquad k = TS$$

The plastic non-linear segment can be modeled as a modified sinusoid. To simplify the analysis, the sinusoid model is abandoned in favor of the linear approximation. For this case, the basic function is a straight line with BC#1 and

BC#3b ($\sigma(\varepsilon_f) = TS$), where a discontinuous slope at ε_y eliminates BC#2. This results in the base function and parameters below.

$$\sigma(\varepsilon) = m\varepsilon + b \qquad m = \frac{\sigma_y - TS}{\varepsilon_y - \varepsilon_f} \qquad b = \frac{TS\varepsilon_y - \sigma_y\varepsilon_f}{\varepsilon_y - \varepsilon_f}$$

The highly elastic curve is modeled as an exponential, as shown in the previous section. We have two boundary conditions for this curve, so we will have two parameters. The base function is: $\sigma(\varepsilon) = e^{\varepsilon}$. We can then add a vertical coordinate shift to give: $\sigma(\varepsilon) = e^{\varepsilon} + k$. The incorporation of a scaling factor in the exponent then gives the second parameter: $\sigma(\varepsilon) = e^{a\varepsilon} + k$. The two boundary conditions for this case are:

BC#3b:

$$\sigma(\varepsilon_f) = TS$$

BC#4:

$$\sigma(0) = 0$$

Applying these boundary conditions gives the base function and parameter values stated below.

$$\sigma(\varepsilon) = e^{\alpha\varepsilon} + k \qquad a = \frac{\ln(TS + 1)}{\varepsilon_f} \qquad k = -1$$

2.1.7 Integrals and Model Synthesis

This section completes the integrals of the stress strain functions and combines the model components developed up to this point for energy calculations. The integrals of the stress strain curves are presented below.

Brittle: $\sigma(\varepsilon) = Y_B \varepsilon$

$$\int_0^{\varepsilon_f} \boldsymbol{\sigma_1}\, d\varepsilon = \int_0^{\varepsilon_f} Y_B \varepsilon\, d\varepsilon = \frac{1}{2} TS_{cw} * \varepsilon_f$$

Slightly Ductile Brittle: $\sigma(\varepsilon) \approx \left\{ \begin{matrix} Y\varepsilon \\ a(\varepsilon - h)^{1/2} + k \end{matrix} \middle| \begin{matrix} 0 \le \varepsilon \le \varepsilon_y \\ \varepsilon_y < \varepsilon \le \varepsilon_f \end{matrix} \right\}$

$$\int_0^{\varepsilon_f} \boldsymbol{\sigma_2}\, d\varepsilon = \int_0^{\varepsilon_y} Y\varepsilon\, d\varepsilon + \int_{\varepsilon_y}^{\varepsilon_f} a(\varepsilon - h)^{1/2} + k \quad d\varepsilon$$

$$= \frac{Y}{2} {\varepsilon_y}^2 + \frac{2a}{3}\left(\varepsilon_f - h\right)^{3/2} + k\varepsilon_f - \frac{2a}{3}\left(\varepsilon_y - h\right)^{3/2} - k\varepsilon_y$$

Ductile: $\sigma(\varepsilon) \approx \left\{ \begin{matrix} Y\varepsilon \\ -a(\varepsilon - h)^2 + k \end{matrix} \middle| \begin{matrix} 0 \le \varepsilon \le \varepsilon_y \\ \varepsilon_y < \varepsilon \le \varepsilon_f \end{matrix} \right\}$

$$\int_0^{\varepsilon_f} \boldsymbol{\sigma_3}\, d\varepsilon = \int_0^{\varepsilon_y} Y\varepsilon\, d\varepsilon + \int_{\varepsilon_y}^{\varepsilon_f} -a(\varepsilon - h)^2 + k\, d\varepsilon$$

$$= \frac{Y}{2} {\varepsilon_y}^2 - \frac{a}{3}\left(\varepsilon_f - h\right)^3 + k\varepsilon_f + \frac{a}{3}\left(\varepsilon_y - h\right)^3 - k\varepsilon_y$$

Plastic: $\sigma(\varepsilon) \approx \left\{ \begin{matrix} Y\varepsilon \\ m\varepsilon + b \end{matrix} \middle| \begin{matrix} 0 \le \varepsilon \le \varepsilon_y \\ \varepsilon_y < \varepsilon \le \varepsilon_f \end{matrix} \right\}$

$$\int_0^{\varepsilon_f} \boldsymbol{\sigma_4}\, d\varepsilon = \int_0^{\varepsilon_y} Y\varepsilon\, d\varepsilon + \int_{\varepsilon_y}^{\varepsilon_f} m\varepsilon + b\, d\varepsilon$$

$$= \frac{Y}{2}{\varepsilon_y}^2 + \frac{m}{2}{\varepsilon_f}^2 + b\varepsilon_f - \frac{m}{2}{\varepsilon_y}^2 - b\varepsilon_y$$

Highly Elastic: $\sigma(\varepsilon) \approx e^{a\varepsilon} - 1$

$$\int_0^{\varepsilon_f} \boldsymbol{\sigma_5}\, d\varepsilon = \int_0^{\varepsilon_f} e^{a\varepsilon} - 1\, d\varepsilon = \frac{1}{a}(e^{a\varepsilon_f} - 1) - \varepsilon_f$$

Two assumptions are made to refine the curve equations: that the Young's modulus is twice the value calculated from the assumption of linearly elastic Brittle behavior ($Y = 2Y_B$) and that the stress at yielding takes a value of half the tensile stress ($\sigma_y = TS_{cw}/2$). These assumptions allow the construction of a first set of curves and the calculation of a first set of energy values.

2.1.8 Calculation

The model described above was coded in MATLAB for calculation and further analysis. The MATLAB output (Figure 2.6) confirms the proper shape of the assumed material behaviors and uses the parameter values listed in Table 2.2 to calculate the energy to rupture cells as J/m^3 of solution and pJ/cell directly.

Table 2.2 – Inputs for model calculation

Symbol	Value	Units	Symbol	Value	Units
TS_{cw}	638E6	N/m^2	T_{cw}	100E-9	m
Y	$2*(TS_{cw}/\varepsilon_f)$	N/m^2	$\rho_{c,d}$	1000	kg/m^3
f_f	1.0	--	h	100E-9	m
f_s	0.25	--	a_s	0.01	--
C_c	2.7	kg/m^3	a_c	0.01	--
f_w	0.9	--	ε_f	0.25	--
$d_{c,s}$	5E-6	m	σ_y	$TS_{cw}/2$	N/m^2
$d_{c,c}$	15E-6	m	ε_y	σ_y/Y	--
l	4*15E-6	m			

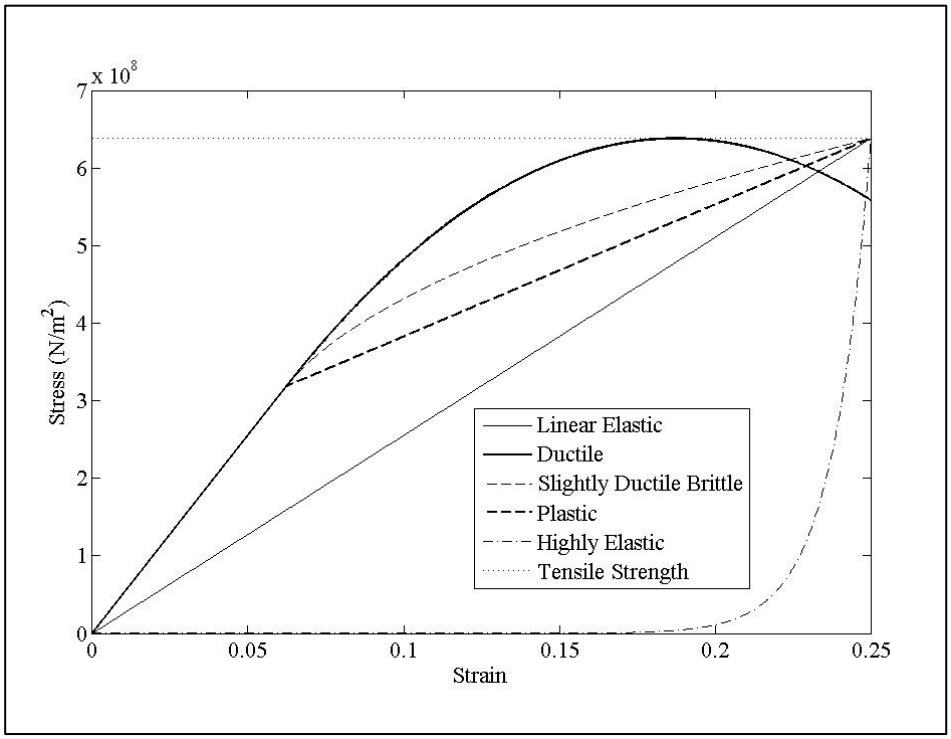

Figure 2.5 – Model output confirmation of parameterized stress strain curves

2.1.9 Results and Discussion

The model calculated cell rupture energy values for both spherical and cylindrical geometries are presented in Tables 2.3 and 2.4.

Table 2.3 – Spherical Cells Solution Rupture Energy [(J/m^3) / (pJ/cell)]. (Bold indicates values within a factor of 2 of the AFM measured value, corrected for cell diameter.)

Elongation Criteria	Assumed Height	Assumed Fraction	Strain Based
Linear Elastic	2584 / **6.264**	1015 / **2.460**	25370 / 61.49
Ductile	3714 / **9.004**	1459 / **3.536**	36470 / 88.40
Slightly Ductile Brittle	3445 / **8.351**	1353 / **3.280**	33820 / 81.99
Plastic	3230 / **7.829**	1268 / **3.075**	31710 / 76.87
Highly Elastic	254.9 / 0.6179	100.1 / 0.2426	2502 / **6.066**

Table 2.4 – Cylindrical Cells Solution Rupture Energy [(J/m^3) / (pJ/cell)]

Elongation Criteria	Assumed Height	Assumed Fraction	Strain Based
Linear Elastic	47.85 / 78.79	143.6 / 56.37	3589 / 1409
Ductile	68.78 / 27.01	206.4 / 81.03	5159 / 2026
Slightly Ductile Brittle	63.80 / 25.05	191.4 / 75.16	4785 / 1879
Plastic	59.81 / 23.49	179.4 / 70.46	4486 / 1762
Highly Elastic	4.720 / 1.854	14.16 / 5.561	354.0 / 139.0

The energy values for spherical cells cover a range of 2 orders of magnitude and those for cylindrical cells cover a range of 3 orders of magnitude. (Spherical: 0.24 – 88.40 pJ/cell; Cylindrical: 1.85 – 2025.87 pJ/cell)

These ranges can be compared to the calculated values from [38] with corrected tensile strength and measured values from atomic force microscopy [88]. In

order to compare these results on equal footing, the parameters must be normalized. The only non-material dependent parameter is the cell geometry. In the case of direct measurement with atomic force microscopy, the cell is an ellipsoid with maximum dimensions 10x8x6 μm. If it is assumed that the cell wall splits in an equatorial line along its longest perimeter (where the highest wall tension would be present), an analogous spherical radius can be calculated that would experience an equivalent wall stress. This is done by setting the equations for calculated stresses equal to each other and solving for the radius in terms of the largest cross section plane half length and half height (approximating the perimeter of an ellipse as $p \approx 2\pi\sqrt{\frac{b^2+c^2}{2}}$). This gives $r = bc\sqrt{\frac{2}{b^2+c^2}}$, which, for b=4μm and c=5μm, yields r=4.42μm. Note that simply equating ellipsoid perimeter and sphere circumference would not account for the difference in cross sectional area to which the internal pressure is applied. The energy values per cell calculated using this cell diameter (8.84μm), but maintaining all other parameter values, along with the parameter values used, are shown in Table 2.5. Final energy values are presented as pJ/cell.

Table 2.5 – Rupture Energy per Cell Comparison. (d_c = 8.84μm)

Reference Species	*Chlamydomonas eugametos*				*Tetraselmis suecica*
Cell Shape	Sphere				Ellipsoid
Equation	2.2	2.1	2.1	2.3	AFM measured
Y (GPa)	2.13	3.19	2.552	2.552; 5.104	
ε_f	0.3	0.002	0.25	0.25	
e_c (pJ/Cell)	923	0.0123	192	0.758-276	17.43

It can be seen from these results that Equation 2.2 produces a drastic overestimate of cell rupture energy when applied using the corrected tensile strength. Equation 2.1 is highly dependent on strain, as noted above, resulting in under- and overestimates when assuming low or high strain values. Equations 2.3 display a 3 order of magnitude range of cell rupture energy values.

The cell diameter input is the only difference between the values presented in Table 2.3 and Table 2.5. The ratio of the square of the diameters used provides an energy conversion ratio of 3.12. Applying this conversion to the AFM value in Table 2.5 yields 5.59pJ/cell. This energy value matches most closely with Table 2.3 values in the assumed height and assumed fraction columns, excluding the highly elastic category of stress-strain behavior; and the single value that is both highly elastic and strain based.

2.1.10 Conclusions

There are 2 sets of possible conclusions of equal merit, eliminating 6 combinations of volume and stress-strain behavior. Either 1) the volume of material considered in the rupture energy calculation is not strain based, and the cell wall does not exhibit highly elastic behavior; or 2) the volume of material is strain based and is highly elastic. It can also be observed from a comparison of Table 2.3 and Table 2.4 that cylindrical cells will require 1-2 orders of magnitude greater energy to rupture than spherical cells.

2.2 Ultrasound System Calorimetry

2.2.1 Introduction

The overall efficiency of biomass pretreatment systems is dependent not only on the resistance of biomass to treatment, but also on the energy transfer efficiency of the treatment system itself. Analysis of energy transfer in power ultrasound systems applied to suspensions of unicellular microalgae requires qualitative and quantitative consideration of several modes of energy transfer.

The application of power ultrasound (sonication) introduces pressure oscillations in solution at a high frequency and intensity. This causes extreme localized pressure fluctuations in solution. These pressure fluctuations lead to the formation and subsequent collapse of solvent vapor bubbles in solution (cavitation). The implosion of these bubbles results in localized shockwaves, thermal singularities, and high velocity micro-jets of solvent from asymmetric implosions. The shockwaves and jets exert force on cells, potentially rupturing them. Free radical formation is also induced at thermal singularities, leading to oxidation of solution constituents [98, 99].

Additional phenomena, such as acoustic streaming, acoustic heating, and waveform distortion, arise from non-linear interactions that become significant for the high intensity perturbations characteristic of power ultrasound [100].

The efficiency of ultrasound power transfer to solution is affected by ultrasound amplitude, ambient pressure, and temperature and viscosity of the medium [101, 102], reactor geometry [103], and media type and liquid height in the reactor

[104]. Frequency also has a strong effect on the efficiency of cavitation generation, with the inducement of cavitation at 10kHz requiring 10% of the ultrasound intensity required at 400kHz [98]. The relationship between cavitation threshold pressure and stimulation frequency in water is nearly flat up to ~100kHz, beyond which there is a drastic increase in pressure required at increasing frequencies [105].

Increasing ultrasound intensity (W/cm^2) influences the effectiveness of ultrasound by extending the reaction zone, thus increasing the number of cavitation events per volume [99]. This is one of the reasons for the use of booster horns with small effective area in ultrasound systems [98]. For a smaller probe, the same power applied at the ultrasound generator experiences less impedance, allowing for more displacement at the same frequency. Increased displacement corresponds to higher acoustic energy, and that acoustic energy is applied over a smaller area. However, the high intensity provided by these booster horns makes them susceptible to erosion; and this erosion alters the tip geometry, potentially altering the delivered ultrasound intensity.

The front end efficiency of the ultrasound generator is also important as an economic consideration. This takes lesser precedence in theoretical and experimental investigations, but is essential to the viability of scale-up.

The boundaries of operationally useful conditions are defined on one end by the inducement of cavitation and the other end by the decoupling of the ultrasound surface from the solvent at the solid-liquid interface, replacing cavitation with agitation.

In order to determine the transfer efficiency of energy applied for cell rupture, that energy is measured to select and characterize an ultrasound pretreatment system.

The objectives of this study are to: 1) quantify power transfer to solution in ultrasound probe-reactor systems, 2) select an appropriate reactor system for future experiments with microalgae, 3) characterize power transfer efficiency of the ultrasound probe-reactor systems, and 4) determine whether ultrasound probe tip erosion affects power transfer efficiency.

2.2.2 Theory

The incidence and intensity of cavitation due to power ultrasound are dependent on ambient pressure, frequency and amplitude of oscillation, and the density, viscosity, and vapor pressure of the solution solvent. Descriptions of these relationships generally start from the Raleigh-Plesset equation for the stable oscillation of a cavitation bubble [106].

$$R\ddot{R} + \frac{3}{2}\dot{R}^2 = \frac{1}{\rho_l}\left[p_b(t) - \frac{2\sigma}{R} - 4\mu_l\frac{\dot{R}}{R} - p(t)\right]$$

According to this equation, the cavitation bubble radius (R) can be determined as a function of time. From this radius, theoretical collapse energy can be calculated. In the case of a known solvent within a limited operational temperature range, the density (ρ_l), viscosity (μ_l), vapor pressure (p_b) , and ambient pressure can be taken as constant. Thus the bubble radii and corresponding collapse energies are a function of $p(t)$, an external pressure driving function dependent on the ultrasound frequency and amplitude.

While acoustic heating has been characterized as the result of non-linear interactions of the acoustic and entropy modes of strong perturbations under the momentum conservation, mass conservation, and entropy equations [100], power dissipation to solution by a sonicator can be more easily and directly quantified via the calorimetric method [69, 107].

$$\iiint_V \rho_l C_{v_l} \frac{dT}{dt} = P_{diss} + \dot{Q}$$

The terms of this energy balance equation are the integral of sonotrode power input, power dissipation to solution (P_{diss}), and thermal energy flux out of the system ($\dot{Q}$); where ρ_l is the liquid medium density, C_{v_l} is the constant volume specific heat of the liquid medium, T is temperature, t is time, and V is volume of solution. The experimental measurement of P_{diss} is performed as a temperature measurement over the initial treatment time with the assumptions that temperature is uniform within the reactor (complete mixing), heat energy flux out of the system is negligible during the initial treatment time, and density and specific heat are constant. This yields a simplified equation where the slope of the linear segment of the temperature curve over time can be used to calculate power dissipated to solution:

$$P_{diss} = V \rho_l C_{v_l} \frac{\Delta T}{\Delta t}$$

2.2.3 Experimental Approach

The calorimetric method is used to determine power transferred to solution for a series of laboratory vessels and liquid volumes. Average electrical power draw of the

sonotrode system is used to assess system efficiency, and power transfer is assessed on a gross basis. Qualitative visual observations of mixing and probe-liquid coupling are made to assess validity of results and appropriateness of vessel-volume combinations for future investigations. Comparison is made between power transfer of smooth and strongly eroded sonotrode tip faces.

2.2.4 Materials and Methods

The experimental apparatus consists of a longitudinally oscillating probe sonotrode (QSonica Q55 with 1/8 inch microtip) and digital probe thermometer (VWR Precision 0.01 and Robothermometer) suspended in parallel with a separation of ~1.5cm by ring clamps over a lab jack with a neoprene deck pad to hold the reactor vessels.

Power transfer to solution was measured using the calorimetric method as the change in temperature during treatment. All test were performed in randomized order at a power setting of 100 with the probe tip immersed 1.5cm below the liquid free surface and clearance of at least 1cm from the reactor bottom. The placement of the horn tip has been shown to not influence power measurements [104, 108]. However, initial trials showed poor mixing with placement of the horn tip within 1cm of the reactor bottom; and decoupling of the horn from the liquid by entrainment of ambient air due to breakage of the liquid surface around the probe when the tip face was within 1cm of the free surface.

The dependence of energy transfer on reactor type and solution volume was investigated using the following vessels filled with 25ml, 50ml, 100ml, or 200ml tap

water as outlined in the experimental design: 50ml plastic centrifuge tube (NUNC), 100ml glass beaker (VWR), 400ml glass beaker (VWR), and 50ml glass jacketed beaker (Kimble). Temperature stabilization to room temperature (22-28^{o}C) was observed for 30 minutes prior to treatment for all except the jacketed beaker. A re-circulating bath was used to bring the jacketed beaker sample to a stable temperature of 25^{o}C then deactivated during treatment. Sample volumes were treated for 20s, as outlined in the experimental design (Table 2.6).

Power draw of the system was measured as apparent power via rms voltage and rms current measurements taken during operation using a digital multimeter with probes contacting the lines coming in to the AC adapter in parallel and series, respectively.

$$P_{apparent} = V_{RMS} \times I_{RMS}$$

Current and voltage were measured at power settings from 10 to 100 at intervals of 10 with the probe tip immersed 1.5cm below the surface of a 500ml tap water reservoir. Power transfer efficiency was calculated as

$$\eta = \frac{P_{diss}}{P_{apparent}}$$

Ultrasound probe tip surfaces are prone to significant erosion on the tip face. Because this face is the cavitation inducing surface, modifications to this interface have the potential to alter power transfer and cavitation. To determine whether this

was occurring, a side by side comparison of calorimetry results was performed in 50ml of tap water in the 50ml glass jacketed beaker (Kimble).

Linear least squares regression was performed on pooled calorimetry time series' for each experimental condition. Determination of difference in calorimetric time series' between new and eroded sonotrode tips was performed visually. All error bars have length of one standard deviation.

Table 2.6 – Experimental Design

Vessel	Liquid Volume (ml)	Treatment Duration (s)	Number of Replicates
50ml Centrifuge Tube	25	20	3
	50	20	6
100ml Beaker	50	20	6
	100	20	6
400ml Beaker	100	20	6
	200	20	3
50ml Jacketed Beaker – new tip	50	20	3
50ml Jacketed Beaker – eroded tip	50	20	3

2.2.5 Results and Discussion

Ultrasound power transfer to solution was determined calorimetrically for multiple experimental systems. Power dissipated to solution ranged from 5.59 - 9.27W (Figure 2.7). Results from these tests were used to select an appropriate reactor and liquid volume combination for future tests processing microalgae.

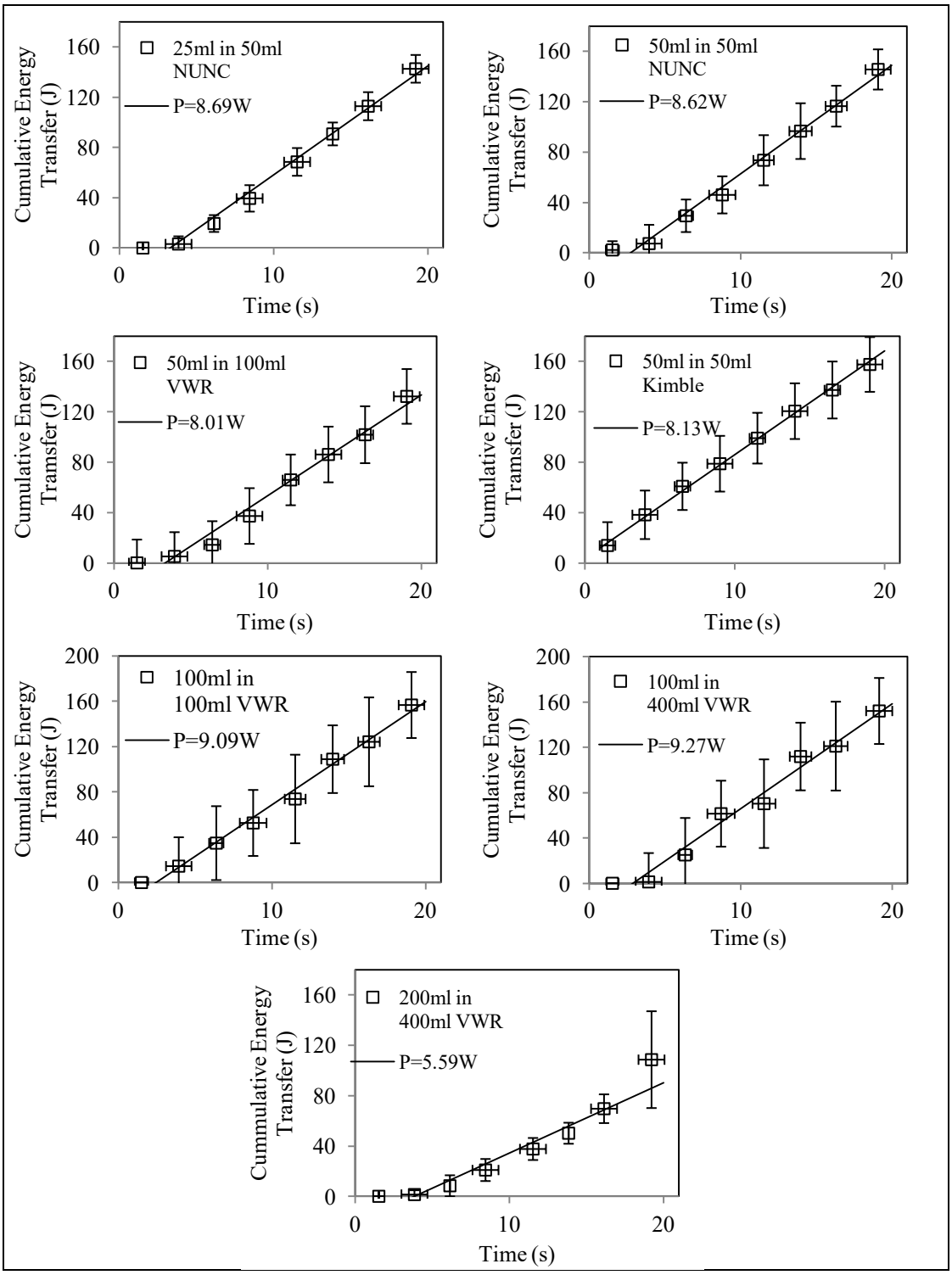

Figure 2.6 – Cumulative energy transferred to solution by Q55 sonotrode at setting of 100 using 1/8 inch microtip immersed1.5cm in specified volume of tap water and reactor. Horizontal error bars are one standard deviation of time lumped for visualization, but not for regression

At a given frequency, varying amplitude will vary power (W), and probe tip face area determines the intensity (W/cm^2) of that power [109, 110]. When treating varying volumes of liquid, the power dissipated to solution is often normalized by volume to give an ultrasound dose or specific power (W/ml) [102, 104].

When normalized, the power transfer values observed here correspond to ultrasound intensities of 70.6 - 117 W/cm^2 over an area of 0.0792cm^2 and ultrasound doses of 0.112 – 0.185 W/ml in 50ml. This intensity is well above the threshold intensity of 4 W/cm^2 required to induce cavitation in air-free water [98].

From the perspective of the reactor as a closed system, the presence of such significant variation in energy accumulation for what should be a constant mechanical power input seems to violate the conservation of energy. If it is assumed that the heat losses from the system are still negligible during the measurement period, then the discrepancy of energy must be explained through the differential parsing of acoustic energy into its dominant non-linear interaction modes. These are: acoustic streaming (hydrodynamic flows), sound-sound interactions (soundwave distortion), and acoustic heating (heat transfer) [100]. Higher acoustic streaming would display as lower mixing delay. Higher acoustic heating would display as higher calorimetric power. Increased sound-sound interactions would not display directly under the measurements taken, but would imply increased instability and inconsistency of pressure oscillations. Since consistent pressure oscillations are required for the successive formation and collapse of cavitation bubbles, sound-sound interaction could imply lower cavitation activity. When a Punnett square of the two measured non-linear behaviors is

superimposed on a plot of calorimetric power versus mixing delay, the reactor combinations are easily separated into pairings of heating and streaming behaviors (Figure 2.8). If it is assumed that the energy of the 3 dominant nonlinear behaviors are conserved together, then an ideal reactor would display high heating and high streaming, minimizing the energy available for sound-sound interactions that might interfere with cavitation.

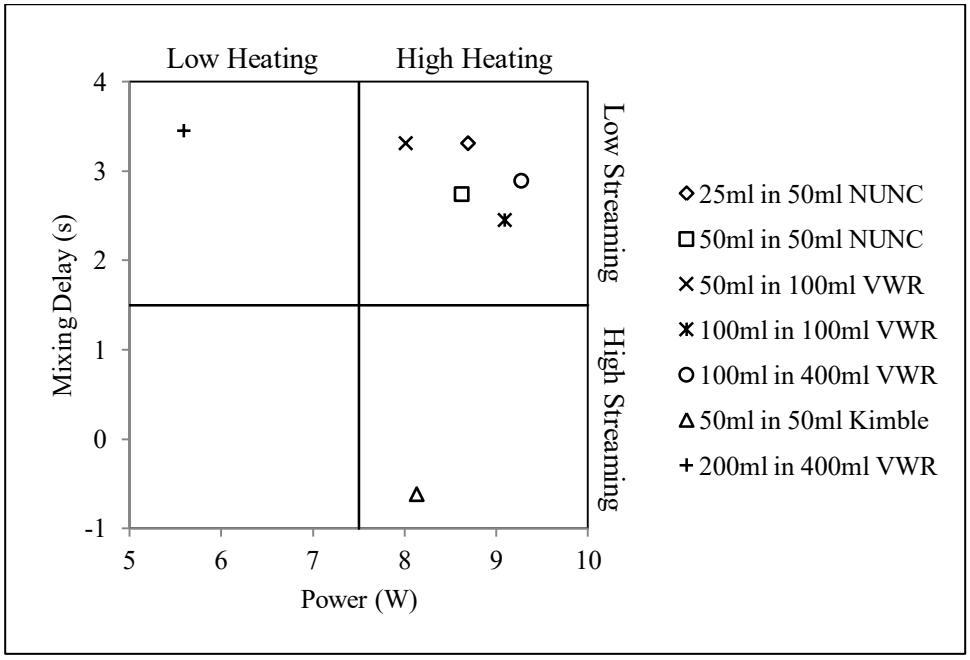

Figure 2.7 – Categorization of reactors according to non-linear interactions

Only one reactor – liquid volume combination falls into the categories of both high heating and high streaming. This was the Kimble jacketed beaker with a solution volume of 50ml, which also showed negligible delay in temperature increase during calorimetry (Table 2.7). Because the reactor system will be used to investigate energy models of microalgae processing, fulfillment of the assumption of complete mixing with minimal to no transient startup is essential. Because of these combined

characteristics and its capacity for temperature control, the 50ml Kimble jacketed beaker is selected for future studies despite its only moderate power transfer of 8.13W.

Table 2.7 – Linear regression coefficients for cumulative energy transfer and average power transfer efficiency (η). Power transfer to solution is given by the slope, and mixing delay is given by the x-intercept

Name	Power (W)	Mixing Delay (s)	R^2	η
25ml in 50ml NUNC	8.69	3.31	0.9720	0.343
50ml in 50ml NUNC	8.62	2.74	0.9141	0.341
50ml in 50ml Kimble	8.13	-0.619	0.8625	0.321
50ml in 100ml VWR	8.01	3.31	0.8268	0.317
100ml in 100ml VWR	9.09	2.45	0.7667	0.359
100ml in 400ml VWR	9.27	2.89	0.8995	0.366
200ml in 400ml VWR	5.59	3.45	0.9211	0.221

The efficiency of the QSonica Q55 system in converting electrical energy to heat dissipated to solution ranged from 22.1 – 36.6% (Table 2.7), based on apparent power measured at a setting of 100 (Figure 2.9). The QSonica Q55 system generator has a power rating of 55W, however, the nominal power of the generator is not specified. The high voltage (700Vrms) and frequency (20kHz) output of the sealed generator makes measurement of nominal power both hazardous and impractical in our lab and these characterizations have been performed elsewhere [102, 111].

While the calorimetric efficiency of this specific laboratory system is not directly applicable to energy requirements for biomass processing at scale, it is a necessary step in the energy analysis of the process. In order to fully contextualize the calorimetric measurements provided here in the frame of effective energy efficiency of biomass pretreatment for microalgae cell disruption, knowledge of the energy conversion efficiency will be required in addition to measurements of process yield

[102]. As noted above, calorimetric measurement of ultrasound power dissipation to solution does not capture all forms of energy imparted to the treated volume. It is common practice to take calorimetric measurements as representative of cavitation activity in the non-linear operating mode (past the cavitation threshold) [111], and correlations have been presented to support this [112]. However, in order to eventually optimize a real process, a differentiation between thermal, cavitation, and effective process efficiencies will be required [102].

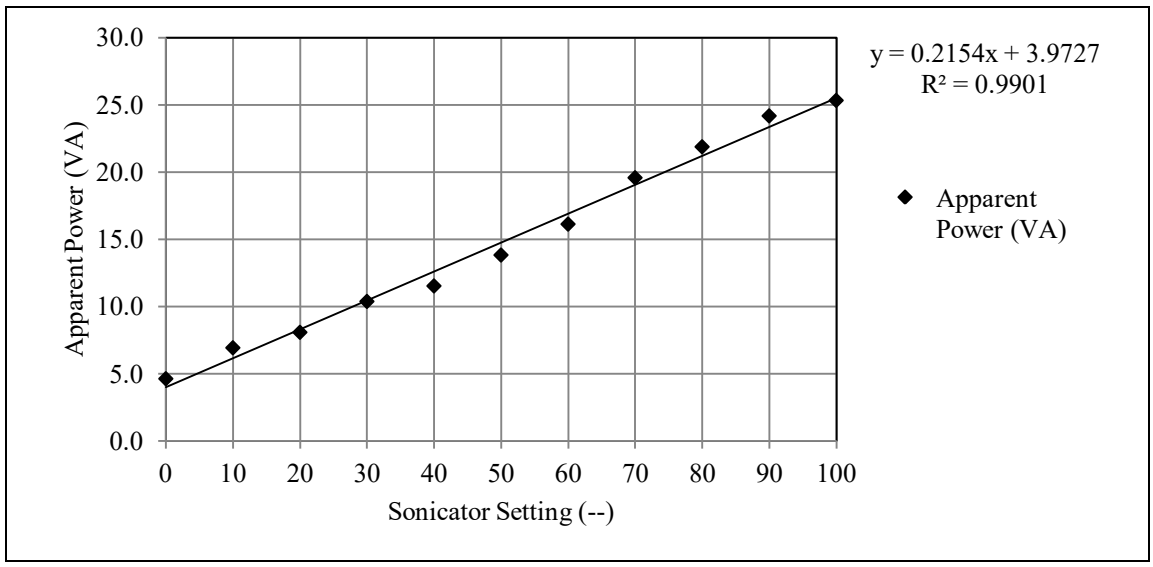

Figure 2.8 – Apparent power draw of Q55 sonotrode over full performance range using 1/8 inch microtip immersed 1.5cm in 500ml tap water reservoir

The comparison of power transfer by a new sonotrode tip to that of an eroded tip yielded inconclusive results (Figure 2.10, Table 2.8). The eroded tip does appear to provide lower power. However, high variance in the experimental measurements prevents confirmation of this difference to a sufficient degree of certainty. Probe tips are constructed of a titanium alloy or silica, specifically chosen to resist erosion [98].

However, the tips are considered to be a disposable component due to the significant erosive potential of the ultrasound and cavitation action.

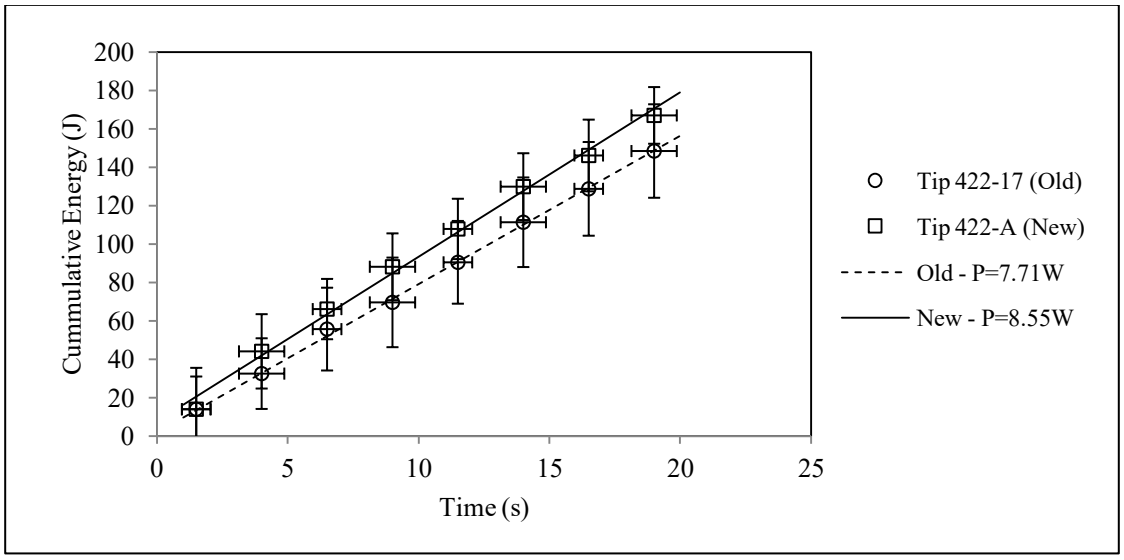

Figure 2.9 – Cumulative energy transferred to solution by Q55 sonotrode at setting of 100 using 1/8 inch microtip immersed1.5cm in 50ml in 50ml Kimble jacketed beaker using new and eroded sonotrode tips

Table 2.8 – Linear regression coefficients for cumulative energy transfer and average power transfer efficiency (η). Power transfer to solution is given by the slope, and mixing delay is given by the x-intercept

Name	Power (W)	Mixing Delay (s)	R^2	η
422-17 (old)	7.71	-0.275	0.8338	0.305
422-A (new)	8.55	-0.929	0.9280	0.338

One of the challenges associated with sonotrode tip erosion is the complex geometry of a cavitation eroded surface, which is difficult to characterize and measure. The three possibilities of reaction to this changed geometry are decreased, increased, and static cavitation activity. A decrease in cavitation activity could occur from interference of multiple acoustic waves leaving the eroded face. On close

inspection, the eroded face is pitted with multiple concave impressions, and concave surfaces focus acoustic energy. The pitting of the probe surface may convert it from a single flat generating surface to a field of multiple focused generating surfaces.

It is also possible that both of these mechanisms and/or others effectively cancel each other out to differing degrees with a random net result. This is borne out by qualitative observation of the cavitation zones of the flat and eroded tip faces. The flat face produces a cavitation zone visible as a dense cloud of bubbles that is axi-symmetrically conical with height approximately equal to the diameter of the probe face. This conical shape is mirrored across a plane perpendicular to the probe axis at the apex of the cavitation zone. The mirrored cone appears to be a region of concentrated acoustic streaming, visible as a refractive distortion of the fluid and by entrained dispersed bubbles. The cavitation zone of the eroded face is also symmetric, but forms a semi-ellipsoid dome with height approximately half the diameter of the probe. The acoustic streaming from the eroded tip is not axially symmetric, but maintains a somewhat conical shape with its apex superimposed somewhere within the last several millimeters of the probe body. Cavitation is visually confirmed in both cases, but the relative levels of cavitation are unknown. The degree of change in energy partitioning between non-linear interaction effects is also unknown with both conditions still falling within the high heating, high streaming zone of Figure 2.8.

2.2.6 Conclusions

The calorimetric power transferred to solution in the tested experimental systems ranged from 5.59-9.27 W. Additional differentiation by mixing delay and

analysis of the results in the context of non-linear acoustic theory led to classification of reactors in terms of acoustic streaming and acoustic heating. The 50ml Kimble jacketed beaker was chosen for future tests based on inferred lower interference with cavitation due to high streaming and heating behavior. Calorimetric efficiencies of the systems were relatively consistent, and the power transfer of a smooth probe tip could not be differentiated from that of an eroded tip face. A mechanism was proposed to explain this lack of difference between smooth and eroded tip faces. Additional characterization of energy partitioning between linear and non-linear acoustic phenomena is required moving forward in the field, but the inferences presented here facilitate decision making and classification where direct measurement is impossible or impractical.

2.3 Ultrasound Processing of *Chlorella vulgaris*

2.3.1 Introduction

Energy commodities and co-products produced from microalgae are the result of extraction processes that often begin in pretreatment of biomass with the intent to rupture individual cells. The rupture of cells makes cellular products more accessible for extraction and the efficiencies of pretreatment and extraction are essential to process feasibility.

The challenge of generalizing energy relationships in microalgae biomass processing stems from a lack of understanding of the physical responses of microalgae to applied pretreatment energy. There have been a large number of efforts to characterize pretreatment system performance, but these works have focused on single system-species-extract combinations, while neglecting energy relationships. If the underlying behavior of cells in pretreatment were better understood, the requirement for individual characterizations could be minimized and system level extrapolations could be made more accurately. The capacity for inference from these pretreatment characterizations would also greatly benefit from the inclusion of energy analysis.

Power ultrasound is a widely used system for cell disruption in molecular biology and has been adopted for microalgae biomass pretreatment in fuel and co-products extraction. Low frequency power ultrasound is most efficient at generating the cavitation operative in cell rupture. *Chlorella vulgaris* is both widely used as a test organism and the subject of biofuels investigations based on its ability to accumulate

lipids that can be extracted as bio-oil. This study fills the gap in current knowledge using ultrasound processing of *Chlorella vulagaris* to validate cell rupture energy calculated using a constitutive model.

In order to explore the energy efficiency of cell rupture pretreatment, this study addresses the following objectives: 1) Characterize the rate of cell rupture under low frequency power ultrasound treatment; 2) Determine the power ultrasound energy required to rupture microalgae cells; and 3) Evaluate modeled cell rupture energy requirements in the context of power ultrasound pretreatment processes.

2.3.2 Experimental Approach

Chlorella vulgaris was grown in semi-continuous batch aerated cultures. Harvested biomass was treated with power ultrasound in triplicate for 30 minutes in each replicate. Samples were taken every 3 minutes and analyzed for cell concentration and percent viability. The time series of cell rupture was fitted to a first order empirical disruption model. Cell disruption data was analyzed for average energy requirements for cell rupture and compared to theoretical predictions.

2.3.3 Materials and Methods

Microalgae Growth

Chlorella vulgaris was obtained from Carolina Biological and grown in Bold's Basal Medium [113] (modified to 1/6 trace metals concentration) from a single colony isolate. All media were autoclaved at 121^{o}C for 30 minutes before inoculation using aseptic technique. 3.0L cultures were grown in foam stopped 4L round glass bottles,

mixed by convection induced by HEPA filtered air bubbling through a ¼ inch diameter open ended glass weighted tube terminating at the bottom of the vessel wall. Lighting was on a 14hr/10hr on/off cycle via 2x 40W, 2600 lumen, 4100K fluorescent light tubes suspended ~3ft above the cultures. Ambient temperature regularly fluctuated in the range of 20-25^{o}C. Semi-continuous batch operation was maintained in exponential growth phase using 1.5L of each culture volume remaining as inoculum after harvest.

Cultures were monitored using spectrophotometric absorbance (300nm-800nm, BioMate3S). Spectra were monitored for aberrant peaks that could indicate contamination. Biomass was measured as absorbance at 750nm.

Power Ultrasound

Low frequency power ultrasound treatment was performed using a 20kHz sonotrode system (Qsonica Q55) with 1/8 inch micro-tip. The tip was immersed to a depth of 1.5cm in 50ml samples in a 50ml jacketed beaker with recirculating water at 25.5^{o}C (sample temperature 25^{o}C). Treatment was performed in triplicate at a setting of 100 (8.13W, 103 W/cm^{2}, 0.163 W/ml) for 30 minutes. Temperature was monitored to check for overheating (max. 28.5^{o}C). Power transfer to solution was determined calorimetrically [101] in a separate test.

Analysis

Cell concentrations and % viability were determined optically via automated cell counts (Nexcellom Cellometer AutoX4) in duplicate. 20µl of culture sample was

combined with 20µl propidium iodide (PI) stain (Cellometer ViaStain™ PI Staining Solution) in a 1.5ml microcentrifuge tube and vortexed for 10 seconds. A 20µl sample was then pipetted to a Cellometer counting chamber and allowed to stabilize for 2 minutes. A bright field cell count was executed, followed by stimulation of the sample at 501nm and emission measurement at 595nm for 10 seconds of exposure. Dead cells were identified via fluorescence of PI in an automated count of fluorescing cells. Percent viability was determined as the difference between the bright field and fluorescence cell counts divided by the bright field cell count.

2.3.4 Results and Discussion

Power Ultrasound

The total number of cells disrupted at the end of 30 min treatment of a 50ml volume averaged 4.67 $x10^8$. The treatment provided 8.13W to solution, resulting in an average energy requirement of 31.3 µJ per cell disrupted. This value is 4 orders of magnitude higher than constitutive model predictions of picojoules to rupture a single cell. However, examination of the cell disruption curve shows it to be non-linear (Figure 2.11), making the direct average comparison less appropriate.

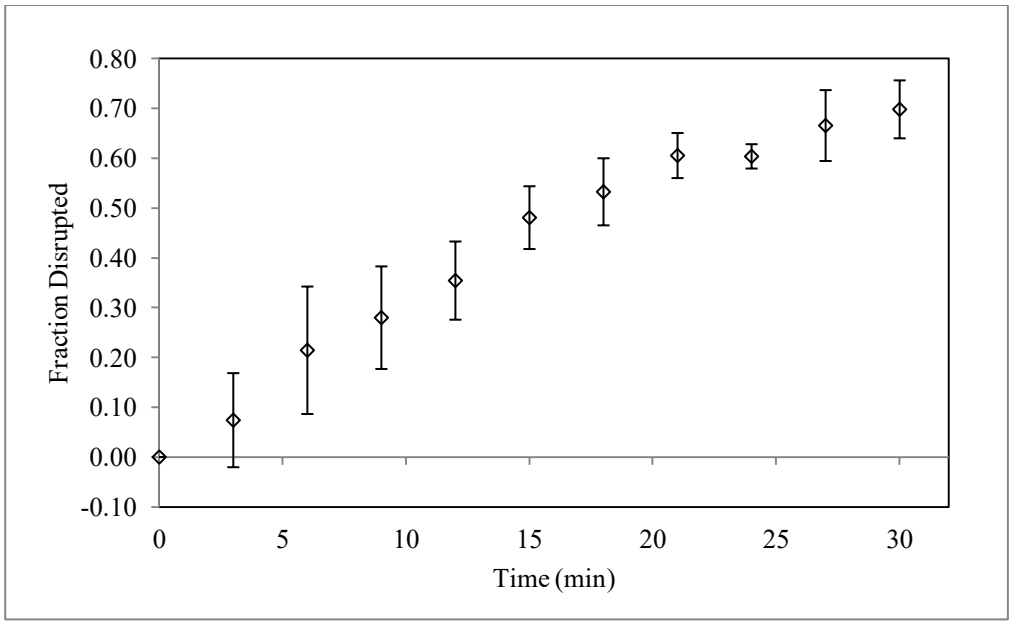

Figure 2.10 – Cell disruption over time under power ultrasound

A first order empirical disruption model is applied to express disruption rate as a function of disrupted cell concentration (N_d): $\frac{dN_d}{dt} = k(N_0 - N_d)$; $N_d = N_0 - N_c$; $D = (N_0 - N_c)/N$ [89]. The initial whole cell concentration is N_0, D is the disrupted fraction, and the solution to this equation for $N_d(t = 0) = 0$ is $D = 1 - e^{-kt}$. This model generally fits disruption data well with the reaction constant being a function of starting cell concentration and ultrasound frequency and intensity [64]. The value of the disruption rate constant observed here is 0.0411 min^{-1} (Figure 2.12).

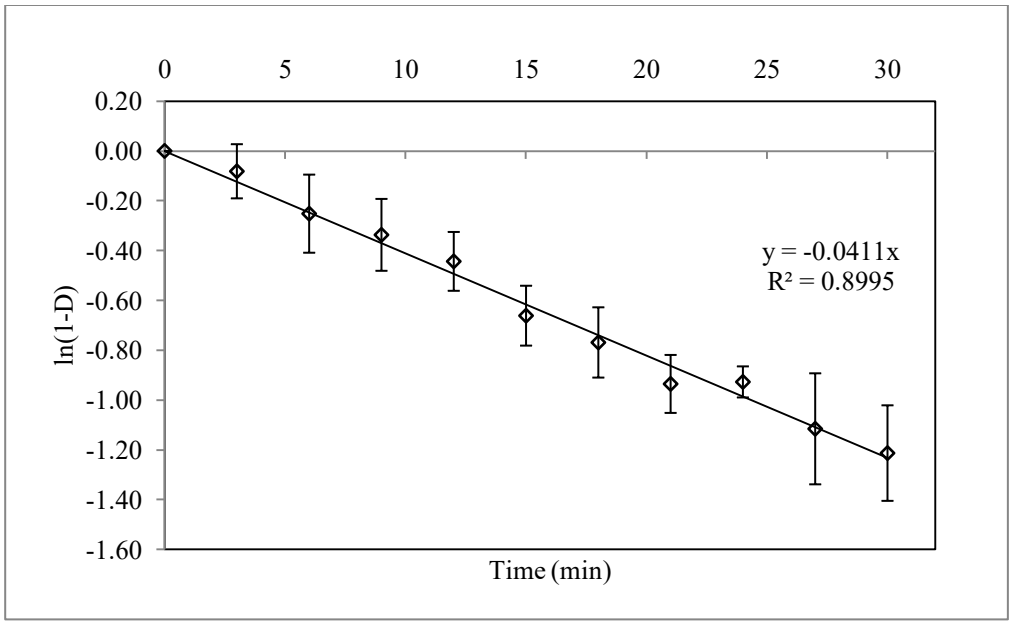

Figure 2.11 – First order empirical cell disruption model

Where $E = P * t$ and $N_d = N_0\left(1 - exp(-kt)\right)$, the average cumulative energy expended per cell ruptured over time is $\frac{E}{V*N_d} = \frac{P*t}{V*N_0\left(1-e^{-kt}\right)}$. The instantaneous expended energy per cell ruptured is described by a different function of time, $e_c(t) = \frac{de/dt}{dN_d/dt} = \frac{de}{dN_d} = \frac{P}{kN_0} exp(kt)$, and e_c increases exponentially as a function of time. A comparison of this model prediction versus an approximation of $\Delta e/\Delta N_d$ is presented in Figure 2.13.

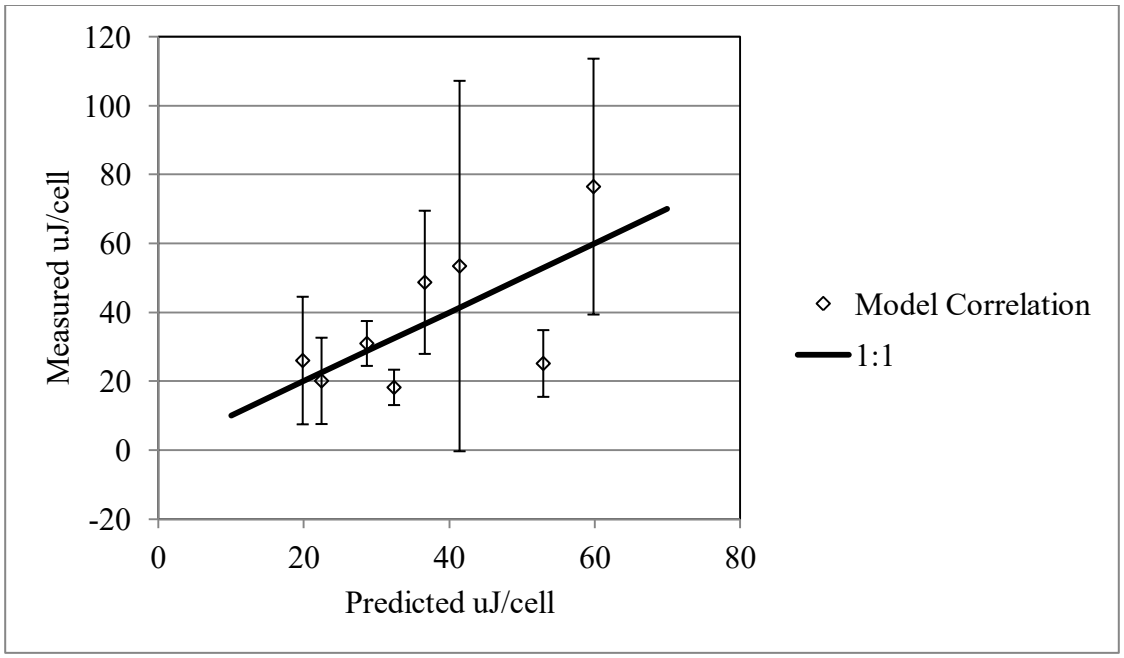

Figure 2.12 – Model predicted versus measured marginal rupture energy per cell over time under power ultrasound treatment

The average measured rupture energies (excluding outliers) range from 18μJ/cell to 76μJ/cell, showing that use of the cumulative average of 31.3μJ/cell misses important operational realities, and the general reporting of average energy values out of context is inappropriate because of its dependence on k, N_0, and t .

The model fit is immediately recognized as poor and the high observed variance points out the limitations of applying a deterministic model to a high variance system. This high variance should be incorporated into future model predictions of cell rupture energy requirements.

2.3.5 Conclusions

The power ultrasound treatment of *Chlorella vulgaris* required an average ultrasound energy input per cell ruptured ranging from 18 to 76μJ. The 4 order of

magnitude difference between observed and predicted energy requirement may be due to power transfer efficiencies inherent in the treatment method. The rupture rate fits a first order disruption model relatively well. However, high variance observed in cell rupture energy requirement implies a need to expand the constitutive model of cell rupture to incorporate the variability of model inputs. Additional model expansion may be required to incorporate the observed first order disruption behavior.

Chapter 2, in part, has been submitted for publication of the material as it may appear in Biomass & Bioenergy, 2017, Klinger, Rory; Garoma, Temesgen, Elsevier, 2017; and in Ultrasonics Sonochemistry, 2017, Klinger, Rory; Garoma, Temesgen, Elsevier, 2017. The dissertation author was the primary investigator and author of this material.

Chapter 3 - **Sensitivity Analysis**

3.1 Introduction

Because the inputs and control systems of physical processes display inherent variation, so too do the outputs of those processes. The pretreatment of microalgae biomass for extraction is not an exception to this rule, and its variation should be accounted for in design decisions. A more routine industrial approach to accommodating this process variation is the use of systematic testing to assess variation and control plots to implement quality control, and this approach is reflected in the literature. However, this approach interprets the process as a black box, precluding the evaluation of sub-process mechanisms. In order to evaluate the component energy relationships of the cell rupture process, a deterministic model is presented. This model assesses the energy requirements for rupture of a single microalgae cell with assumed properties. An analysis of the sensitivity of this model to its various inputs is performed here to capture process input and output variation. This will expand the ability of the model to reflect measured variation in cell properties across multiple species, extrapolate process scale energy requirements with more precision and accuracy, and allow simulation based process optimization across species. This chapter presents both analytical and statistical sensitivity analysis of the constitutive model of cell rupture energy. The physical measurement of a high sensitivity input is then performed and used as a statistical input to Monte Carlo

simulations of the energy requirement for rupture of a physically diverse axenic population of unicellular microalgae.

3.2 Sensitivity Analysis of Constitutive Model

The influence of intra- and interspecies variation of geometry and material properties on single cell rupture energy for unicellular microalgae is evaluated here. An attempt to determine the controlling parameters of a constitutive model of cell rupture energy analytically leads to a simplified model representation. This simplified model is assessed for sensitivity analytically.

The original constitutive model is then evaluated via formal sensitivity analyses. An initial assessment of sensitivity is obtained by adjusting one input at a time (OVAT) with all other parameters held constant to evaluate the effect on rupture energy for a single cell. The entire input space is then further explored using scatter plots of a single variable versus rupture energy with all other inputs sampled randomly (uniformly) within a set range.

3.2.1 Methods

The categories of model inputs evaluated for sensitivity are cell geometry, material properties, and failure extent. The influence of cell geometry is tested using 1) cell diameter (d_c) and 2) wall thickness (T_{cw}). The influence of material properties is tested using 3) tensile strength (TS_{cw}) and 4) failure strain (ε_f). The influence of failure extent is tested using 5) the fraction of circumference split (f_s). The objective is to

understand the relative sensitivity of each model variant to each input, and to order those inputs to identify the highest priority for further investigation.

An initial evaluation of sensitivity is performed analytically. The model equations are separated into equations for volume of disrupted material and energy/volume integrals of stress-strain behavior. Order dependence on each input in a simplified model is then assessed and used as a comparison for formal sensitivity analysis of the original constitutive model.

OVAT line plots are produced by holding all non-varied inputs at their central values and varying one input uniformly between the low and high values in Table 3.1.

Table 3.1 – Input Ranges for Sensitivity Analysis

	Low (-90%)	Central	High (+90%)
d_c	1E-6 m	10E-6 m	19E-6
T_{cw}	10E-9 m	100E-9 m	190E-9 m
TS_{cw}	63.8E6 Pa	638E6 Pa	1212E6 Pa
ε_f	0.025	0.25	0.475
f_s	0.025	0.25	0.475

Confounding is explored by varying 2 inputs at a time. Energy values are calculated for the entire 2D I/O space for the model.

The entire input space is then explored using scatter plots of a single input versus rupture energy with all other inputs varied randomly (uniformly) within the Table 3.1 range.

3.2.2 Results and Discussion

The order influence of inputs is directly seen in the volume equations, as presented in Table 3.2. However, inspection of the energy/volume integrals shows a much less straight forward input order, preventing adequate sensitivity analysis by order alone.

Table 3.2 – Model Sensitivity Order by Variable in Volume of Disrupted Material

d_c	2
T_{cw}	1
TS_{cw}	0
ε_f	1
f_s	1

When reexamining the parameterized model equations, the integrals of stress-strain curves can all be alternatively parameterized to $\int \sigma d\varepsilon = \beta TS_{cw}\varepsilon_f$, where $0 < \beta \leq 1$. A simplified model equation is produced by recognizing the following: β does not depend on f_s, T_{cw}, or d_c; V_{dm} is not dependent on TS_{cw}; and V_{dm} does depend on ε_f in the case of strain based fraction of material. This simplified model equation is: $e_{c,i} = \beta TS_{cw}\varepsilon_f * V_{dm,i}(f_s, T_{cw}, d_c, \varepsilon_f)$. Varying this parameterized model one variable at a time should produce the order dependence shown in Table 3.3.

Table 3.3 – Simplified model order of dependence on inputs: TS_{cw} / T_{cw} / f_s / ε_f / d_c

	V_{dm} Model Variant		
Material Behavior	Fixed height	Defined fraction	Strain based
Linear Elastic	1/1/1/1/1	1/1/1/1/2	1/1/1/2/2
Ductile	1/1/1/1/1	1/1/1/1/2	1/1/1/2/2
Slightly Ductile Brittle	1/1/1/1/1	1/1/1/1/2	1/1/1/2/2
Plastic	1/1/1/1/1	1/1/1/1/2	1/1/1/2/2
Highly Elastic	1/1/1/1/1	1/1/1/1/2	1/1/1/2/2

An example of OVAT line plots of rupture energy per cell with model inputs varied one at a time (as a uniformly distributed set of points between the low and high values in Table 3.1) is shown in Figure 3.1. When examined with the order representations in Table 3.3, the curves produced by varying one parameter at a time match these order dependencies.

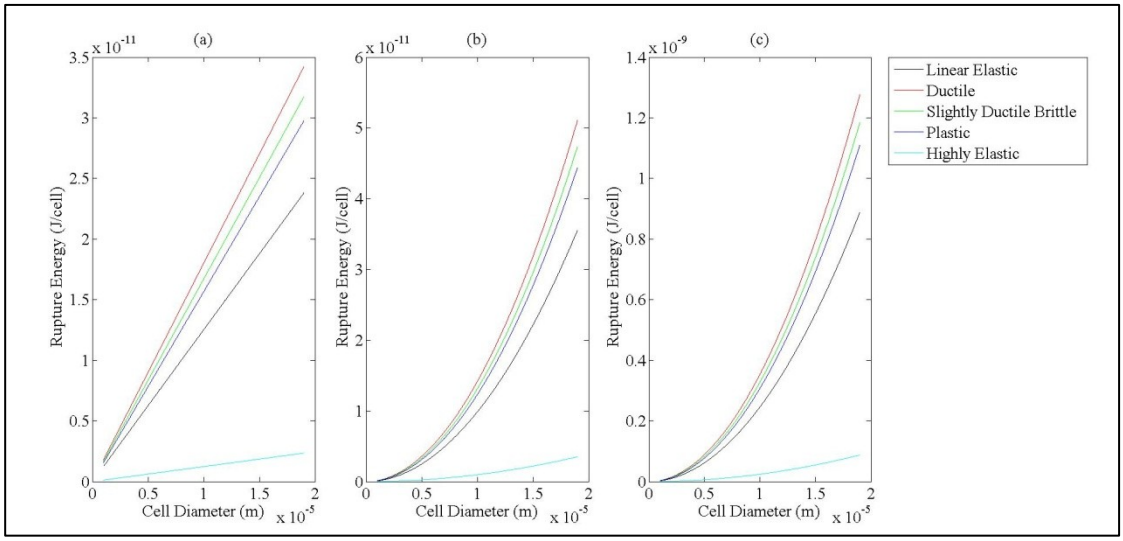

Figure 3.1 – Constitutive model cell rupture energy versus cell diameter for 15 model variants: (a) assumed height of material at h = 100nm, (b) circumference fraction of material at α = 0.01, (c) strain based fraction of material at ε_f = 0.25

Variations of cell diameter and failure strain produce non-linear responses (approximately 2^{nd} order), so these will be the most influential parameters, but only in the circumference fraction and strain based fraction model variants.

Similar patterns are observed across model variants and may be due to the structure of the equations and the choice to vary each input by ±90% of the central value. The uniform application of this choice has the effect of multiplying the energy equation by the same linear set of fractions between 0.1 and 1.9 regardless of which parameter is varied. This effect is compounded in the non-linear relationships, leading to different magnitudes between similar shaped non-linear curves. However, identical fractional changes in inputs sharing the same order of influence will produce the same overall effect on model output.

Varying more than one input at a time will compound the effects of each scaling. Three sets of order dependences are seen in Table 3.3, each with 5 potentially varying inputs. This gives 2^5=32 combinations of binary input states (constant or varied) for each model variant, implying 3*32=96 total sets of scaling factors. However, when the orders of impact of each varied input under each model variant are matched and summed for each input state, only 8 distinct outcomes are observed, ranging from 0 to 7^{th} order (Figure 3.2). This number is the result of having only 3 potential orders of influence, the consistently shared first order influence of 3 inputs across all model variants, and an assumption of equal scaling in the variation of each input. An infinite number of overall scaling factors can be produced by non-equal scaling of individual inputs, but these are bounded by the range of each scaling factor

and remain controlled by the number of inputs varied and their order of influence. The bounds thus defined are scaling between 0.1^7 and 1.9^7, or 1E-7 to 89.4, corresponding to ranges with factors somewhere between 10 and 10^9.

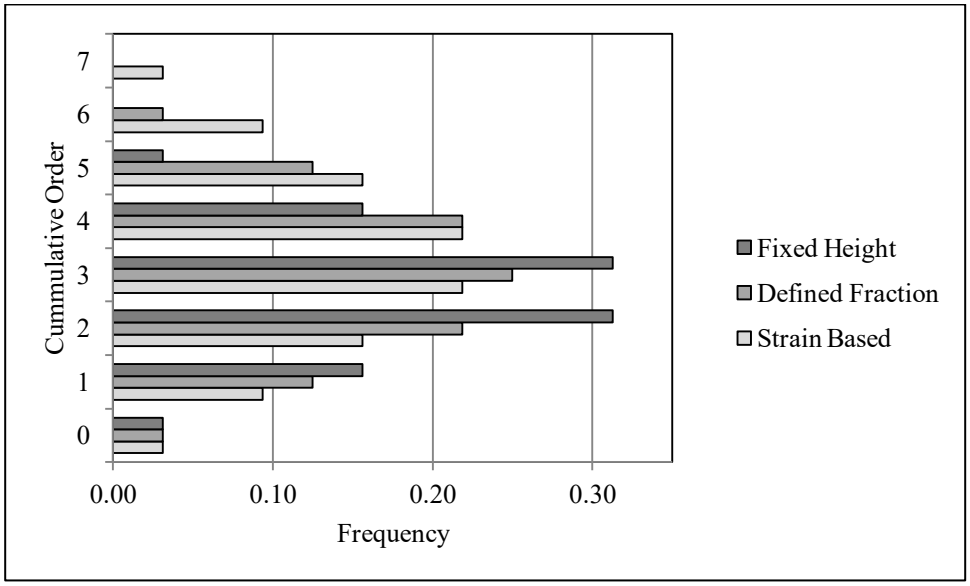

Figure 3.2 – Frequency distribution of cumulative order of influence of input scaling under 3 constitutive cell rupture energy model variants

This represents a wide output variation, but this range can be narrowed by limiting the number of varying inputs to those that are most influential. If cell diameter, failure strain, and one other input are varied, 3 response patterns should be observed based on the 3 combinations of order dependence seen in Table 3.3, with the third varying input acting as a linear scaling factor. Contour plots of the expected patterns observed by varying failure strain and cell diameter under the 3 material volume model variants are shown in Figure 3.3. These contour plots show both symmetric and asymmetric influence scenarios for failure strain and cell diameter. The

energy ranges produced are at the low end of that possible in the bounds identified for the simplified model.

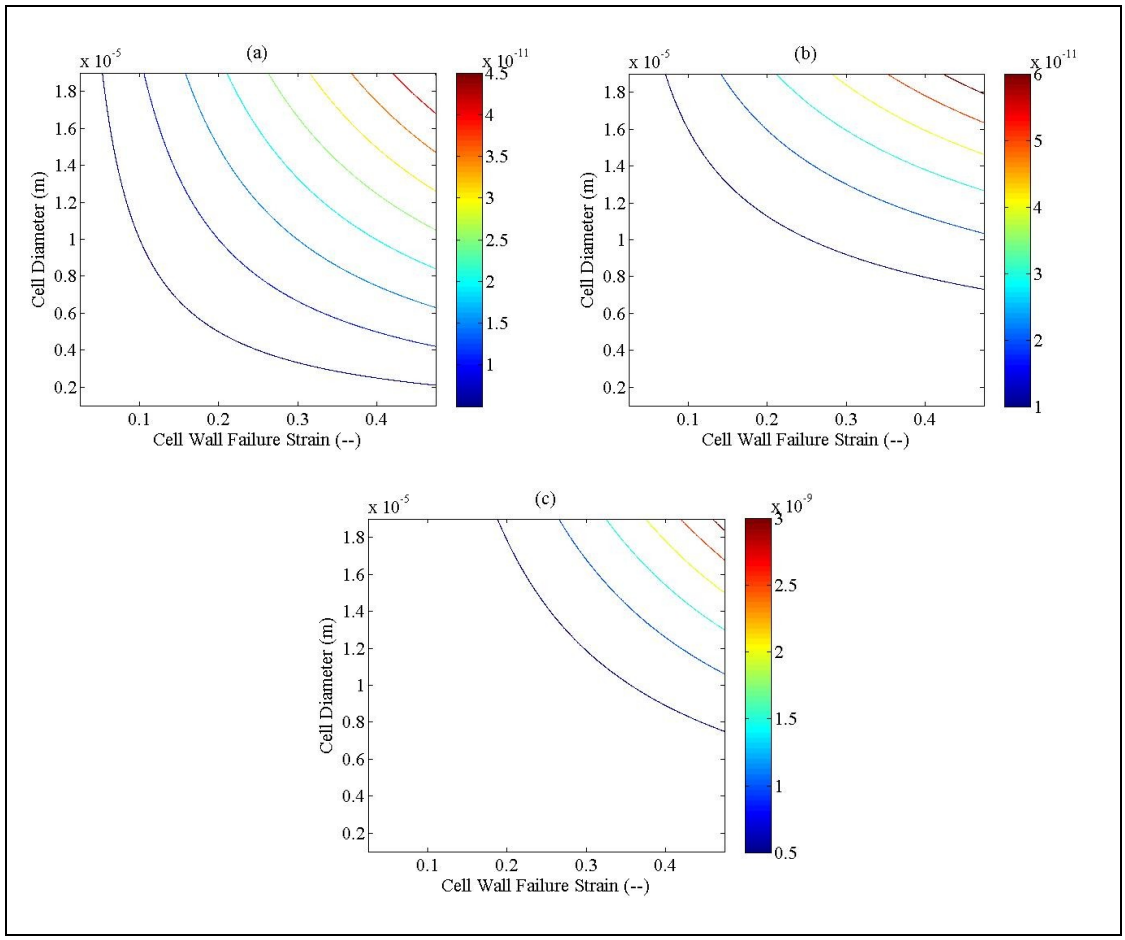

Figure 3.3 – Cell rupture energy (J) output contours of constitutive cell rupture model over input space of cell diameter and failure strain: (a) assumed height model h = 100E-9m, (b) set fraction height model α = 0.01. (c) strain based height model f_s = 0.25

The exploration of the 2D input space is expanded using scatter plots of energy outputs with uniform random variation of all inputs, including those held constant in the line and contour plots. Linear Elastic model scatter plots are representative of scatter shape, and are presented alone in Figures 3.4 – 3.6.

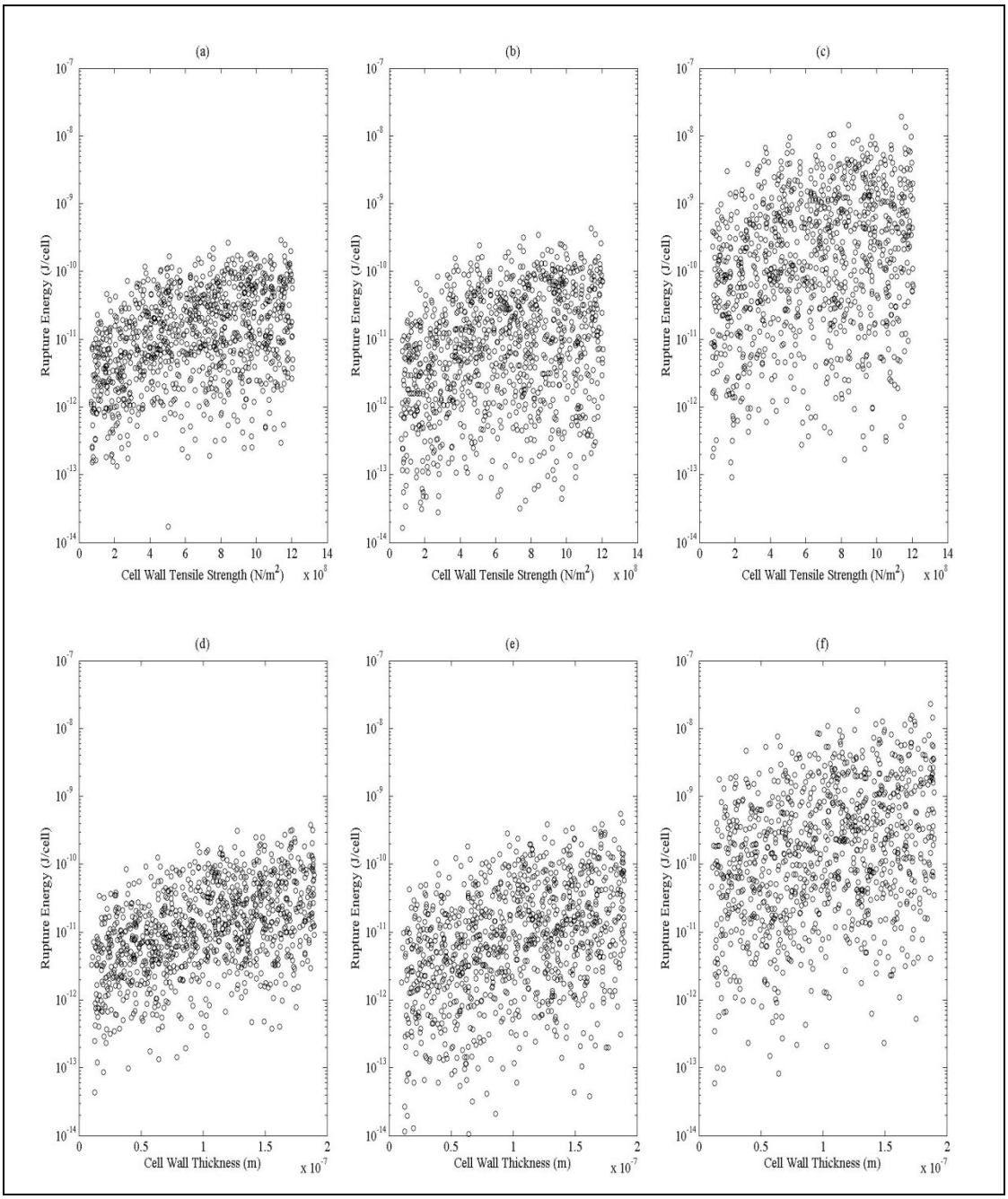

Figure 3.4 – Scatter plots of cell rupture energy versus tensile strength and versus wall thickness for linear elastic constitutive model with uniform random variation of all other inputs: (a and d) assumed height of material at h = 100nm, (b and e) circumference fraction of material at $\alpha = 0.01$, (c and f) strain based fraction of material at $\varepsilon_f = 0.25$

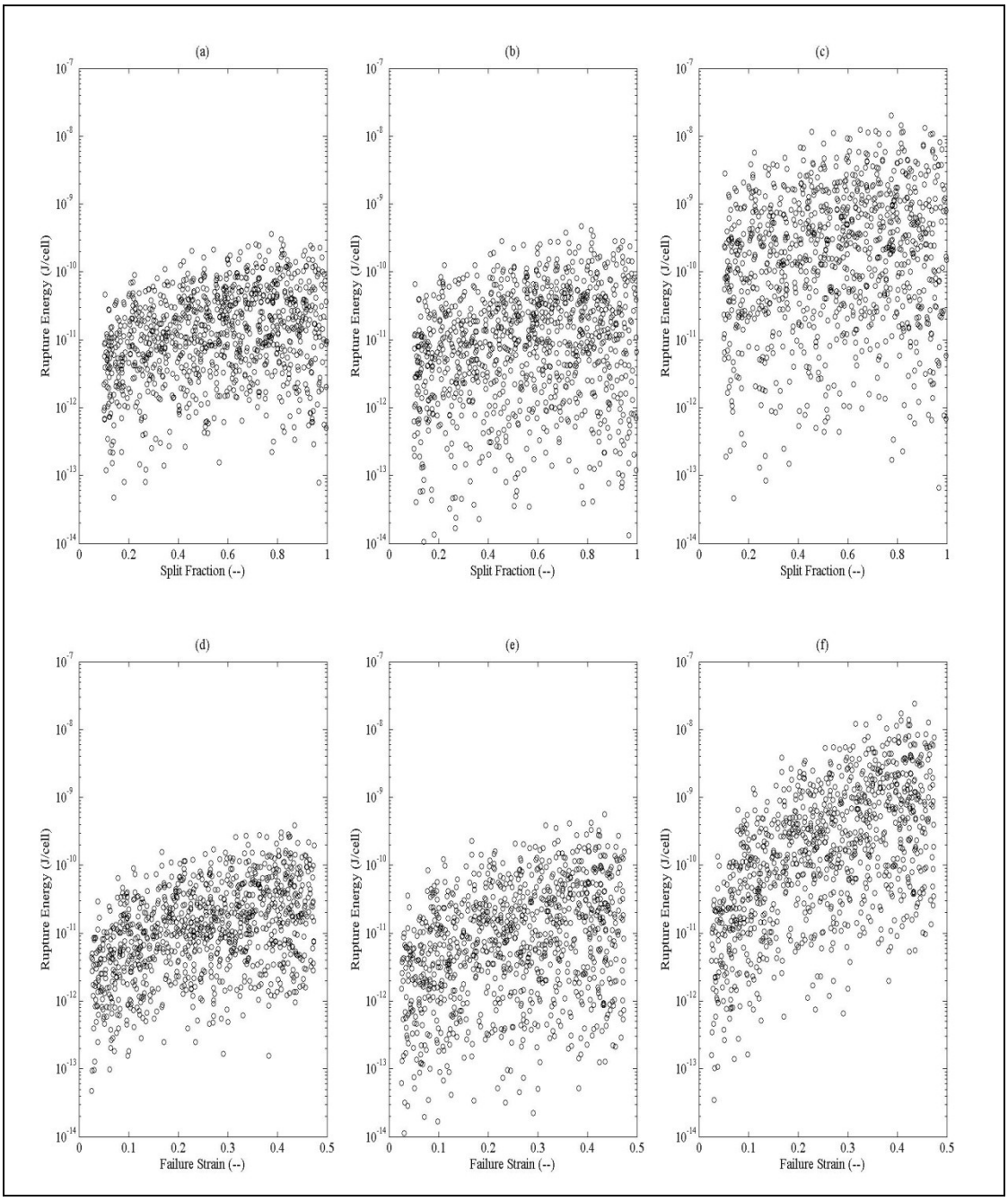

Figure 3.5 – Scatter plots of cell rupture energy versus split fraction and versus failure strain for linear elastic constitutive model with uniform random variation of all other inputs: (a and d) assumed height of material at h = 100nm, (b and e) circumference fraction of material at $\alpha = 0.01$, (c and f) strain based fraction of material at $\varepsilon_f = 0.25$

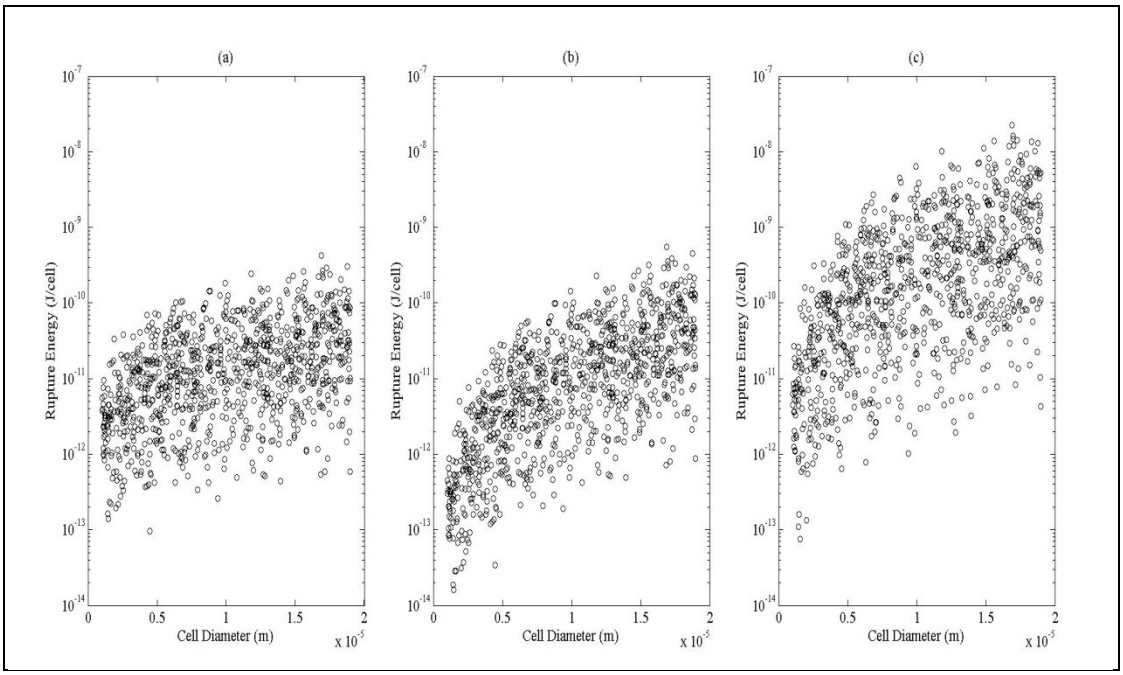

Figure 3.6 – Scatter plot of cell rupture energy versus cell diameter for linear elastic constitutive model with uniform random variation of all other inputs: (a) assumed height of material at h = 100nm, (b) circumference fraction of material at $\alpha = 0.01$, (c) strain based fraction of material at $\varepsilon_f = 0.25$

Both an envelope of rupture energy values and degree of influence are suggested from these scatter plots. All exhibit monotonic increase. However, some also display indications of asymptotic increase rather than the unbounded increase seen in Figure 3.1. The most influential variables are again recognized as cell diameter and failure strain. The ranges of energy values observed also lie within the scaling ranges indicated by the simplified model at 10^4 - 10^7.

3.2.3 Conclusions

A simplified constitutive model of cell rupture energy predicts both first and second order dependencies on the 5 tested inputs. An anticipated variation of ±90% in each input produces potential for energy ranges scaled by 10 – 10^9. OVAT analysis of

the non-simplified constitutive model found that the simplified model orders of dependency on each input match those of the non-simplified model. Variation of only the 2 high influence inputs in the non-simplified model produce range scaling lower than that predicted by the same variation in the simplified model. Random variation of all inputs to the non-simplified model produced energy range scaling from 10^4 - 10^7, a smaller range than predicted by the simplified model. Results indicate that cell diameter and failure strain are the most influential inputs, and that the simplified model should not be used because of a significant and unnecessary loss in precision.

3.3 Cell Diameter Measurement and Monte Carlo Simulations of Cell Strength

Sensitivity analysis of the constitutive model of cell rupture energy both expanded the deterministic prediction of rupture energy to ranges incorporating random variation of model inputs and confirmed the primary importance of cell diameter and failure strain in controlling rupture energy. Model predictions are further refined here by incorporating more realistic statistical variation of input populations and directly measuring the inputs that hold primary importance.

While direct measurement of the primary inputs could decrease uncertainty associated with model predictions of cell failure energy, experimental systems present challenges of measurability. The in-vivo failure strain of a single cell wall is not readily measurable, but the distribution of diameters of cells in a culture can be measured by several established methods.

This section of the study addresses the challenge of improving model prediction accuracy and precision by measuring the distribution of *Chlorella vulgaris* cell diameters and performing Monte Carlo simulations of constitutive cell rupture energy using this improved input data.

3.3.1 Materials and Methods

Chlorella vulgaris was obtained from Carolina Biological. Cultures were grown in medium modified from ATCC Medium: 5 Sporulation Agar [114]. Media

was prepared with the following composition in deionized water: yeast extract (0.333g/L), beef extract (0.333g/L), FeSO4-7H2O (0.00133g/L), dextrose (3.33g/L). Cultures were grown for 30 days under fluorescent light on a 12hr/12hr on/off cycle using active mixing in foam stopped bottles, and then stored at 4^{o}C until analysis.

Cell size was analyzed in 3 triplicate sequences (n=10,000 per run) using an M3 Coulter Counter (Beckman-Coulter, USA), employing the electric sensing zone method [115] with a 50μm aperture. Isoton II diluent was employed to maintain isotonic conditions for all measurement runs, and the system was calibrated using a 5μm L5 standard (Beckman-Coulter).

Monte Carlo Simulation

The MonteCarlo simulation is a sampling based approach to simulation of complex processes. Random samples from the assumed distributions of inputs are fed into the process model equations. Each set of random sample inputs produces a single output. Multiple samplings thus lead to multiple outputs. These outputs are the distribution of outputs under random sampling of the input distributions, and should represent actual output distribution [116].

A central value and standard deviation are assigned to each input with an assumed normal distribution, and used in place of the uniform random distribution utilized in the sensitivity analysis. Standard deviations are arbitrarily chosen as 20% of the mean value. The simulations are performed first with the inputs specified in Table

3.4. Simulations are then repeated with the fitted distribution of measured cell diameter in place of the arbitrarily chosen distribution.

Table 3.4 – Monte Carlo Simulation Input Distribution Descriptors

	Mean	Standard Deviation
Cell Diameter	10E-6 m	2E-6 m
Cell Wall Thickness	100E-9 m	20E-9 m
Tensile Strength	638E6 Pa	128E6 Pa
Failure Strain	0.25	0.05
Fraction of Circumference Split	0.25	0.05

3.3.2 Results and Discussion

Cell Diameter

The measured cell diameter displays a unimodal positive skew distribution with mean 3.96μm, median 3.85μm, standard deviation 0.814μm, skew 0.902, and kurtosis 2.99. A Q-Q test plot for normality (Figure 3.7) shows poor fit of cell diameter to a normal distribution, but a much closer fit to log-normal. This degree of fit is confirmed quantitatively using a correlation coefficient based p-value criteria for assessing fit of a normal distribution [117]. The raw data yield a correlation coefficient of 0.981 and p-value of <0.01, signifying very poor fit. The log-transformed data yield a correlation coefficient of 0.998 and p-value of >0.5, signifying excellent fit. The log transformed cell diameter distribution displays a unimodal relatively symmetric distribution with mean 1.36, median 1.35, standard deviation 0.200, skew 0.157, and kurtosis 0.232.

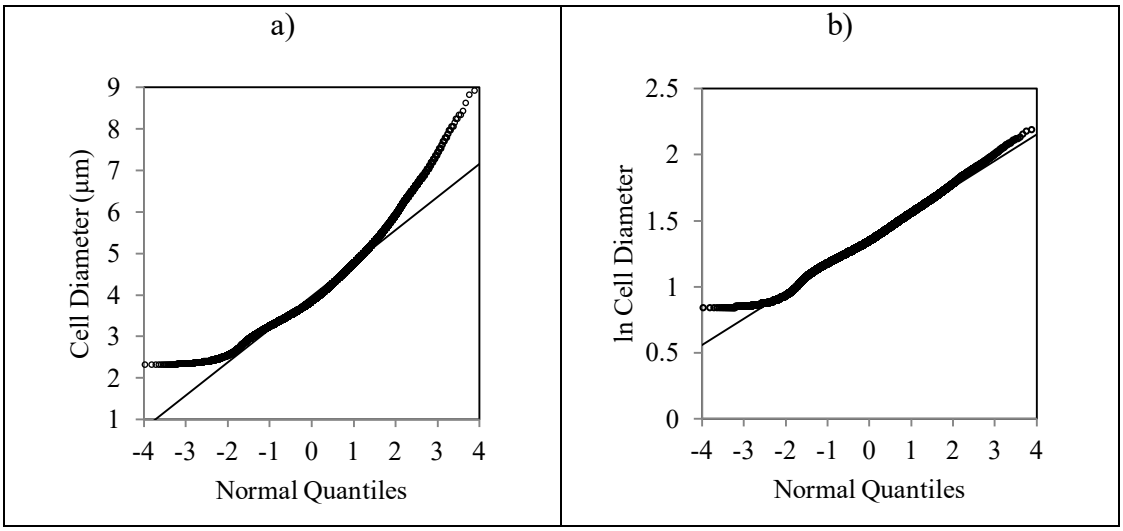

Figure 3.7 – Graphical Q-Q test for normality of a) raw cell diameter distribution and b) log transformed cell diameter distribution

Monte Carlo Simulation

Initial Monte Carlo simulations with all input distributions assumed are presented in Figures 3.8 and 3.9. The scatter plots observed in model sensitivity analysis have been significantly refined, presenting clearly defined envelopes of anticipated cell rupture energies. These envelopes are more clearly interpreted when the Monte Carlo outputs of the full set of 15 model variants are visualized together as a set of cumulative distribution functions (CDFs) (Figure 3.9). While there is horizontal displacement among all CDFs, the forms are relatively consistent. Each shows rupture energies ranging over approximately 1.5 – 2 orders of magnitude, which is much more precise than the 4 – 7 order of magnitude ranges observed in sensitivity analysis. Each also displays a steep ascent with small tails, reflecting the tightly clustered energy values seen in the scatter plots. The 5 rightmost lines in Figure

3.9 (strain based) display the pattern that is observed for the other 2 disrupted volume model variant groups but is obscured slightly by overlap.

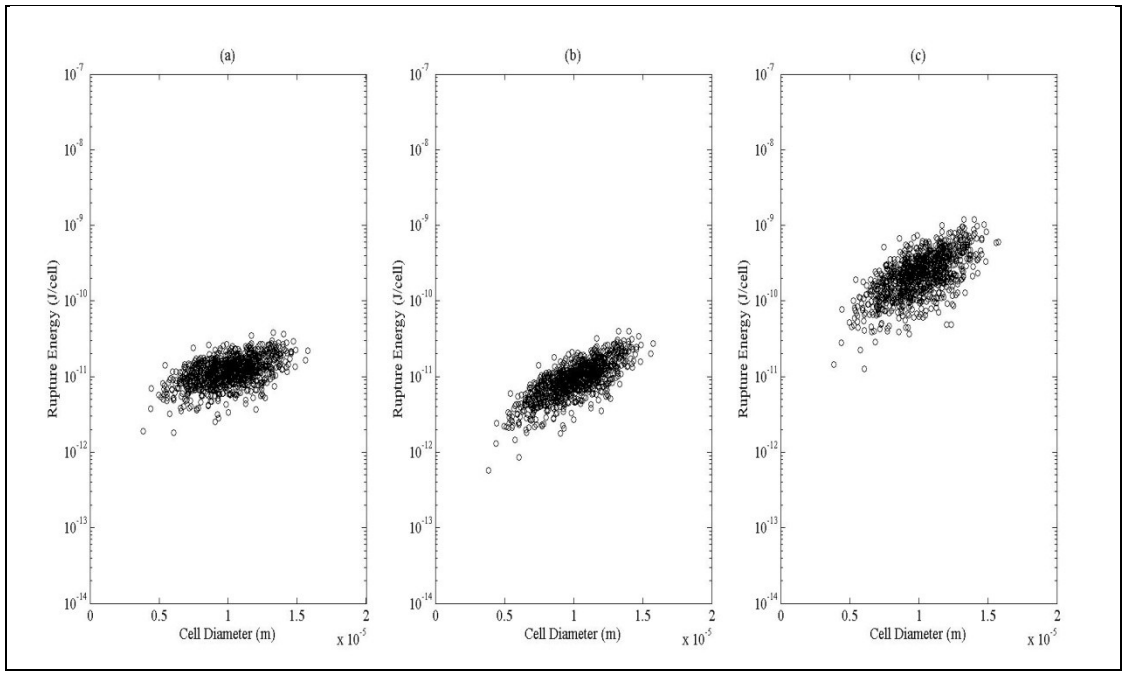

Figure 3.8 – Scatter plots of Monte Carlo simulation outputs for assumed normal distributions of all inputs: (a) assumed height of material at h=100E-9, (b) circumference fraction of material at $\alpha = 0.01$, (c) strain based fraction of material $\varepsilon_f = 0.25$. Cell diameter versus rupture energy plots are presented as representative of observed results

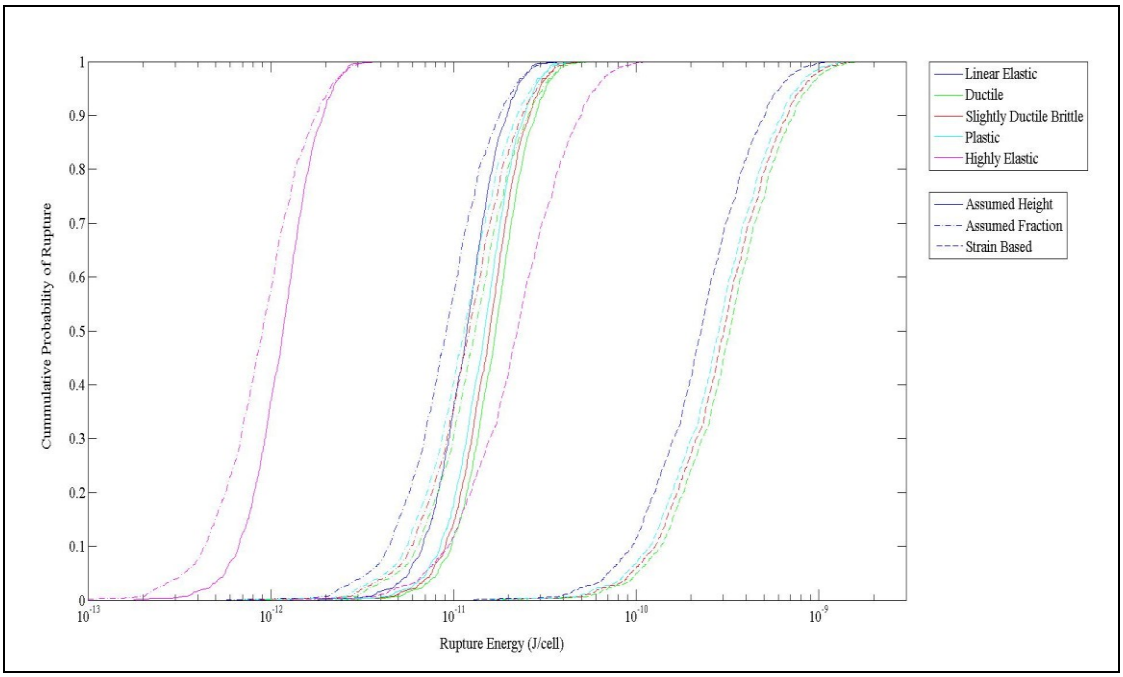

Figure 3.9 – Cumulative distribution functions of cell rupture energy for all Monte Carlo simulation outputs with fully assumed normal input distributions

The measurement based log-normal model distribution of cell diameter is then substituted for the assumed normal distribution, and the Monte Carlo simulations are repeated. Results are shown in Figures 3.10 and 3.11. The CDFs in Figure 3.11 have the same shape and approximate magnitude of range as those in Figure 3.9, but are shifted to the left by different amounts for each of the three model groupings for V_{dm}, resulting in the observed spread of previously overlapping CDFs. This corresponds to the downward shift of the scatter positions from Figure 3.8 to Figure 3.10.

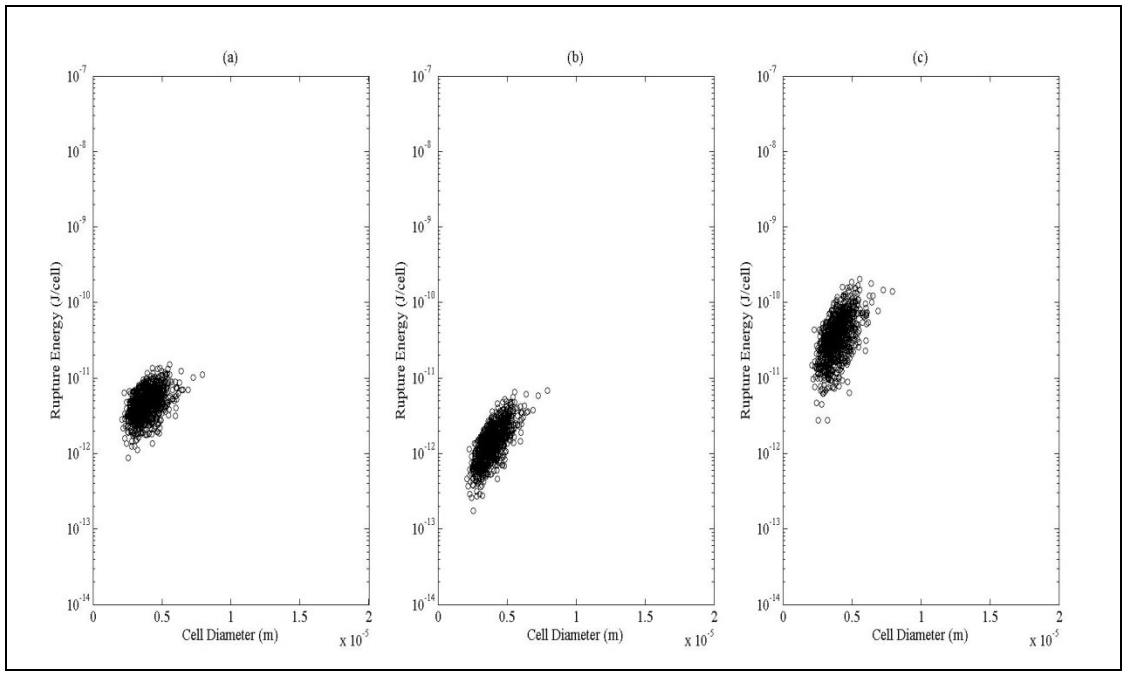

Figure 3.10 – Scatter plots of Monte Carlo simulation outputs for measurement based cell diameter input. Cell diameter versus rupture energy plots are presented as representative of observed results: : (a) assumed height of material at h = 100nm, (b) circumference fraction of material at $\alpha = 0.01$, (c) strain based fraction of material at $\varepsilon_f = 0.25$

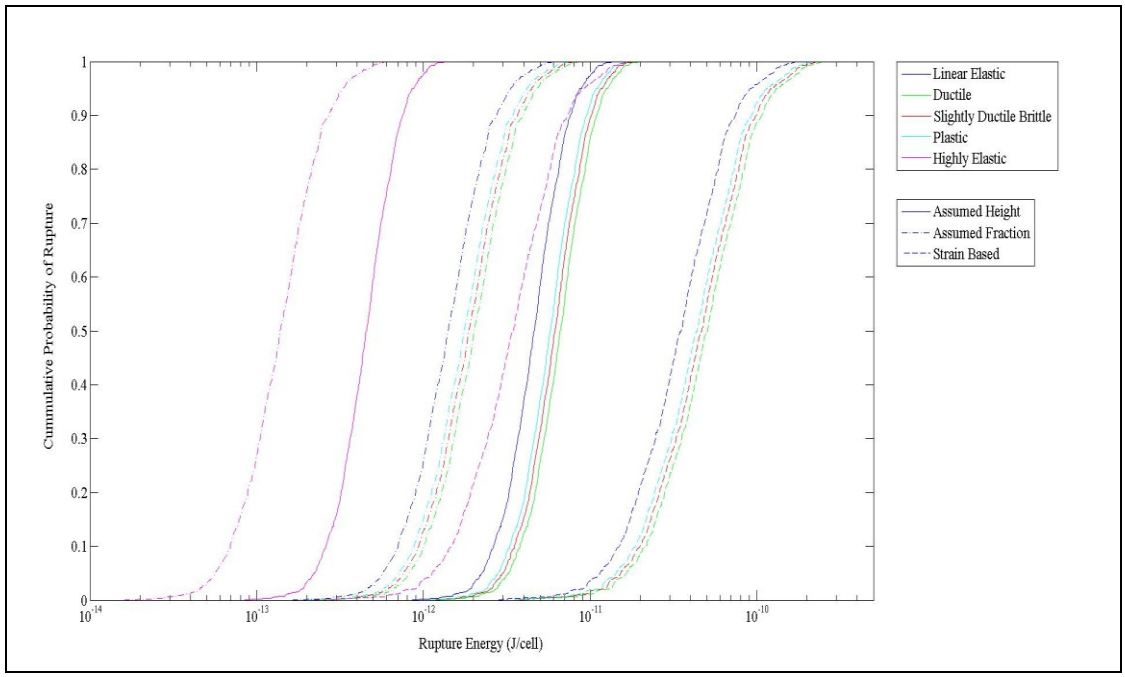

Figure 3.11 – Cumulative distribution functions of cell rupture energy for all Monte Carlo simulation outputs with measurement based cell diameter input distribution

Because of the similar shapes of these distributions and the nature of the pretreatment process, a threshold energy value comparison is appropriate. The natural point of diminishing returns for energy investment toward cell rupture is the inflection point of the CDF around the 50th percentile. However, because of the goal of maximal cell rupture and the narrow CDF shoulders, the 90th percentile is chosen for comparison and assigned the symbol E_{90}. A comparison of E_{90} values for all model variants is presented in Figure 3.12. The measurement based assumed height, assumed fraction, and strain based model variant predictions were scaled down by 60%, 85%, and 84%, respectively, relative to the assumed value predictions. The improved input also had the effect of decreasing the span of E_{90} values across all model variants from 701pJ to 113pJ.

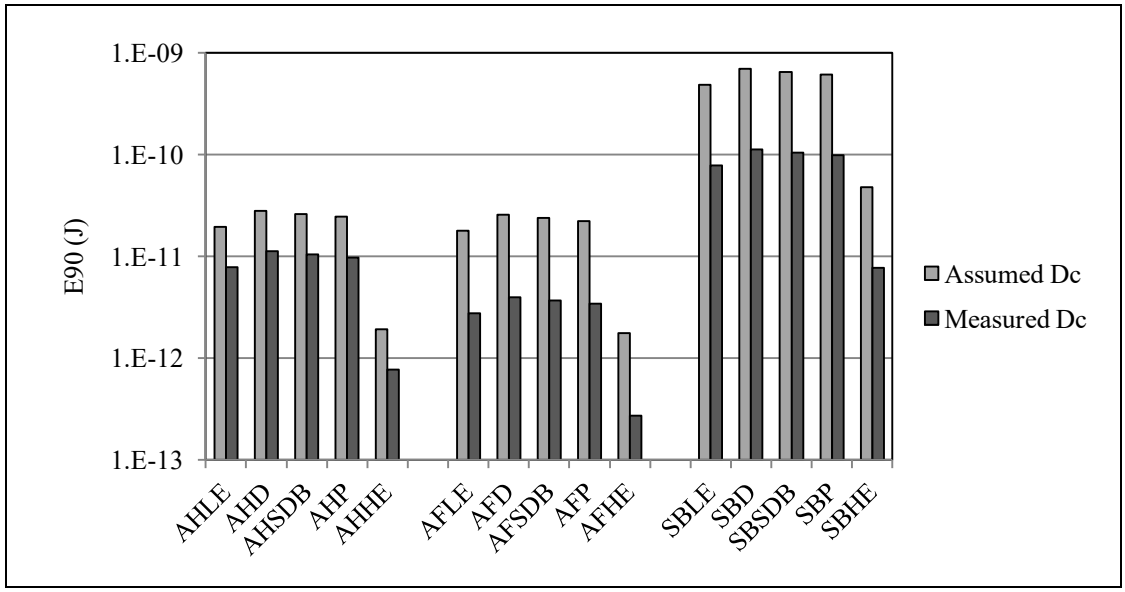

Figure 3.12 – E_{90} values for cell rupture from Monte Carlo simulations. (prefixes: AH = assumed height; AF = assumed fraction; SB = strain based) (suffixes: LE = linear elastic; D = ductile; SDB = slightly ductile brittle; P = plastic; HE = highly elastic)

Values of E_{90} provide limits to test against energy content of the cell for feasibility in terms of net energy. Assuming a single energy level is supplied, the cumulative distribution of energy/cell can be used to predict the energy/cell requirement to rupture a specified fraction of cells in solution. This value can then be conditionally extrapolated to total energy input for a suspension of many cells as has been done in [38]. This can then be conditionally extrapolated further to process/extraction performance improvements given appropriate correlations that will be process specific. Where experiments provide correlation between fractional cell rupture and process performance, the energy to attain that performance change can be predicted based on the constitutive model using appropriate cell information.

Extrapolation of expected energy requirements from E_{90} can be made, but those extrapolations assume a one-to-one matching of single energy treatment interactions with 100% efficiency. Because this is not the case in any pretreatment system, the E_{90} extrapolation can at best be used as a lower bound of expected process energy requirements. Additional insight requires the consideration of the underlying assumptions of interaction frequency, pretreatment energy distribution, and the criticality of interactions in terms of cell rupture.

A set of cumulative distributions of rupture energy was obtained from Monte Carlo simulations. In physical experiments, 100% rupture is not usually a reasonably attainable endpoint. This leads to the use of 50% rupture as a benchmark or a first order empirical model of cumulative rupture as a function of energy input [64, 87]. The empirical model framing makes some sense as the number of cells available to

rupture in a batch reactor will decrease over the course of treatment. However, this black box model neglects the compound structure of the problem. The rupture process is not simply a change in availability of a reactant with uniform properties.

3.3.3 Conclusions

Monte Carlo simulations of constitutive cell rupture energy produced distributions with ranges of approximately 2 orders of magnitude. This is a drastic improvement in precision from the results of sensitivity analysis. Cell diameter was observed to follow a log-normal distribution. Substitution of the measured cell diameter distribution for the assumed distribution in Monte Carlo simulations resulted in a negative shift of the energy distributions, but negligible change in precision for any single model variant. Interpretation of the CDFs of rupture energy in terms of E_{90} revealed that the measurement of cell diameter reduced the spread of modeled rupture energy across the suite of model variants by a factor of approximately 7, a drastic improvement in overall model precision.

Chapter 3, in part, is currently being prepared for submission for publication of the material. Klinger, Rory; Garoma, Temesgen. The dissertation author was the primary investigator and author of this material.

Chapter 4 - **Growth Media Selection and Power Ultrasound Processing**

The effect of microalgae growth medium on power ultrasound treatment of microalgal biomass was investigated. *Chlorella vulgaris* was grown in Bold's Basal Medium, high and low iron Bristol's Medium, Sueoka Medium, HAMGM Medium, and MiracleGro All Purpose Water Soluble Plant Food. High iron Bristol's Medium and HAMGM Medium did not produce sufficient growth to warrant further investigation. The other 4 media showed statistically indistinguishable intrinsic growth rates, averaging 0.052/day. Power ultrasound treatment was applied at 9.5W for 5 minutes. MiracleGro showed chemical oxygen demand solvation post-sonication of 66%, twice that of other growth media per cell ruptured; which was unexpected based on observed consistent biomass quality. Media differences do not appear to have an effect on ultrasound power transfer; thus *Chlorella vulgaris* grown in MiracleGro medium has a decreased strength in terms of resistance to rupture by ultrasound. These results suggest that while biomass productivity and composition are important for the efficiency of extraction, media effects on the susceptibility of cells to pretreatment should not be ignored in overall process design.

4.1 Introduction

Material extraction from microalgae is a technically viable option for the production of many products from food and beauty products to plastics and fuels. However, the technical feasibility of these products has not always translated to financial feasibility. In order to enhance the extraction process, pretreatment of the microalgae biomass is often required [32, 118]. The objective of pretreatment is the rupture of the cell wall and membrane toward the end of increasing availability for reaction of expelled cell contents and newly exposed cell materials [35].

Power ultrasonic treatment has been demonstrated as an effective method of microalgae cell disruption and extraction enhancement [59, 60, 63-65, 67]. However, extraction efficiency is also affected by the composition of the cell biomass, which can be controlled to a certain extent by the growth medium selection [57, 119]. While the individual effects of media on composition [119] and pretreatment on extraction [60] have been investigated, the effect of media on the efficiency of pretreatment is a gap in current knowledge.

By understanding the effect of growth media on pretreatment effectiveness, the relationship between growth medium and pretreatment efficiency may be incorporated into process optimizations for both energy and cost for a given extraction product.

In order to explore this relationship, the objectives of this study are: 1) to identify appropriate growth media based on isolation ability and growth rate, 2) to characterize cultures grown on these media in terms of biomass production and energy conversion potential, and 3) to determine the effect of growth medium on low frequency power ultrasound pretreatment performance.

4.2 Materials and Methods

Growth Media

Growth of feedstock material consistent enough for reproducible laboratory analysis is facilitated by the use of synthetic media. Synthetic freshwater media used to grow *Chlorella vulgaris* include: Sueoka Medium [120], Bold's Basal Medium (BBM) [113] (modified to 1/6 trace metals concentration, Bristol's Medium [121], Bristol's Medium amended with excess ferric chloride [122], and HAMGM Medium [123]. The Bristol's media are designated Bristol's (-Fe) and Bristol's (+Fe), respectively. TAP Medium [124], which is supplemented with organic carbon, was also used to include a minimally enriched medium.

Informal online materials for lab instructors and students [125] recommend MiracleGro All Purpose Water Soluble Plant Food (Material: SH1181) as a simple isolation media for the growth of microalgae in the laboratory, and it has been used in the literature as a nitrogen and phosphorus supplement [126]. Preliminary tests mixing rich media with MiracleGro at varying ratios to encourage growth rate and microalgae dominance in culture led to the determination that the most consistently aseptic and high rate growth came from a basal medium consisting of only MiracleGro solution (2.337 g/L - Hydrated). In order to remain consistent with the literature while exploring this simple alternative media, MiracleGro is run in parallel with the synthetic freshwater media identified above.

Microalgal Growth

Chlorella vulgaris was obtained from Carolina Biological Supply Company (USA). All media were autoclaved in individual growth bottles at 121°C and 16.5psi for 30 minutes. A starter culture was created from an agar plate single colony isolate, and inoculations were performed inside a laminar flow hood using aseptic technique. 150ml cultures were grown in foam stopped 250ml media bottles, magnetically stirred to produce an ~6mm vortex well (~400RPM). Lighting was on a 14h/10h on/off cycle via 2x 40W fluorescent light tubes suspended ~1m above the cultures. The lab temperature regularly fluctuated in the range of 20-25°C. Three growth runs were completed in duplicate for each medium, with the exceptions of Bristol's (+Fe) and MiracleGro. Bristol's (+Fe) produced no growth, and so was abandoned after the first run and replaced with MiracleGro in subsequent runs.

Biomass concentration was monitored by measuring the spectrophotometric absorbance of each culture for 31 days (300nm-800nm) using a BioMate3S spectrophotometer. Spectra were monitored for aberrant peaks that could indicate contamination. In order to minimize the risk of contamination during sampling, the culture bottles were measured directly, and absorbance values corrected to 1cm path length via Lambert's Law using a matched 1cm cuvette reading at the end of growth for each culture bottle.

Culture Analyses

At the end of the growth period, each culture was sampled and its absorbance spectra read (300-800nm) in a 1cm cuvette. Cultures were then analyzed for: chemical oxygen demand (COD), soluble COD (SCOD), total solids (TS), ash free dry weight

(AFDW), cell concentration, % cell viability, electrical conductivity (EC), Oxidation Reduction Potential (ORP), and pH.

COD and SCOD were measured as indicators of total and soluble organic carbon. Samples were analyzed using the dichromate reactor digestion method (HACH method 8000), with the soluble fraction taken as the supernatant after centrifugation at 17,000xg for 5 minutes.

TS was measured as culture mass remaining after drying at 105^{o}C. AFDW, representing the biomass fraction of TS, was measured as the mass lost from the TS sample upon firing at 550^{o}C for 1 hour [127].

Cell concentrations and % viability were determined optically via automated cell counts (Nexcellom Cellometer AutoX4). 20µl of culture sample was combined with 20µl propidium iodide (PI) stain (Cellometer ViaStain™ PI Staining Solution) in a 1.5ml microcentrifuge tube and vortexed for 10 seconds. A 20µl sample was then pipetted to a Cellometer counting chamber and allowed to stabilize for 2 minutes. A bright field cell count was performed, followed by stimulation of the sample at 501nm and emission measurement at 595nm for 10 seconds of exposure. Dead cells were identified via fluorescence of PI, and an automated count of fluorescing cells was executed. Percent viability was then determined as the difference between the bright field and fluorescence cell counts divided by the bright field cell count.

EC was measured to determine relative salinity of the media, an important indicator of media habitability for microalgae. Measurement was performed using a 2-plate epoxy conductivity cell probe (Model 250 Denver Instruments, USA).

Change in ORP is a common indicator of overall oxidation state of chemical species in a solution. As such, it can also be an indicator of succession of microbial communities and redox conditions that can influence microbial growth. Measurement was performed using an Ag/AgCl referenced platinum disc ORP/Redox probe (MTC101 HQ440d Hach, USA).

pH is important to CO_2 availability and the multitude of reactions essential for microalgal growth. Measurements were performed using an Ag/AgCl single junction glass pH probe (PHC101 HQ440d Hach, USA).

Low Frequency Ultrasound Treatment

Low frequency power ultrasound treatment was performed using a sonotrode system (20kHz) with a 1/8in (3.175mm) micro-tip (Q55 Qsonica, USA) immersed 1.5cm in 50ml of sample in a 50ml jacketed beaker with recirculating water at 25.5^{o}C for a sample temperature of 25^{o}C. Treatment was performed at a setting of 100 (8.13W) for 5 minutes. Temperature was monitored to check for overheating (max. 28.4^{o}C). Power transfer to solution was determined calorimetrically [101] in a separate test.

The fixed growth period led to culture samples being treated directly, without dilution. Because of the small culture volume, and the desire to determine the effect of the media as it existed at the end of the growth period, dilution was not practical. While there is a recognized effect of cell concentration on power ultrasound performance, it has been shown to decrease significantly in magnitude with a decrease

in the power of ultrasonic treatment, becoming insignificant at 32.5W [64], well above the power of 8.13W used here.

After power ultrasound treatment, samples were again analyzed for cell concentration, % cell viability, COD, SCOD, EC, ORP, and pH. Because solvents, digestive enzymes, and other extracellular reactants of biomass processing tend to be non-permeant to live cells, cell death is measured as an indication of susceptibility to processing. The fraction of total COD that is soluble is a direct measure of the organic constituents that are most directly accessible to physical separation, chemical reaction, and microbiological transformation [128]. EC, ORP, and pH can be influenced by the release of intracellular molecules, and thus may be indicators of: the release of intracellular contents, solution characteristics that may influence downstream processes, and suitability of treated media for recirculation after biomass dewatering.

Statistical Methods

Three types of statistical analyses were used. In group, pre-post comparisons were analyzed using a one tailed paired t-test. Significant difference of values among groups was identified using one-way ANOVA. Significant differences of values in pair-wise multiple-comparisons between groups were identified and quantified using Fisher's protected LSD. A significance criteria of $\alpha=0.05$ was used for all analyses. p-values are presented for t-test and ANOVA results, but not for Fisher's LSD where it could be misleading and thus is not conventionally done [129].

4.3 Results and Discussion

Media Selection

Growth rates are calculated as intrinsic (exponential) growth rate from the change in absorbance at 750nm [130]. Optical density is a common surrogate for cell count in microalgal growth. The absorbance spectra of sample dilutions were analyzed at each wavelength (300-800nm; 2nm spacing) for linearity of correlation with cell count. Linear regression R^2 of 0.9975 and 0.9992 for 600nm and 750nm, respectively, confirm the appropriateness of these wavelengths. However, absorbance at 750nm avoids interference by changing pigment absorption over the microalgae life cycle [131]. A sample absorbance spectrum is presented as Figure 4.1.

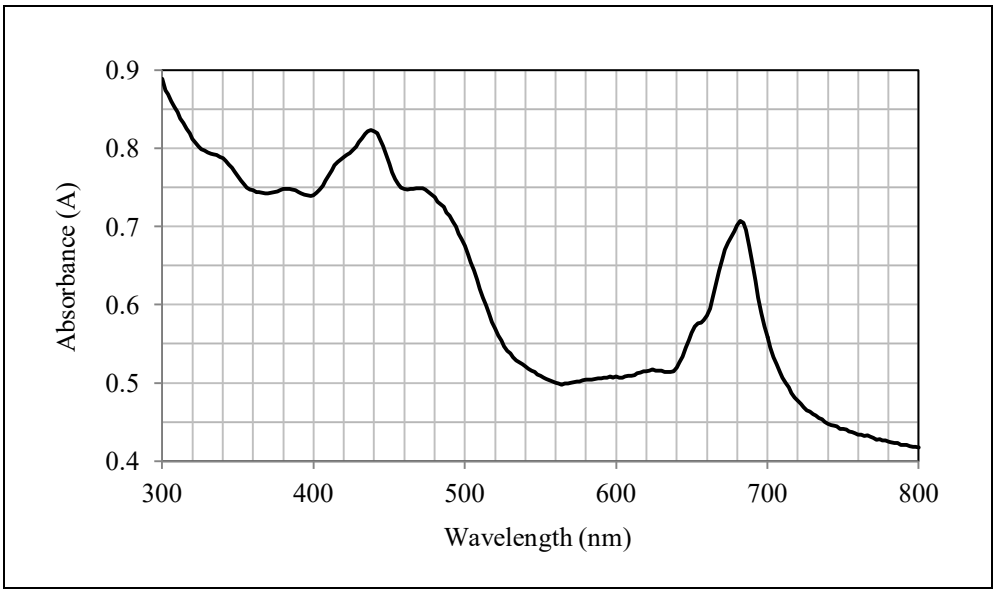

Figure 4.1 – Sample spectrophotometric absorbance spectrum of *Chlorella vulgaris* grown in BBM medium

Because Bristol's (+Fe) did not produce any growth, it is excluded from all analyses. TAP medium consistently produced considerable growth, but is excluded from growth rate and other analyses because of a contamination frequency of 1. While HAMGM medium produced viable growth, consistent formation of precipitates and floc confounded optical density measurements and was inconsistent with growth in the other media. For these reasons, HAMGM is also excluded from further analyses.

The highest growth rate of *Chlorella vulgaris* was obtained in BBM medium, followed by Sueoka, Bristol's (-Fe), and MiracleGro medium (Figure 4.2). Results of one-way ANOVA show no significant difference of intrinsic growth rate among the growth media (p=0.238). Follow-up multiple comparison using Fisher's Protected LSD confirms this result.

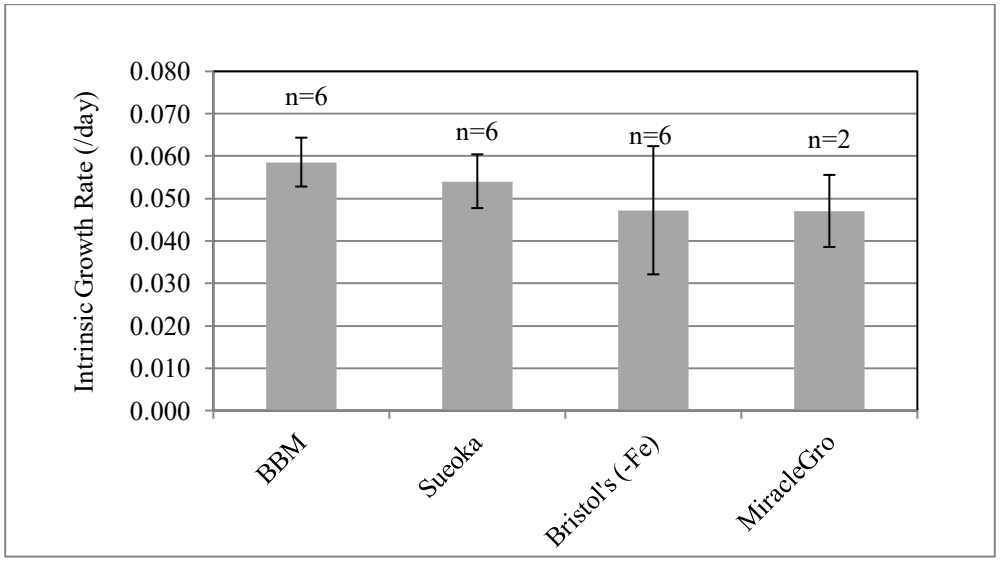

Figure 4.2 – Intrinsic growth rates (r) of *Chlorella vulgaris* grown in specified media. Sample size is indicated by n, defined as the number of cultures that reached an observable maximum growth rate within 31 days without crash due to contamination. Error bars are one standard deviation

Because pond crash prevention is such a critical aspect of successful commercial microalgae cultivation, the tendency of laboratory cultures to maintain algae dominance is important to consider. While strict biological procedures would require the maintenance of axenic cultures, non-axenic cultures are a reality of commercial microalgae production and results are presented here in that context. This tendency toward algae dominance in culture is presented here as isolation ability, calculated as one minus the frequency of contamination; 1-n(contaminated)/n(total). When considering viability of growth overall, a combined frequency of contamination and non-growing cultures, $F_{c,ng}$, can be used; 1 - (n(contaminated) + n(non-growth)) / n(total). Of the six cultures inoculated in each medium, with the exception of MiracleGro with 4 cultures, only N_p algae dominant culture growths were observed. The growth rate, contamination, and non-growth data are summarized in Table 4.1 and the media ranked according to both intrinsic growth rate and frequency of non-viable cultures. BBM and Sueoka are identified as the best media for growth rate. Bristol's (-Fe) and Sueoka are identified as the best media for isolation and viability of growth. The success of growth in these cultures is not surprising given that they are standard media used in laboratory microalgae cultivation. Interestingly, MiracleGro matches Bristol's (-Fe) in terms of growth rate, and performs reasonably well in terms of isolation and viability of growth, though not nearly as well as the synthetic freshwater media Bristol's (-Fe), Sueoka, and BBM.

Table 4.1 – Intrinsic growth rates and frequency of contamination and non-growth of *Chlorella vulgaris* in specified media. The mean intrinsic growth rate (r) is presented ± one standard deviation. $F_{c,ng}$ is the combined frequency of contamination and non-growth. N_p is the number of algae dominant culture growths

	BBM	Sueoka	Bristol's (-Fe)	MiracleGro	HAMGM	TAP
r	0.059 ±0.006	0.054 ±0.006	0.047 ±0.015	0.047 ±0.008	NA	NA
$F_{c,ng}$	0.167	0.000	0.000	0.500	0.667	1.000
N_p	5	6	6	2	2	0
Rank(r, $F_{c,ng}$)	(1,3)	(2,1)	(3,1)	(3,4)	(- ,5)	(- ,6)

Biomass Production and Energy Conversion Potential

While intrinsic growth rate (r) determined from batch growth curves is sufficient to rank the media in terms of biomass productivity for a commercial semi-continuous culture harvested in the logarithmic phase, the utility of that biomass is not considered. In order to incorporate utility, a substrate yield would normally be considered. However, to broadly represent the yield of energy conversion potential, a generalized substrate should be considered. Here, biomass is represented by TS, generalized bio-methane potential is represented by AFDW, and generalized energy conversion potential is represented by COD. Thus the biomass yield is taken as AFDW/TS and the energy conversion potential is COD/TS (Table 4.2). These relationships are commonly used in anaerobic digestion operations. The system response to AFDW and COD loading is generally characterized under a given set of operating conditions to produce a conversion factor in units of $gCH_4/gCOD$ [132]. An analogous performance correlation using SCOD of microalgae solutions after pre-treatment has also been presented in the literature [83].

Table 4.2 – Growth Rate, Biomass Yield, and Energy Conversion Potential of *Chlorella vulgaris* in specified media. Values are mean ± one standard deviation

	BBM	Sueoka	Bristol's (-Fe)	MiracleGro
r	0.059 ±0.006	0.054 ±0.006	0.047 ±0.015	0.047 ±0.008
AFDW/TS	0.467 ±0.021	0.347 ±0.159	0.433 ±0.107	0.464 ±0.051
COD/TS	0.409 ±0.084	0.292 ±0.189	0.337 ±0.202	0.244 ±0.037

Results of one-way ANOVA for AFDW/TS and COD/TS show no significant difference between the different media cultures. The relative consistency of these measures between cultures grown in each of these media suggests that intrinsic growth rate should remain the prominent selecting factor among these options for *Chlorella vulgaris* growth media.

Growth Medium Effect on Power Ultrasound Pretreatment Performance

Pretreatment performance was measured as cell death and dissolution of cell materials. Cell death is presented as the change in percent cell viability (Figure 4.3). Dissolution is calculated as the change in soluble fraction of COD (Figure 4.4).

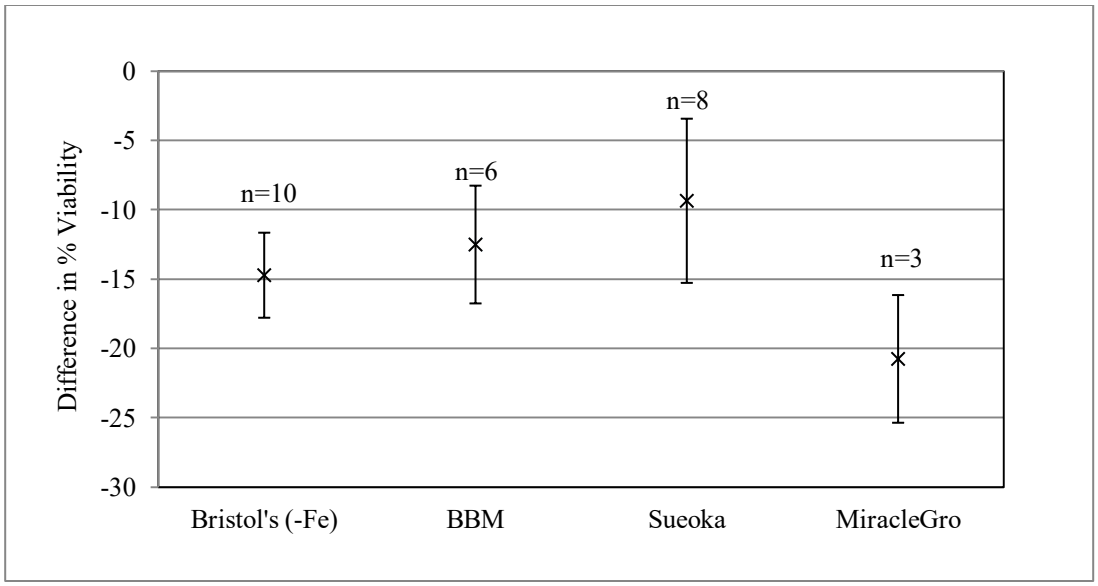

Figure 4.3 – Power ultrasound effect on % viability of *Chlorella vulgaris* grown in specified media. Change in *Chlorella vulgaris* % cell viability as PI fluorescence after power ultrasound treatment. Error bars are one standard deviation. Minimum viability of cultures prior to treatment was 98.2%

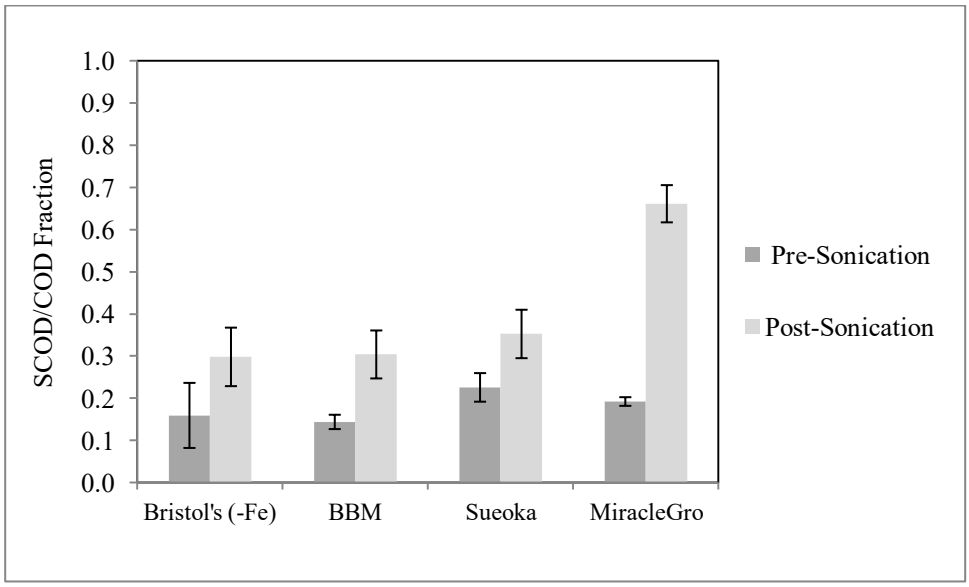

Figure 4.4 – Solvation of *Chlorella vulgaris* COD in specified media by power ultrasound. Soluble fraction of COD before and after power ultrasound treatment of 50ml volume. Error bars are one standard deviation

It appears from Figure 4.3 that MiracleGro culture cells were more susceptible to death by sonication, with the other media being approximately equivalent. Analysis of the data presented in Figure 4.3 using one-way ANOVA reveal a significant difference ($p=7x10^{-3}$) among growth media in the effect of sonication on cell viability. Multiple-comparison using Fisher's protected LSD gives overlapping but non-combining ranges of significant differences, grouping Sueoka with BBM , BBM with Bristol's (-Fe), and Bristol's (-Fe) with MiracleGro. Differences in effect between media are presented in Table 4.3.

Table 4.3 – Paired differences of change in % viability of *Chlorella vulgaris* after power ultrasound between growth media. Read table as 'column' shows 'value' higher change in % viability than 'row'. Values are the mean difference ± Fisher's LSD 95% confidence intervals

	BBM	Sueoka	MiracleGro
Bristol's (-Fe)	2.21 ±5.55	5.37 ±5.10	6.04 ±7.08
BBM	--	3.15 ±5.81	8.25 ±7.61
Sueoka	--	--	11.40 ±7.28

The increased sensitivity of MiracleGro cultures extends to solvation of cell contents as COD, but in more dramatic fashion. The effect of power ultrasound treatment on SCOD/COD was shown to be significant for each growth medium via one-tailed paired t-test (Bristol's (-Fe) $p=5x10^{-5}$; BBM $p=2x10^{-4}$; Sueoka $p=1x10^{-6}$; MiracleGro $p=1x10^{-3}$). The change in SCOD/COD between growth media was also shown to be significantly different by one-way ANOVA ($p=4\ x10^{-9}$). Multiple-comparison using Fisher's protected LSD confirms what can be seen in Figure 4; that MiracleGro cultures released COD at a significantly higher level than other growth

media, and there is not a significant difference amongst the other media. The significant differences in treatment effect between media are presented in Table 4.4.

Table 4.4 – Significant differences between media in COD solvation by power ultrasound. Values are mean difference ± Fisher's LSD 95% confidence interval

Media Pairing	Difference in SCOD/COD
MiracleGro - Bristol's (-Fe)	0.330 ±0.079
MiracleGro - BBM	0.309 ±0.085
MiracleGro - Sueoka	0.342 ±0.082

Potential Explanations of the Observed Medium-Pretreatment Relationship

From the results above, a relationship was detected between the medium in which *Chlorella vulgaris* is grown and the change of soluble COD fraction after power ultrasound treatment. However, the question remains whether the relative increases of SCOD/COD are due to differences in: proportion of intracellular SCOD material, power ultrasound mechanical performance, susceptibility to rupture, or a combination of factors.

The continuity of composition observed in Table 4.2 and the high likelihood of complete digestion of unicellular organisms in a COD reaction speak against the possibility of differences in intracellular SCOD material among growth media.

Power ultrasound mechanical performance is affected by a number of factors, with solvent vapor pressure and solution viscosity being most relevant here [101, 133]. Temperature changes were uniform for all treatments. Solvent vapor pressure is very important in ultrasound cavitation. Based on Raoult's Law ($P_{v,solution}=x_{solvent} * P_{v,solvent}$; where x is the mole fraction and P_v is vapor pressure) the vapor pressure of the solvent

will decrease as more constituents are added to solution. Decreased vapor pressure leads to an increase in the amount of energy required to volatilize in a cavitation bubble. Thus the relative energy requirements for cavitation in each of the growth media can be determined based on their composition. An end of growth surrogate for this is the EC, as it is an indicator of ion concentration. As can be seen in Table 4.5, the ascending order of EC of sonicated solutions is Bristol's (-Fe) < BBM < MiracleGro < Sueoka (EC values did not appreciably change due to sonication). This order does not match what would be expected if the ion concentration effect on vapor pressure were a controlling factor in sonotrode performance (i.e. MiracleGro < Bristol's (-Fe) < BBM < Sueoka).

Table 4.5 – *Chlorella vulgaris* culture end conditions. pH, EC, and ORP of Chlorella vulgaris cultures at the end of 31 days growth in selected media. Values are mean ± one standard deviation

	Bristol's (-Fe)	BBM	Sueoka	MiracleGro
pH	7.18 ±0.18	8.59 ±0.51	6.98 ±0.02	7.88 ±0.13
EC (µS/cm)	741.3 ±164	929.6 ±193	1558 ±75	1150 ±85
ORP (mV)	266.0 ±5.0	239.4 ±16.8	286.3 ±12.3	241.3 ±3.5

Another solution property that strongly affects ultrasound power transfer and cavitation is viscosity. In fact, viscosity is the only damping term in the Rayleigh–Plesset model of acoustically driven bubble oscillation [105, 106]. The relationship between dissolved salts and viscosity is generally that an increase in dissolved salts will increase viscosity. This would suggest that more saline solutions would have more damped cavitation bubble oscillations. Decreased oscillation amplitude might suggest decreased bubble instability and thus decreased bubble collapse. If this is the

case, then the order of ranked values of EC also does not match what would be expected if the ion concentration effect on viscosity were a controlling factor in sonotrode performance.

Thus it is concluded that there is a difference in the resistance to cell rupture of MiracleGro grown Chlorella vulgaris cells in response to 20kHz power ultrasound treatment at 8.13W.

4.4 Conclusions

BBM represents the best medium for rate of *Chlorella vulgaris* biomass production. MiracleGro showed the highest rate of solvation of COD. The amount of solvation was also proportionally higher than in other media on a per cell rupture basis, which was unexpected based on observed consistent biomass quality among growth media. Media differences do not appear to have an effect on ultrasound power transfer, and thus *Chlorella vulgaris* grown in MiracleGro medium has a decreased strength in terms of resistance to rupture by ultrasound. These results suggest that while biomass productivity and composition are important for the efficiency of extraction, media effects on the susceptibility of cells to pretreatment should not be ignored in overall process design. Future work will address this balance of productivity and susceptibility to rupture in terms of relative induced extraction potential per cell mass and biomass composition.

Chapter 4, in full, has been accepted for publication of the material as it will appear in Proceedings of ECOS 2017 - 30th International Conference on Efficiency, Cost, Optimization, Simulation and Environmental Impact of Energy Systems, 2017. Klinger, Rory; Garoma, Temesgen. The dissertation author was the primary investigator and author of this material.

Chapter 5 - **Theoretical Kinetics and Mechanism of Cell Disruption**

A theoretical development of the kinetics and mechanism of microbial cell disruption via ultrasound horn induced cavitation is presented. The general assumption of complete mixing in small to moderate size test systems is challenged and corrected using a mass balance on a 2 concentric reactor model system with 100% recycle. A first order elementary reaction model is employed and then binned to component parallel reactions based on a probability density function (PDF) of cell strength. Consideration of the likely existence of a PDF of cavitation energy leads to the expansion of the parallel cell disruption reactions to a second order elementary reaction model. An assumption of steady state cavitation generation and interpretation of the cell strength and cavitation energy PDFs through the lens of activation energy allows the creation of a first order rate equation for this second order process. An experimental approach for the determination of binned cell disruption rate constants is proposed. An alternative reaction mechanism based on mechanical shear is then developed using the concept of critical distance. The critical distance model is then expanded by incorporating the failure limits of the cell wall material under a constitutive model perspective to derive an expression for the first order rate constant as an explicit function of the operational parameters of microbial cell disruption under ultrasound induced cavitation. A known rate constant value for specific experimental

conditions is then used in conjunction with the critical distance and concentric reactor models to predict the cavitation rate under a sonotrode. The critical distance mechanical shear model is used to prove the existence of a critical distance for any bubble-cell interaction, and the model is then expanded to incorporate the use of PDF inputs for cell and cavitation radii.

5.1 Introduction

Direct laboratory tests of kinetics [64] and quantitative and qualitative process performance indicators [65, 67, 110] are common approaches to the measurement and modeling of cell disruption processes. Direct tests provide useful data characterizing specific systems, but have not been conducted or analyzed in a mathematically generalized framework that can be used to predict the performance of alternative systems.

Power ultrasound treatment of unicellular microbial biomass is one category of specific systems in which such a framework is possible. The species and concentration of biomass [64, 110], geometry and volume of reactor [98], ultrasound probe specifications and placement [98] are generally cited as having quantitatively unpredictable impacts on system performance. Knowledge of microbial cell strength is an important key to the prediction of the minimum energy required to disrupt a population of cells for the purpose of commodity extraction [38]. However, this benchmark is usually foregone in practice. This has resulted in an expansive literature full of narrowly defined systems and performance specifications that are not useful for

drawing general conclusions or predicting cell rupture performance in an alternative system [134].

The interaction of power ultrasound with a solution has been conceptually described as taking place within a discrete reaction zone localized in front of the active face of the ultrasound probe tip [135]. The reaction constants of the overall reactor have been presented in the literature [64, 78, 89, 136]. However, in order to quantitatively predict the elementary reaction kinetics for use in reactor design two models are required: one of the reactor and another of the reaction taking place within the reaction zone. The separation of these models is required in order to isolate the reaction itself, and eliminate the reactor dependent nature of rate constants as they are generally presented in the literature.

To improve understanding of the reaction mechanism, move toward a theoretical system optimization, and provide a framework for quantitative prediction of reactor independent cell disruption rate constants under power ultrasound, this study develops a probabilistic kinetic model of cell rupture and couples it to an isolated reaction zone reactor model.

5.2 Reactor Model

A sonotrode tip placed in the center of a cylindrical batch reactor with rounded edges generates an approximately toroid circulation via acoustic streaming. The reaction zone is below the sonotrode face, and the remainder of the reactor is treated as a storage reservoir with 100% recycle. Mass balances of this recycling 2 reactor

system form a first order linear system of ODEs with constant coefficients, where the reaction zone is assigned the subscript 1.

$$V_1 \frac{dN_1}{dt} = N_2 Q - N_1 Q + V_1 r_1$$

$$V_2 \frac{dN_2}{dt} = N_1 Q - N_2 Q$$

The reaction term (r) is assumed to follow first order decay ($r = -k_1 N_1$), matching the form observed in the overall reactor. With this assumption in place, the system is easily solved by elimination to give a second order linear ODE.

$$\left(\frac{V_1 V_2}{Q}\right) N_2'' + \left(V_1 + V_2 + \frac{k_1 V_1 V_2}{Q}\right) N_2' - (k_1 V_1) N_2 = 0$$

Since measurements of concentration can only be taken in reaction zone 2, and this concentration is known to follow an apparent first order decay, the first order solution with $N_2(0)=N_0$ is substituted for N_2 and it's derivatives: $N_2 = N_0 e^{-kt}$; $N_2' = -kN_0 e^{-kt}$; $N_2'' = k^2 N_0 e^{-kt}$. This is solved for the zone 1 rate constant in terms of the apparent rate constant from zone 2 sampling. Note that as V_2 approaches zero, k_1 approaches k, denoting a CMBR testing scenario.

$$k_1 = \frac{Q\left(1 + \frac{V_2}{V_1}\right) k - V_2 k^2}{Q - V_2 k}$$

5.3 Elementary Reaction Model

The observed bulk cell rupture rate by ultrasound is well described by a first order elementary reaction model ($r = -kN$) [64]. In typical chemical reactions, k is independent of N, but dependent on temperature. In power ultrasound, k is reported as dependent on initial concentration, total power, power intensity, specific power, frequency, reactor geometry, probe geometry, solvent, and temperature. These observed dependencies of k direct this discussion of the reaction model.

The dependence of k on initial concentration implies that the elementary first order model may not be appropriate. While drastic changes in cell concentration can impact viscosity [137] and thus both cavitation and mixing, this should be used to define operational limits of a reactor system rather than impacting the reaction kinetics.

The dependence of k on power intensity (W/m^2) makes sense as a normalization of the thermal analog of power from different sources, but should really be captured in a change of the reaction zone affiliated with the increased surface area of the probe. Equal intensities could imply equal reaction zone volumes since a larger surface area probe must match the intensity of that of a smaller probe by having a shorter longitudinal displacement amplitude. However, the relationship between amplitude and intensity is likely non-linear given that both the active volume through which the probe passes and the amplitude of pressure fluctuations (due to increased velocity) will increase if the frequency is held constant.

Dependence of k on specific power (W/m^3) is reactor dependent, and thus inappropriate for consideration in the reaction model.

Dependence of k on ultrasound frequency is appropriate, as frequency drives the resonant sizes and thus collapse energies of cavitation bubbles. These bubbles will be characterized as a reactant in the reaction mechanism and thus separated from k here.

Dependence of k on reactor geometry is not appropriate for exploration here, as it is a matter for reactor design rather than investigation of the elementary reaction.

The ultrasound probe geometry and design are a matter for a study of cavitation generation and mixing in conjunction with reactor design, not the fundamental reaction process. Solvent selection and temperature effects are also influencers of cavitation generation, not the fundamental reaction process for an assumed rate and distribution of cavitation.

The elementary reaction assumed by the first order empirical model is:

$$Cells_{whole} \xrightarrow{P_{ultrasound}} Cells_{ruptured}$$

To expand this reaction model, cavitation bubbles are treated as discrete reactants rather than an intensive property of the solution (an initially appropriate assumption given that ultrasound power is routinely measured calorimetrically):

$$Solvent \xrightarrow{P_{ultrasound}} Cavitation\ Bubbles$$

$$Cavitation\ Bubbles + Cells_{whole} \longrightarrow Cells_{ruptured}$$

The reaction activity of whole cells (C_w) can be described using number per volume concentration (N_c) as in the first order rate model, and the activity of cavitation bubbles (B) can be described similarly (N_B). However, the cells have a distribution of strengths (f_{cs}) (an analog to activation energy of rupture), suggesting a reaction series based on the discretization of f_{cs}.

Reaction series	Rate equations
$B + C_{1,w} \overset{k_1}{\rightarrow} C_{1,r}$	$\frac{dN_{c,1,w}}{dt} = k_1 N_{c,1,w}$
$B + C_{2,w} \overset{k_2}{\rightarrow} C_{2,r}$	$\frac{dN_{c,2,w}}{dt} = k_2 N_{c,2,w}$
$\vdots$	$\vdots$
$B + C_{n,w} \overset{k_n}{\rightarrow} C_{n,r}$	$\frac{dN_{c,n,w}}{dt} = k_n N_{c,n,w}$

Where $N_c = \sum_i N_{c,i,w}$ in a common volume, $\frac{dN_c}{dt} = \sum_i \frac{d}{dt} N_{c,i,w} = \sum_i k_i N_{c,i,w}$. While the overall rate may be 1st order, that of component reactions may not be. These reactions are considered to run independently and in parallel with no deterioration of N_B, and it is also reasonable to assume that the cavitation bubble collapse energy (bce) in a dynamic environment exists as a distribution (f_{bce}) rather than a single value. The distribution f_{bce} and N_B are used to specify an effective $N_{B,i}$ for each reaction in the series based on the bce required to rupture cells in a specified range. The rate equations for this second order elementary reaction series with parsed bubble concentration is:

Reaction series	Rate equations
$B_1 + C_{1,w} \overset{k_1}{\rightarrow} C_{1,r}$	$\frac{dN_{c,1,w}}{dt} = k_1 N_{c,1,w} N_{B,1}$
$B_2 + C_{2,w} \overset{k_2}{\rightarrow} C_{2,r}$	$\frac{dN_{c,2,w}}{dt} = k_2 N_{c,2,w} N_{B,2}$
$\vdots$	$\vdots$
$B_n + C_{n,w} \overset{k_n}{\rightarrow} C_{n,r}$	$\frac{dN_{c,n,w}}{dt} = k_n N_{c,n,w} N_{B,n}$

With constant N_B, and effective $N_{B,i} = N_B\left(1 - F_{bce}(cs_i)\right)$, where F is the cumulative distribution function identifying the fraction of bubbles below the threshold required to rupture cells in a specified range, the overall rate equation is rewritten as:

$$\frac{dN_c}{dt} = N_B \sum_i k_i N_{c,i,w}\left(1 - F_{bce}(cs_i)\right)$$

When interpreted in the context of F_{cs}, five observable behaviors are expected as F_{bce} is translated horizontally across F_{cs}. Where $F_{bce}(cs_1) = 1$, the rate is zero because the cavitation energies available are insufficient to rupture any cells. The opposite case is more representative of practice. Where $F_{bce}(cs_n) = 0$, the rate becomes independent of f_{bce}, as all cavitation energies available are sufficient to rupture any cells. This scenario ensures that all cells may be ruptured and increases the rupture rate, but requires input of excess ultrasound energy to achieve.

The set of intermediate cases, $F_{bce,j}\left(cs_{(i>1)}\right) = 1$, can be evaluated using the final extents of reaction, $X_j(t=\infty) = F_{cs}\left(bce_{F_{bce,j}=1}\right)$. Thus, $bce_{F_{bce,j}=1} = F_{cs}^{-1}\left(X_j(t=\infty)\right)$. The upper boundary of this intermediate set lies at $F_{bce}\left(cs_{(n)}\right) = 1$, and represents minimal matching of the discrete activation and available energies to achieve $X(t=\infty) = 1$. However, no information about f_{bce} can be extracted from bulk rupture experiments other than its maximum value.

A set of transitional cases is defined where $1 > F_{bce,j}(cs_n) > 0$. Here, $X(t=\infty) = 1$, and there is no cell rupture corollary (other than rate) in this range.

One potential path to extract additional information about $F_{bce,j}(cs_i)$ and N_B would be to determine $k_i^* = N_B k_i\left(1 - F_{bce}(cs_i)\right)$ from experiment. The resultant k_i^* would trace a reflection of the bubble collapse energy distribution, in the region of CDF overlap, scaled by a constant equal to $N_B k_i$. The integral of F_{bce} outside the bounds [cs_1, cs_n] represents non-ideal energy matching. Low-value cavitation energy wasted in the system is identified as $F_{bce}(cs_1) > 0$, and energy of excessive value as $F_{bce}(cs_n) < 1$. This could be quantified as $E_w = N_B\left(\int_{min}^{max} F_{bce} - \int_{cs_1}^{cs_n} F_{bce}\right)$ only where F_{bce} had been determined. However, the value of the integral of F_{bce} in the overlapping region could be used as a relative figure of merit along with a characterization of energy wastage and/or excessive value. In order to achieve this, a method for the measurement or estimation of k_i^* is required.

The overall reaction rate stated in the elementary reaction model section above is affiliated with reactor zone 1 and equated with r_1.

$$\frac{dN_c}{dt} = N_B \sum_i k_i N_{c,i,w}\left(1 - F_{bce}(cs_i)\right)$$

The number of unknowns in this equation can be reduced from 3n+2 to n+1 and further by re-lumping constants, minimizing the grid size for discretization, and implementing a physical filter bank to bin cells by size and thus strength. This treatment assumes sufficient N_B to prevent competitive effects, and is summarized in the matrix equation below with the increasing derivative subscripts denoting individual treatment bins with increasing filter mesh size.

$$\begin{bmatrix} k_1^* & 0 & 0 & & 0 \\ k_1^* & k_2^* & 0 & \dots & 0 \\ k_1^* & k_2^* & k_3^* & & 0 \\ & \vdots & & \ddots & \vdots \\ k_1^* & k_2^* & k_3^* & \dots & k_n^* \end{bmatrix} \begin{bmatrix} N_1 \\ N_2 \\ N_3 \\ \vdots \\ N_n \end{bmatrix} = - \begin{bmatrix} dN/dt|_1 \\ dN/dt|_2 \\ dN/dt|_3 \\ \vdots \\ dN/dt|_n \end{bmatrix}$$

However, the individual reaction rate constants are not mathematically separable and cannot be directly determined individually without fluorescence flow cytometry, a technology currently unavailable to our group.

5.4 Reaction Mechanism and Critical Distance

The assumed interaction, relative energy, and proximity of the reaction mechanism are lumped in practical empirical correlations. The first two of these assumptions were addressed in the elementary reaction model section above. To

address the issue of proximity, an alternative reaction mechanism is presented and used to theoretically derive the first order rate constant for microbial cell rupture under ultrasound induced cavitation.

The mechanical shear [134], mechanical acoustic resonance [110], and kinetic [64] models of cell disruption under ultrasound cavitation are useful frameworks for cell disruption rate and energy studies. However, each is incomplete on its own. The kinetic model recognizes a generic energy of interaction, focusing on empirical curve fitting to provide direct practical knowledge. The mechanical acoustic resonance model ignores the influence of cavitation in cell disruption by cavitation. It offers a potentially valid but separate mechanism of cell disruption in the high frequency (MHz) regime that will not be applicable at low frequency (kHz). The mechanical shear model implements the parameter of critical distance, which is analogous to the kinetic model rate constant but makes explicit the mechanical mechanism of rupture.

The mechanical shear model defines a critical distance (l_c) of a system as the distance from a cell surface within which cavitation bubble collapse occurring leads to disruption of the cell. The critical distance is used as a floating lumped parameter to represent the unknown system of bubble collapse shear force (a function of cell to bubble relative distance and bubble collapse velocity) and cell wall "shear" strength that define the criticality of the interaction of a single bubble-cell pair.

The conceptual framework begins with the assumption that cells are distributed in solution in a random close-pack configuration with a defined cell volume fraction. This allows the calculation of the half distance between cell surfaces (δ), defining the

spherical boundary of a system of a single cell. Probability of an interaction being critical (ψ_c) is defined for a single cell as the ratio of annular volume from the cell surface to l_c and the annular volume from the cell surface to δ. While the size and position distributions of cavitation bubbles are unknown [106, 111, 138], there are implicit assumptions here that the spatial distribution is random and the bubble size is single valued. The number rate of cell disruption (M_k) is then taken as the product of the number of cavitations generated per time (ϕ) and probability of critical co-location ψ_c, creating a two parameter (ϕ and l_c) family of solutions.

$$M_k = \phi\psi_c$$

This simplification is an elegant implementation of spatial probability to define reaction rate in terms of the outcome of a single interaction, but it is developed under extremely limiting assumptions. The foremost simplification assumes that all bubble-cell combinations have a critical distance, which they may not.

The critical distance conceptual framework presented in [134] is developed here into a theoretical framework, implementing some corrections and alternative assumptions.

The extrapolation of ψ_c from a single cell to a reactor volume $\psi_{c,r}$ requires that the non-cell annular volume be defined by the void fraction of the entire reactor rather than the single cell system volume and that the critical volume be scaled by the number concentration of cells in the system (N_c).

$$\psi_{c,r} = \frac{\frac{4}{3}\pi\left((r+l_c)^3 - r^3\right)N_c}{V_T - \frac{4}{3}\pi r^3 N_c}$$

From this expression, the limits of probability, [0, 1], can be used to derive the potential range of l_c: $0 \leq l_c \leq \left(\frac{3}{4\pi N_c}\right)^{1/3} - r$.

Substituting $\psi_{c,r}$ in the critical diameter cell disruption rate equation with $dN_c/dt = -M_k/V_1$ and rearranging gives a theoretically derived, non-integer order rate equation with no explicit empirical rate constant:

$$\frac{dN_c}{dt} = \left(\frac{-4\pi\phi}{V_1}\left((r + l_c)^3 - r^3\right)\right) \times \frac{N_c}{(3 - 4\pi r^3 N_c)}$$

Recognizing the magnitudes of cell radius (~10^{-6} m) and concentration (~10^{13} m^{-3}), the second term in the denominator of the quotient on the right becomes negligible (~10^{-5}). Thus the non-integer order rate equation becomes a first order rate equation, as is observed in experiment.

$$\frac{dN_c}{dt} = -kN_c \quad ; \quad k = \frac{4\pi\phi}{3V_1}\left((r + l_c)^3 - r^3\right)$$

Now l_c is expanded to make explicit the combined influence of bubble collapse energy, cell strength, and relative position on disruption rate. A collapsing bubble near a surface induces a local velocity gradient between the bubble and the surface. Assuming for simplicity that the flow is steady across the surface, a liquid shear stress of $\sigma \approx \frac{\mu v}{l}$ (μ= dynamic viscosity, v= velocity, l= distance from the surface to the

bubble surface) acts tangent to the surface [139] in radial spokes toward a point sink where the cell surface is co-normal to the bubble.

A mass balance can be applied to the cylindrical column of height (h) below the bubble collapse footprint to estimate an average velocity (v) at the boundary for mass flux. The height is calculated in 2 regimes. Where the bubble radius (r_b) is greater than the cell diameter (r), h is taken as extending to the equatorial plane of the cell, $h = r_b + l + r$. Where $r_b < r$, h decreases as the projection of the bubble on the cell moves up the cell surface, $h = r_b + l + r - \sqrt{r^2 - r_b^2}$. Assuming an incompressible liquid solvent, volume replacement for the cell-adjacent bubble hemi-sphere only, and collapse time equal to half the period of the ultrasound driving frequency (f), the average velocity (v) is $v = (4fr_b)/3h$. Assuming a linear velocity profile and no-slip condition at the surface, the velocity at height h in the velocity profile will be twice the average. Substituting the variations of h gives:

$$v = \begin{cases} \dfrac{8fr_b}{3(r_b + l + r)} & ;\ r_b \geq r \\ \dfrac{8fr_b}{3\left(r_b + l + r - \sqrt{r^2 - r_b^2}\right)} & ;\ r_b < r \end{cases}$$

The fluid shear stress is applied as a tangential force on the cell wall surface over the projection area (a spherical cap), generating a wall tension force along the perimeter of the projection. This tension force exerted across the thickness of the cell wall (T_{cw}) along this perimeter will exert a tension stress (σ_T) in the cell wall material. The condition for cell rupture under this mechanism is then that σ_T be greater than or equal to the tensile strength of the cell wall material (TS_{cw}). Under this condition σ is

denoted as critical (σ_c) and the distance between the cell and bubble surfaces (l) becomes the critical distance (l_c).

$$\sigma_T = \left\{ \begin{array}{ll} \dfrac{\sigma r}{T_{cw}} & ;\ r_b \geq r \\ \dfrac{\sigma\left(r_b^2 + \left(r - \sqrt{r^2 - r_b^2}\right)^2\right)}{2T_{cw} r_b} & ;\ r_b < r \end{array} \right\} \geq TS_{cw}$$

Solving for σ_c in terms of TS_{cw}:

$$\sigma_c = \left\{ \begin{array}{ll} \dfrac{TS_{cw} T_{cw}}{r} & ;\ r_b \geq r \\ \dfrac{2TS_{cw} T_{cw} r_b}{r_b^2 + \left(r - \sqrt{r^2 - r_b^2}\right)^2} & ;\ r_b < r \end{array} \right.$$

Critical distance (l_c) is then defined in terms of σ_c:

$$l_c = \frac{\mu v}{\sigma_c} = \left\{ \begin{array}{ll} \dfrac{8\mu f r_b r}{3TS_{cw} T_{cw}(r_b + l_c + r)} & ;\ r_b \geq r \\ \dfrac{4\mu f\left(r_b^2 + \left(r - \sqrt{r^2 - r_b^2}\right)^2\right)}{3TS_{cw} T_{cw}\left(r_b + l_c + r - \sqrt{r^2 - r_b^2}\right)} & ;\ r_b < r \end{array} \right.$$

And solving for l_c produces:

$$l_c = \left\{ \begin{array}{ll} \dfrac{\pm\sqrt{\left(3TS_{cw} T_{cw}(r_b + r)\right)^2 + 96\mu f r_b r TS_{cw} T_{cw}} - 3TS_{cw} T_{cw}(r_b + r)}{6TS_{cw} T_{cw}} & ;\ r_b \geq r \\ \dfrac{1}{6TS_{cw} T_{cw}}\left[\pm\left(\left(3TS_{cw} T_{cw}\left(r_b + r - \sqrt{r^2 - r_b^2}\right)\right)^2 \right.\right. & ;\ r_b < r \\ \left.\left. +96\mu f r TS_{cw} T_{cw}\left(r - \sqrt{r^2 - r_b^2}\right)\right)^{1/2} - 3TS_{cw} T_{cw}\left(r_b + r - \sqrt{r^2 - r_b^2}\right)\right] & \end{array} \right.$$

In conjunction with the first order rate equation, $\frac{dN_c}{dt} = -kN_c \;\; ; \;\; k = \frac{4\pi\phi}{3V_1}((r + l_c)^3 - r^3)$, and the recognition that ϕ will be dependent on power, the determination of l_c has resulted in the derivation of an expression for the first order rate constant as an explicit function of the operational parameters of microbial cell disruption under ultrasound induced cavitation.

$$k = k(\phi(P), V_1, \mu, f, r_b, r, TS_{cw}, T_{cw})$$

5.5 Rate Constant Mapping

The reaction zone volume is reasonably assumed to be isolated to the cavitation cone produced at the face of a sonotrode. Based on visual observations of turbidity at sonotrode faces, the cavitation cone has a height approximately equal to the diameter ($2r_s$) of the sonotrode face, and $V_1 = 2\pi {r_s}^3/3$. For r_s=1.5875E-3m, V_1=8.379E-9 m^3.

Typical cavitation bubble radii are 1-5µm [140]. Observed average cell radius for Chlorella vulgaris is ~4µm. Typical low frequency power ultrasound runs from 20-100kHz [140].

The viscosity is held at 890µPa-s assuming a temperature of 25°C in aqueous solution. T_{cw} is approximately 100nm [141] and TS_{cw} is 638MPa [87]. When not varied, f=20kHz, r=4µm, r_b=3µm, and ϕ=1E6s^{-1}.

The interaction of these parameters in an isothermal, isochoric, system with a single cell wall type is $k(\phi, f, r_b, r)$ shown below in Figure 5.1-5.6 (ϕ indicated as

phi). An anomalous wrinkle is observed in all the contours of Figures 5.2-5.6, but not in Figure 5.1, which does not include any variation of either bubble or cell radius. The vertical nature of the transition in Figures 5.2, 5.4, and 5.5 suggests a threshold in ultrasound frequency and cavitation rate for the effect of both r and r_b on k. The slope of the transition line in Figure 5.6 not equaling 1 suggests that the transition between velocity models at the equality of r and r_b does not cause the anomaly.

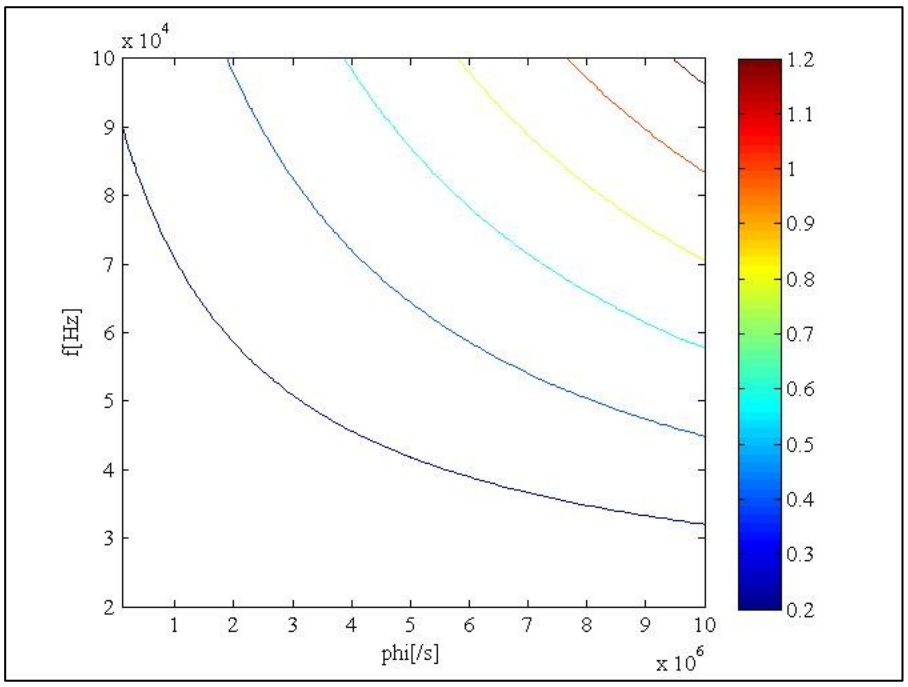

Figure 5.1 – Cell disruption rate constant over frequency and cavitation rate

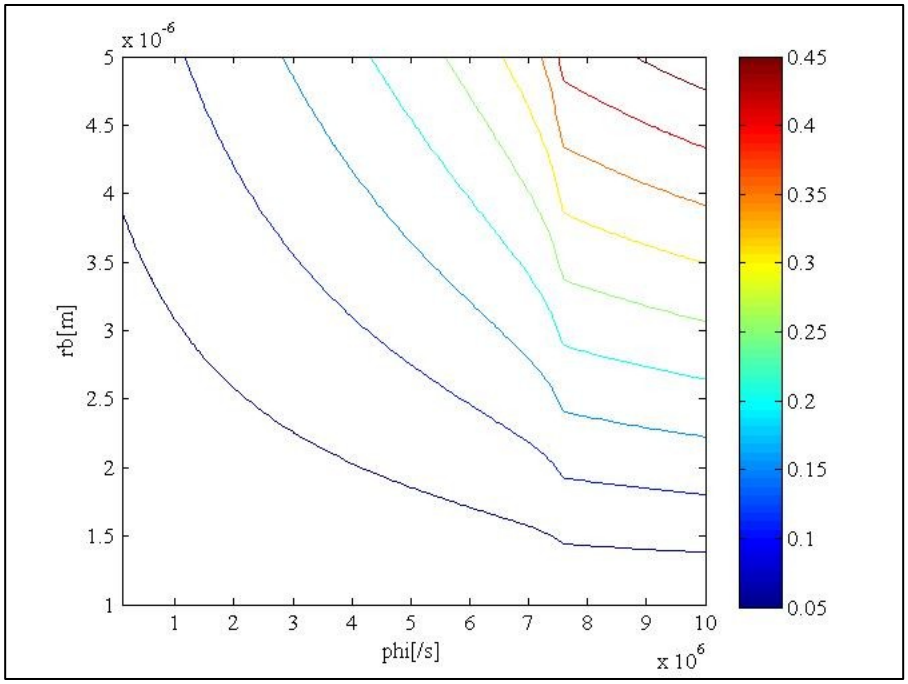

Figure 5.2 – Cell disruption rate constant over bubble radius and cavitation rate

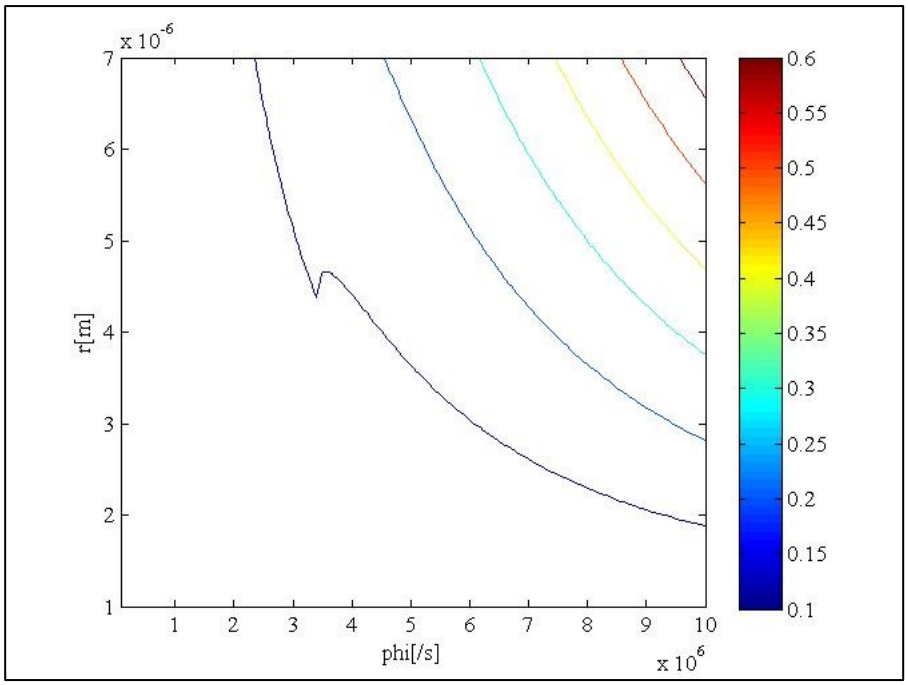

Figure 5.3 – Cell disruption rate constant over cell radius and cavitation rate

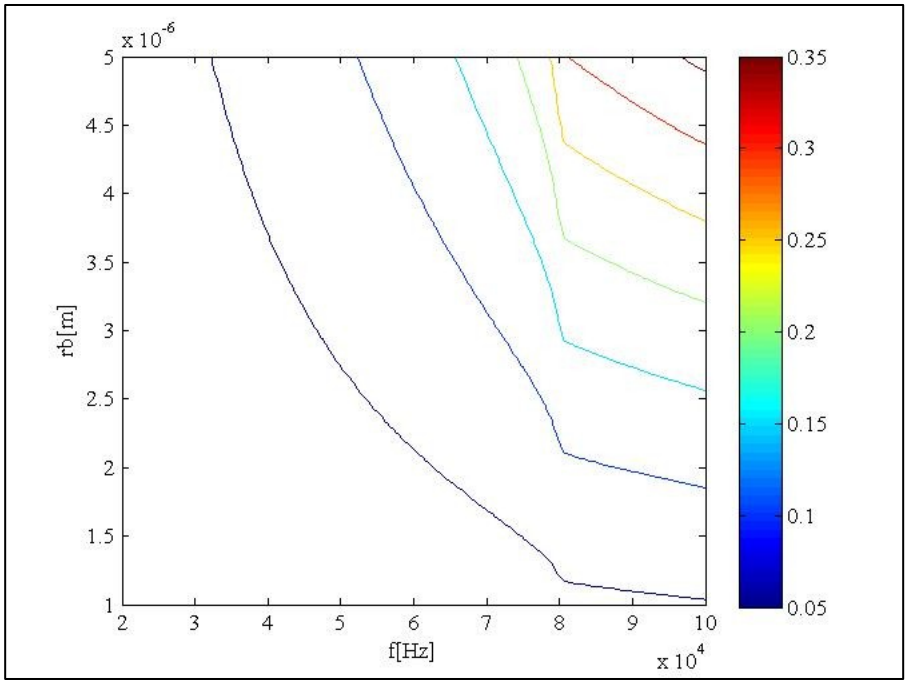

Figure 5.4 – Cell disruption rate constant over bubble radius and frequency

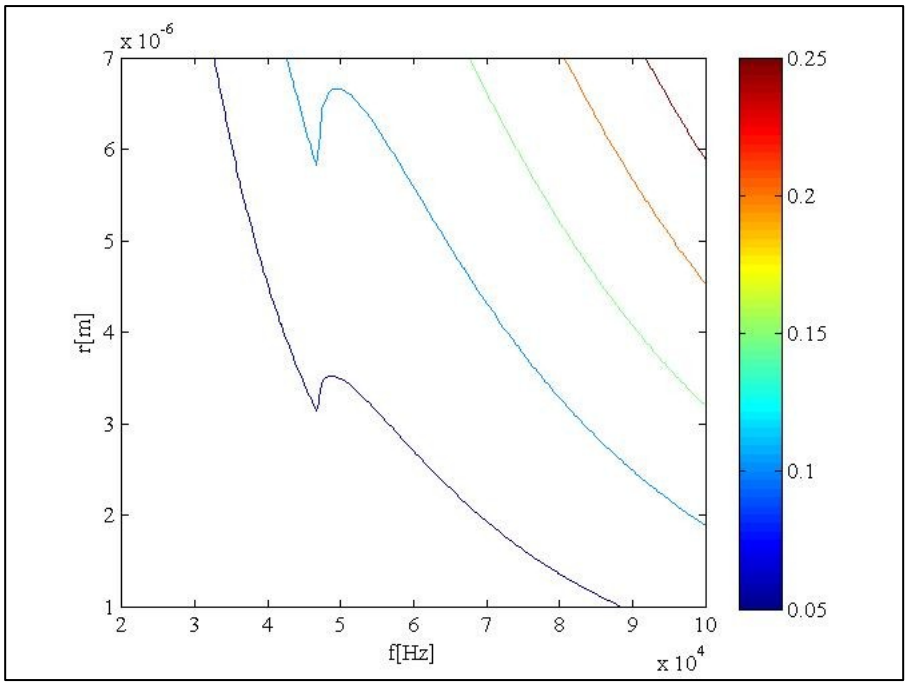

Figure 5.5 – Cell disruption rate constant over cell radius and frequency

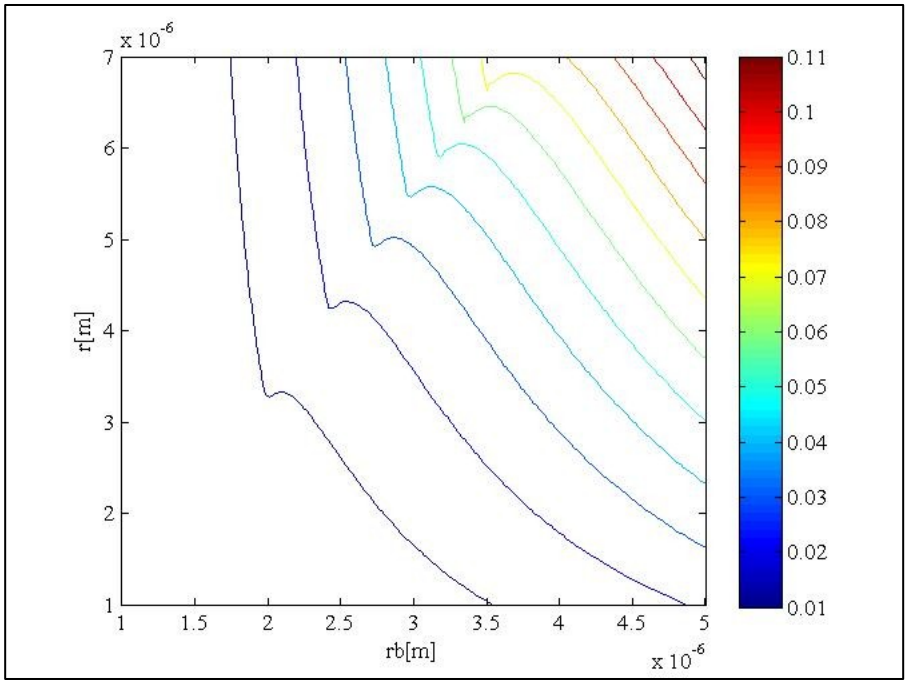

Figure 5.6 – Cell disruption rate constant over cell radius and bubble radius

5.6 Prediction of Cavitation Rate

A cell disruption first order rate constant of 0.0411/min (6.85×10^{-4}/s) was observed in Chapter 2.3 for Chlorella vulgaris treated at 20kHz using a 1/8 inch diameter sonotrode in a 50ml reactor volume.

Based on the re-circulating reactor model, the zone 1 reaction rate constant for Chlorella disruption under these conditions will be a function of the acoustic streaming driven re-circulation flow rate (Q), $k_1=f(Q)$.

If the typical bubble radius is left as a free variable, then the critical distance model is now $k_1=g(\phi,r_b)$. Then $f(Q)= g(\phi,r_b)$ and there are three unknowns remaining

in the system (Q, r_b, ϕ). Because ϕ is least amenable to estimation, the system is parameterized in terms of Q and r_b.

A first estimate of Q is produced from the zone 1 volume (V_1=8.379 x10^{-9} m^3) and ultrasound frequency (20kHz). Assuming a maximum flow rate caused by an expulsion of the entire zone 1 volume with each stroke, $Q = f V_1$, the maximum flow rate is Q=167.58 x10^{-6} m^3/s. This estimate of 168ml/s is unrealistically high, representing more than 3 passes of the entire 50ml reactor volume per second.

An alternative estimate of Q can be made using the volume of displacement of the sonotrode face during a single cycle. The amplitude of tip displacement (A) can be estimated according to $P_{diss} = \frac{1}{2}A^2(2f\pi)^2SZ$ [104], using calorimetric power dissipated to solution (P_{diss}), acoustic impedance of the solution (Z=1.484 x10^6 kg·m^{-2}·s^{-1} for water), ultrasound frequency (f=20,000Hz), and sonotrode face area (S=7.917 x10^{-6} m^2). With average P_{diss} for old and new Q55 sonotrode microtips observed in Chapter 2.2 as 8.13W, A=9.362 x10^{-6} m, and $V = S A$ =7.412 x10^{-11} m^2 leads to $Q = V f$ =1.482 x10^{-4} m^3/s. This estimate of 1.5ml/s is much more realistic and will be used as a median value.

The model equation to predict cavitation rate is presented below, and its result is displayed in Figure 5.7. The predicted rate of cavitation generation is on the order of 10^8/s.

$$\phi = \frac{3V_1k_1}{4\pi((r+l_c)^3 - r^3)}; \quad k_1 = \frac{Q\left(1+\frac{V_2}{V_1}\right)k - V_2k^2}{Q - V_2k}$$

$$\phi = \frac{3Q(V_1 + V_2)k - V_1V_2k^2}{4\pi((r + l_c)^3 - r^3)(Q - V_2k)}$$

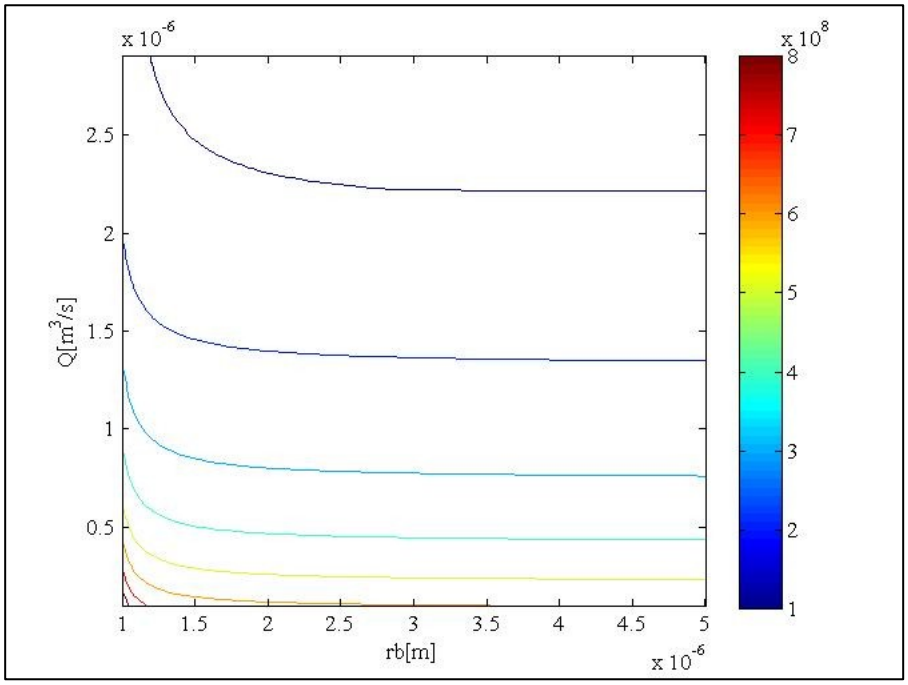

Figure 5.7 – Cavitation rate as a function of bubble radius and streaming flow rate for known reactor rate constant

These figures display the outputs of combinations of single value inputs. Inputs with frequency distributions require additional treatment.

5.7 Treatment of PDF Inputs

In order to determine k_i^*, the distribution of cell radii is binned, and all operations are performed for a cell concentration input for a single cell radius bin, N_i. For constant frequency and cavitation rate within a single cell radius bin, $k(\phi, f, r_b, r)$ becomes $k(r_b)$.

The disruption rate constant $k \rightarrow 0$ only where $l_c \rightarrow 0$, and $l_c \rightarrow 0$ only where $r_b \rightarrow 0$. Thus all bubble-cell interactions have a critical distance, and there is no lower threshold for exclusion of low-energy bubbles under the mechanical shear critical distance disruption mechanism.

Assuming a distribution of r_b, this distribution is binned and multiplied by the cavitation rate to generate ϕ_j for each bubble bin. The bin disruption rate constant $k_{i,j}$ is then evaluated for all bin combinations.

Thus, $\frac{dN_c}{dt} = N_B \sum_i k_i N_{c,i,w}\left(1 - F_{bce}(cs_i)\right)$ is translated to $\frac{dN_c}{dt} = \sum_i {k_i}^* N_{c,i,w}$, and ${k_i}^* = N_B k_i\left(1 - F_{bce}(cs_i)\right)$ becomes $k_i^* = \sum_j k_{i,j}\left(\phi_j, r_{b,j}\right)$.

This requires an assumed distribution of r_b, which is the same issue as was encountered above in the kinetic mechanism approach. However, when compared to the expression $k_i^* = N_B k_i\left(1 - F_{bce}(cs_i)\right)$, the critical diameter based ${k_i}^*$ has one fewer unknown in the absence of k_i.

5.8 Conclusions

A generalized correction factor has been derived for the normalization of the cell disruption rate constant determined in any sonotrode test system. An elementary reaction model used to describe the second order interaction of cells and cavitation bubbles defaults to a first order rate relationship under the assumption of steady state cavitation generation. The first order rate constant can be interpreted as the product of cavitation rate, an interaction rate constant, and an overlap of the cumulative

distribution functions of constitutive cell strength and cavitation energy. A mechanical shear reaction model has been used to create an alternative constant for the first order rate equation. The expression for this rate constant removes lumped parameters, resulting in an explicit expression for the rate constant in terms of the operational inputs of cell disruption under power ultrasound. The rate constant exhibits anomalous patterns as a function of cell and bubble radii, and these were determined to not be a model artifact. A known set of system parameters was used to estimate the cavitation rate under a 1/8 inch, 20kHz, 8.13W sonotrode to be on the order of $10^8 s^{-1}$. The derived reaction rate constants are also amenable to the incorporation of PDF inputs for cavitation and cell radii.

Chapter 5, in part, has been submitted for publication of the material as it may appear in Ultrasonics Sonochemistry, 2017, Klinger, Rory; Garoma, Temesgen, Elsevier, 2017. The dissertation author was the primary investigator and author of this material.

Chapter 6 – **Conclusions**

6.1 Summary

Continually rising energy needs in conjunction with negative externalities of fossil fuel use demand the diversification of energy resources. However, fossil hydrocarbons are also used as raw materials for a vast web of manufacturing of industrial and consumer goods. The use of plant based raw materials as substitutes for fossil materials in fuels and manufacturing has been demonstrated successfully, and microalgae are an extremely diverse and promising resource in this category. One of the chief challenges in the implementation of a bio-economy is efficient processing and conversion of biomass to platform chemicals. In order to maximize extraction efficiency, pretreatment is employed to effect cell rupture. Many pretreatment processes have been implemented using empirical operating curves, but the fundamental energy requirements of the cell disruption process have not been thoroughly explored.

A constitutive model of cell rupture energy was derived here and implemented for low frequency power ultrasound processing of *Chlorella vulgaris*. A sensitivity analysis of the constitutive model was performed, identifying cell diameter as a high sensitivity input. Measured distribution of microalgae cell diameters was then used as a fixed input to Monte Carlo simulations of cell rupture energy from the constitutive

model. The influence of growth media on microalgal growth rate was then investigated, and the resultant biomass subjected to power ultrasound processing to determine the effect of media choice on processing efficiency.

The theoretical kinetics of cell rupture via power ultrasound induced cavitation was developed next. A reactor model was introduced to convert reactor kinetics to reaction zone kinetics. An elementary reaction model was then developed in the context of the constitutive model, leading to the introduction of an alternative reaction mechanism employing a critical distance parameter to capture the relative energies and proximity of cells and cavitation bubbles. This reaction mechanism was extended to generate an explicit expression for the cell disruption first order rate constant in terms of cell properties and power ultrasound operating parameters. This rate constant was mapped over the parameter space, then used to back-calculate cavitation rate, and finally extended to incorporate PDF parameter inputs.

6.2 Conclusions

Evaluation of the constitutive model in the context of experimental results led to two sets of conclusions about the constitutive behavior of microalgae cells. Six of 15 proposed model variants were eliminated to reveal that either: the volume of material considered in the rupture energy calculation is not strain based, and the cell wall does not exhibit highly elastic behavior; or the volume of material is strain based and is highly elastic. It was also observed that cylindrical cells will require 1-2 orders of magnitude greater energy to rupture than spherical cells.

The calorimetric power transferred to solution in the tested low frequency power ultrasound systems ranged from 5.59-9.27 W. Additional differentiation by mixing delay and analysis of the results in the context of non-linear acoustic theory led to classification of reactors in terms of acoustic streaming and acoustic heating. The 50ml Kimble jacketed beaker was chosen for further tests based on inferred lower interference with cavitation due to high streaming and heating behavior. Calorimetric efficiencies of the systems were relatively consistent, and the power transfer of a smooth probe tip could not be differentiated from that of an eroded tip face. A mechanism was proposed to explain this lack of difference between smooth and eroded tip faces. Additional characterization of energy partitioning between linear and non-linear acoustic phenomena is required moving forward in the field, but the inference methods presented here facilitate decision making and classification where direct measurement is impossible or impractical.

The power ultrasound treatment of *Chlorella vulgaris* required 18 – 76μJ ultrasound energy input per cell ruptured. The 4 order of magnitude difference between observed and predicted energy requirement may be due to power transfer efficiencies inherent in the treatment method. The rupture rate fit a first order disruption model relatively well. However, high variance observed in cell rupture energy requirement implied a need to expand the constitutive model of cell rupture to incorporate the variability of model inputs. The requirement of additional model expansion was anticipated to incorporate the observed first order disruption behavior.

Sensitivity analysis of the constitutive model of cell rupture revealed high order of influence model inputs, facilitating improvement via experimental measurement. A simplified constitutive model of cell rupture energy predicted both first and second order dependencies on the 5 tested inputs. An anticipated variation of ±90% in each input produces potential for energy ranges scaled by $10 - 10^9$. OVAT analysis of the non-simplified constitutive model found that the simplified model orders of dependency on each input match those of the non-simplified model. Variation of only the 2 high influence inputs in the non-simplified model produce range scaling lower than that predicted by the same variation in the simplified model. Random variation of all inputs to the non-simplified model produced energy range scaling from 10^4 - 10^7, a smaller range than predicted by the simplified model. Results indicate that cell diameter and failure strain are the most influential inputs, and that the simplified model should not be used because of a significant and unnecessary loss in precision.

Monte Carlo simulations of constitutive cell rupture energy produced distributions with ranges of approximately 2 orders of magnitude. This was a drastic improvement in precision from the results of sensitivity analysis. Cell diameter was observed to follow a log-normal distribution. Substitution of the measured cell diameter distribution for the assumed distribution in Monte Carlo simulations resulted in a negative shift of the energy distributions, but negligible change in precision for any single model variant. Interpretation of the CDFs of rupture energy in terms of E_{90} revealed that the measurement of cell diameter reduced the spread of modeled rupture

energy across the suite of model variants by a factor of approximately 7, a drastic improvement in overall model precision.

The evaluation of growth media influence on microalgal growth and susceptibility to power ultrasound revealed unsatisfactory performance of some established media, and a surprising difference in rate of cell constituent solvation. BBM was found to be the best medium for rate of *Chlorella vulgaris* biomass production. MiracleGro showed the highest rate of solvation of COD. The amount of solvation was also proportionally higher than in other media on a per cell rupture basis, which was unexpected based on observed consistent biomass quality among growth media. Media differences did not appear to have an effect on ultrasound power transfer, and thus *Chlorella vulgaris* grown in MiracleGro medium has a decreased strength in terms of resistance to rupture by ultrasound. These results suggest that while biomass productivity and composition are important for the efficiency of extraction, media effects on the susceptibility of cells to pretreatment should not be ignored in overall process design.

In developing the theoretical kinetics of cell disruption by ultrasound cavitation, a generalized correction factor was derived for the normalization of the cell disruption rate constant determined in any sonotrode test system. An elementary reaction model used to describe the second order interaction of cells and cavitation bubbles was found to default to a first order rate relationship under the assumption of steady state cavitation generation. The first order rate constant was interpreted as the product of cavitation rate, an interaction rate constant, and an overlap of the

cumulative distribution functions of constitutive cell strength and cavitation energy. A mechanical shear reaction model was used to create an alternative constant for the first order rate equation. The expression for that rate constant removed lumped parameters, resulting in an explicit expression for the rate constant in terms of the operational inputs of cell disruption under power ultrasound. The rate constant exhibited anomalous patterns as a function of cell and bubble radii, and these were determined to not be a model artifact. A known set of system parameters was used to estimate the cavitation rate under a 1/8 inch, 20kHz, 8.13W sonotrode to be on the order of $10^{8}s^{-1}$. The derived reaction rate constants were made amenable to the incorporation of PDF inputs for cavitation and cell radii.

6.3 Future Directions

Future work should address the balance of productivity and susceptibility to rupture in terms of relative induced extraction potential per cell mass and biomass composition. Cell size bin reaction rate constants should be measured using fluorescence flow cytometry to infer the distribution of cavitation bubble energies in power ultrasound systems. Mapping of reactor independent cell disruption rate constants could also be extended to unify future cell disruption system characterizations.

Bibliography

1. Administration, U.S.E.I., *International Energy Outlook 2013 with Projections to 2040*, U.S.D.o. Energy, Editor. 2013, U.S. Department of Energy: Washington, D.C.

2. Administration, U.S.E.I., *Annual Energy Outlook 2012 with Projections to 2035*, U.S.D.o. Energy, Editor. 2012, U.S. Department of Energy: Washington, D.C.

3. Administration, U.S.E.I., *Annual Energy Outlook 2014 with Projections to 2040*, U.S.D.o. Energy, Editor. 2014, U.S. Department of Energy: Washington, D.C.

4. SMIL, V., *Energy Transitions : History, Requirements, Prospects*. 2010, ABC-CLIO: Santa Barbara.

5. Fishman, D.e., et al., *National Algal Biofuels Technology Roadmap*, U.D.o. Energy, Editor. 2010, US Department of Energy, Office of Energy Efficiency and Renewable Energy, Biomass Program.

6. States, t.C.o.t.U., *Energy Policy Act of 2005*, in *109-58*, U.S. Congress, Editor. 2005, U.S. Government Printing Office: Washington, D.C.

7. States, t.C.o.t.U., *Energy Independence and Security Act of 2007*, in *110-140*, U.S. Congress, Editor. 2007, U.S. Government Printing Office: Washington, D.C.

8. Vieira Da Rosa, A., *Fundamentals of Renewable Energy Processes*. 3rd ed. 2013, Oxford, UK: Academic Press. 884.

9. DOE-EERE, *Replacing the Whole Barrel To Reduce U.S. Dependence on Oil*, B.T.O. Department of Energy, Editor. 2013: Washington, D.C.

10. Energy, S. *What Is Green Crude?* [Corporate Webpage] 2014 [cited 2014 2014-11-04]; Available from: http://www.sapphireenergy.com/green-crude.

11. DOE-EERE, *Bioenergy Technologies Office: Multi-Year Program Plan*, U.S.D.o. Energy, Editor. 2013: Washington D.C.

12. Meier, R.L., *Biological cycles in the transformation of solar energy into useful fuels.*, in *Solar Energy Research*, F.D. Daniels, John A., Editor. 1955, University of Wisconsin Press: Madison. p. 290.

13. Oswald, W.J.G., Claeence G., *Biological Transformation of Solar Energy*, in *Advances in Applied Microbiology*. 1960. p. 223-262.

14. Bird, K.T.B., P.H., ed. *Seaweed Cultivation for Renewable Resources*. Developments in Aquaculture and Fisheries Science. 1987, Elsevier Science Ltd. 396.

15. Sheehan, J., et al., *A look back at the US Department of Energy's Aquatic Species Program: Biodiesel from Algae*, U.D.o. ENergy, Editor. 1998, National Renewable Energy Laboratory.

16. Eisentraut, A.a.B., Adam, *Technology Roadmap: Bioenergy for Heat and Power*. 2012, International Energy Agency. p. 68.

17. Olivares, J.A.P., *National Alliance for Advanced Biofuels and Bioproducts Synopsis (NAABB) Final Report*, U.D.o.E.-O.o.E.E.a.R. Energy, Editor. 2014.

18. Stocker, M., *Biofuels and biomass-to-liquid fuels in the biorefinery: catalytic conversion of lignocellulosic biomass using porous materials.* Angew Chem Int Ed Engl, 2008. **47**(48): p. 9200-11.

19. Yue, D., F. You, and S.W. Snyder, *Biomass-to-bioenergy and biofuel supply chain optimization: Overview, key issues and challenges.* Computers & Chemical Engineering, 2014. **66**(0): p. 36-56.

20. Cherubini, F., *The biorefinery concept: Using biomass instead of oil for producing energy and chemicals.* Energy Conversion and Management, 2010. **51**(7): p. 1412-1421.

21. Ponce-Ortega, J.M., et al., *A Disjunctive Programming Formulation for the Optimal Design of Biorefinery Configurations.* Industrial & Engineering Chemistry Research, 2012. **51**(8): p. 3381-3400.

22. Alonso, D.M., J.Q. Bond, and J.A. Dumesic, *Catalytic conversion of biomass to biofuels.* Green Chemistry, 2010. **12**: p. 21.

23. Pham, V. and M. El-Halwagi, *Process synthesis and optimization of biorefinery configurations.* AIChE Journal, 2012. **58**(4): p. 1212-1221.

24. Román, S., et al., *Hydrothermal carbonization as an effective way of densifying the energy content of biomass.* Fuel Processing Technology, 2012. **103**: p. 78-83.

25. Pragya, N., K.K. Pandey, and P.K. Sahoo, *A review on harvesting, oil extraction and biofuels production technologies from microalgae.* Renewable and Sustainable Energy Reviews, 2013. **24**(0): p. 159-171.

26. DOE-EERE, *Bioenergy Technologies Office: Office Overview*. 2013: Washington, D.C.

27. Bennemann, J.R., *Overview Algae oil to biofuels*. 2008, NREL.

28. Brennan, L. and P. Owende, *Biofuels from microalgae—A review of technologies for production, processing, and extractions of biofuels and co-products.* Renewable and Sustainable Energy Reviews, 2010. **14**(2): p. 557-577.

29. Mercer, P. and R.E. Armenta, *Developments in oil extraction from microalgae.* European Journal of Lipid Science and Technology, 2011. **113**(5): p. 539-547.

30. Suali, E. and R. Sarbatly, *Conversion of microalgae to biofuel.* Renewable & Sustainable Energy Reviews, 2012. **16**(6): p. 4316-4342.

31. Darzins, A.P., Philip; and Edye, Les, *Current Status and Potential for Algal Biofuels Production*. 2010, International Energy Agency. p. 146.

32. Liew, W.H., M.H. Hassim, and D.K.S. Ng, *Review of evolution, technology and sustainability assessments of biofuel production.* Journal of Cleaner Production, 2014. **71**(0): p. 11-29.

33. Middelberg, A.P.J., *Process-scale disruption of microorganisms.* Biotechnol Adv, 1995. **13**(3): p. 491-551.

34. Williams, P.J.l.B. and L.M.L. Laurens, *Microalgae as biodiesel & biomass feedstocks: Review & analysis of the biochemistry, energetics & economics.* Energy & Environmental Science, 2010. **3**(5): p. 554.

35. Hughes, D.E., J.W.T. Wimpenny, and D. Lloyd, *Chapter I The Disintegration of Micro-organisms*, in *Methods in Microbiology*, J.R. Norris and D.W. Ribbons, Editors. 1971, Academic Press. p. 1-54.

36. Chisti, Y. and M. Moo-Young, *Disruption of microbial cells for intracellular products.* Enzyme and Microbial Technology, 1986. **8**(4): p. 194-204.

37. Geciova, J., *Methods for disruption of microbial cells for potential use in the dairy industry-a review.* International Dairy Journal, 2002. **12**: p. 13.

38. Lee, A.K., D.M. Lewis, and P.J. Ashman, *Disruption of microalgal cells for the extraction of lipids for biofuels: Processes and specific energy requirements.* Biomass and Bioenergy, 2012. **46**: p. 89-101.

39. Gonçalves, A., J.M. Pires, and M. Simões, *Green fuel production: processes applied to microalgae.* Environmental Chemistry Letters, 2013. **11**(4): p. 315-324.

40. Harrison, S.T.L., *2.44 - Cell Disruption*, in *Comprehensive Biotechnology (Second Edition)*, M. Moo-Young, Editor. 2011, Academic Press: Burlington. p. 619-640.

41. Bjornsson, W.J., et al., *Pilot-scale supercritical carbon dioxide extractions for the recovery of triacylglycerols from microalgae: a practical tool for algal biofuels research.* Journal of Applied Phycology, 2012. **24**(3): p. 547-555.

42. Lee, S.J., B.-D. Yoon, and H.-M. Oh, *Rapid method for the determination of lipid from the green alga Botryococcus Braunii.* Biotechnology Techniques, 1998. **12**(7): p. 4.

43. Tran, H.L., S.J. Hong, and C.G. Lee, *Evaluation of extraction methods for recovery of fatty acids from Botryococcus braunii LB 572 and Synechocystis sp PCC 6803.* Biotechnology and Bioprocess Engineering, 2009. **14**(2): p. 187-192.

44. Crampon, C., O. Boutin, and E. Badens, *Supercritical Carbon Dioxide Extraction of Molecules of Interest from Microalgae and Seaweeds.* Industrial & Engineering Chemistry Research, 2011. **50**(15): p. 8941-8953.

45. Young, G., et al., *Lipid extraction from biomass using co-solvent mixtures of ionic liquids and polar covalent molecules.* Separation and Purification Technology, 2010. **72**(1): p. 118-121.

46. Šoštarič, M., et al., *Growth, lipid extraction and thermal degradation of the microalga Chlorella vulgaris.* N Biotechnol, 2012. **29**(3): p. 325-331.

47. Kim, Y.H., et al., *Ionic liquid-mediated extraction of lipids from algal biomass.* Bioresour Technol, 2012. **109**: p. 312-315.

48. Couto, R.M., et al., *Supercritical fluid extraction of lipids from the heterotrophic microalga Crypthecodinium cohnii.* Engineering in Life Sciences, 2010. **10**(2): p. 158-164.

49. Nobre, B., et al., *Supercritical carbon dioxide extraction of astaxanthin and other carotenoids from the microalga Haematococcus pluvialis.* European Food Research and Technology, 2006. **223**(6): p. 787-790.

50. Grima, E.M., et al., *Comparison between extraction of lipids and fatty acids from microalgal biomass.* JAOCS, 1994. **71**(9): p. 5.

51. Andrich, G., et al., *Supercritical fluid extraction of bioactive lipids from a the microalga Nannochloropsis sp.* European Journal of Lipid Science and Technology, 2005. **107**(6): p. 381-386.

52. Andrich, G., et al., *Supercritical fluid extraction of oil from microalga Spirulina(arthrospira) platensis.* Acta Alimentaria, 2006. **35**(2): p. 195-203.

53. Fajardo, A.R., et al., *Lipid extraction from the microalgaPhaeodactylum tricornutum.* European Journal of Lipid Science and Technology, 2007. **109**(2): p. 120-126.

54. Mendes, R.L., et al., *Supercritical CO2 extraction of gamma-linolenic acid (GLA) from the cyanobacterium Arthrospira (Spirulina)maxima: experiments and modeling.* Chemical Engineering Journal, 2005. **105**(3): p. 147-152.

55. Mendes, R.L., A.D. Reis, and A.F. Palavra, *Supercritical CO2 extraction of gamma-linolenic acid and other lipids from Arthrospira (Spirulina)maxima: Comparison with organic solvent extraction.* Food Chemistry, 2006. **99**(1): p. 57-63.

56. Macias-Sanchez, M.D., et al., *Supercritical fluid extraction of carotenoids from Scenedesmus almeriensis.* Food Chemistry, 2010. **123**(3): p. 928-935.

57. Widjaja, A., C.C. Chien, and Y.H. Ju, *Study of increasing lipid production from fresh water microalgae Chlorella vulgaris.* Journal of the Taiwan Institute of Chemical Engineers, 2009. **40**(1): p. 13-20.

58. Patil, P.D., et al., *Comparison of direct transesterification of algal biomass under supercritical methanol and microwave irradiation conditions.* Fuel, 2012. **97**: p. 822-831.

59. Rajasekhar, P., et al., *Impact of sonication at 20 kHz on Microcystis aeruginosa, Anabaena circinalis and Chlorella sp.* Water Res, 2012. **46**(5): p. 1473-81.

60. Lee, J.Y., et al., *Comparison of several methods for effective lipid extraction from microalgae.* Bioresour Technol, 2010. **101 Suppl 1**: p. S75-7.

61. Viswanathan, T., et al., *Effect of cell rupturing methods on the drying characteristics and lipid compositions of microalgae.* Bioresour Technol, 2012. **126**(0): p. 131-136.

62. Gouveia, L. and A.C. Oliveira, *Microalgae as a raw material for biofuels production.* Journal of Industrial Microbiology & Biotechnology, 2009. **36**(2): p. 269-274.

63. Halim, R., et al., *Microalgal cell disruption for biofuel development.* Applied Energy, 2012. **91**(1): p. 116-121.

64. Halim, R., et al., *Mechanical cell disruption for lipid extraction from microalgal biomass.* Bioresour Technol, 2013. **140**: p. 53-63.

65. Gerde, J.A., et al., *Evaluation of microalgae cell disruption by ultrasonic treatment.* Bioresour Technol, 2012. **125**: p. 175-81.

66. Cravotto, G., et al., *Improved extraction of vegetable oils under high-intensity ultrasound and/or microwaves.* Ultrasonics Sonochemistry, 2008. **15**(5): p. 898-902.

67. McMillan, J.R., et al., *Evaluation and comparison of algal cell disruption methods: Microwave, waterbath, blender, ultrasonic and laser treatment.* Applied Energy, 2013. **103**: p. 128-134.

68. Gonzalez-Fernandez, C., et al., *Comparison of ultrasound and thermal pretreatment of Scenedesmus biomass on methane production.* Bioresour Technol, 2012. **110**: p. 610-6.

69. Ranjan, A., C. Patil, and V.S. Moholkar, *Mechanistic Assessment of Microalgal Lipid Extraction.* Industrial & Engineering Chemistry Research, 2010. **49**(6): p. 2979-2985.

70. Samson, R. and A. Leduy, *Influence of mechanical and thermochemical pretreatments on anaerobic digestion of Spirulina maxima algal biomass.* Biotechnology Letters, 1983. **5**(10): p. 6.

71. Heger, M. *A new processing scheme for algae biofuels*. 2009 [cited 2014 08/01/2014]; Short article about the company OriginOil]. Available from: http://www.technologyreview.com/news/413325/a-new-processing-scheme-for-algae-biofuels/.

72. Cheng, J., et al., *Dynamic microstructures and fractal characterization of cell wall disruption for microwave irradiation-assisted lipid extraction from wet microalgae.* Bioresour Technol, 2013. **150**(0): p. 67-72.

73. Balasubramanian, S., et al., *Oil extraction from Scenedesmus obliquus using a continuous microwave system - design, optimization, and quality characterization.* Bioresour Technol, 2011. **102**(3): p. 3396-3403.

74. Kita, K., et al., *Thermal pre-treatment of wet microalgae harvest for efficient hydrocarbon recovery.* Applied Energy, 2010. **87**(7): p. 2420-2423.

75. Harun, R. and M.K. Danquah, *Influence of acid pre-treatment on microalgal biomass for bioethanol production.* Process Biochemistry, 2011. **46**(1): p. 304-309.

76. Nguyen, M.T.C., Seung Phill; Lee, Jinwon; Lee, Jae Hwa; Sim, Sang Jun, *Hydrothermal Acid Pretreatment of Chlamydomonas reinhardtii Biomass for Ethanol Production.* Journal of Microbiology and Biotechnology, 2009. **19**(2): p. 161-166.

77. Chen, P.H. and W.J. Oswald, *Thermochemical Treatment for Algal Fermentation.* Environment International, 1998. **24**(8): p. 9.

78. Spiden, E.M., et al., *Quantitative evaluation of the ease of rupture of industrially promising microalgae by high pressure homogenization.* Bioresour Technol, 2013. **140**(0): p. 165-171.

79. Grima, E.M., et al., *Recovery of microalgal biomass and metabolites: process options and economics.* Biotechnology Advances, 2003. **20**: p. 25.

80. Mendes-Pinto, M.M., et al., *Evaluation of different cell disruption processes on encysted cells of Haematococcus pluvialis: effects on astaxanthin recovery and implications for bio-availability.* Journal of Applied Phycology, 2001. **13**(1): p. 19-24.

81. Halim, R., et al., *Oil extraction from microalgae for biodiesel production.* Bioresour Technol, 2011. **102**(1): p. 178-185.

82. Sheng, J., R. Vannela, and B.E. Rittmann, *Evaluation of cell-disruption effects of pulsed-electric-field treatment of Synechocystis PCC 6803.* Environ Sci Technol, 2011. **45**(8): p. 3795-802.

83. Garoma, T. and T. Shackelford, *Electroporation of Chlorella vulgaris to enhance biomethane production.* Bioresour Technol, 2014. **169**: p. 778-783.

84. Ciudad, G., et al., *Performance of an enzymatic extract in Botrycoccus braunii cell wall disruption.* Journal of Bioscience and Bioengineering, 2014. **117**(1): p. 75-80.

85. Choi, S.P., M.T. Nguyen, and S.J. Sim, *Enzymatic pretreatment of Chlamydomonas reinhardtii biomass for ethanol production.* Bioresour Technol, 2010. **101**(14): p. 5330-5336.

86. Hetherin.Pj, et al., *RELEASE OF PROTEIN FROM BAKERS YEAST (SACCHAROMYCES-CEREVISIAE) BY DISRUPTION IN AN INDUSTRIAL HOMOGENISER.* Transactions of the Institution of Chemical Engineers and the Chemical Engineer, 1971. **49**(2): p. 142-&.

87. Carpita, N.C., *Tensile Strength of Cell Walls of Living Cells.* Plant Physiol., 1985. **79**: p. 4.

88. Lee, A.K., D.M. Lewis, and P.J. Ashman, *Force and energy requirement for microalgal cell disruption: An atomic force microscope evaluation.* Bioresour Technol, 2013. **128**(0): p. 199-206.

89. Hetherington, P.J., et al., *RELEASE OF PROTEIN FROM BAKERS YEAST (SACCHAROMYCES-CEREVISIAE) BY DISRUPTION IN AN INDUSTRIAL HOMOGENISER.* Transactions of the Institution of Chemical Engineers and the Chemical Engineer, 1971. **49**(2): p. 142-&.

90. Carpita, N.C. and D.M. Gibeaut, *Structural models of primary cell walls in flowering plants: consistency of molecular structure with the physical properties of the walls during growth.* The Plant Journal, 1993. **3**(1): p. 1-30.

91. Gibson, L.J., *The hierarchical structure and mechanics of plant materials.* J R Soc Interface, 2012. **9**(76): p. 2749-66.

92. Ortega, J.K.E., et al., *Mathematical Models for Expansive Growth of Cells with Walls.* Mathematical Modelling of Natural Phenomena, 2013. **8**(4): p. 35-61.

93. Deserno, M., *Fluid lipid membranes: From differential geometry to curvature stresses.* Chemistry and Physics of Lipids, 2015. **185**: p. 11-45.

94. Burgert, I.D., John W. C., *Micromechanics of Cell Walls*, in *Mechanical Integration of Plant Cells and Plants*, P. Wojtaszek, Editor. 2011, Springer. p. 27-52.

95. Hiller, S., D.M. Bruce, and G. Jeronimidis, *A MICRO-PENETRATION TECHNIQUE FOR MECHANICAL TESTING OF PLANT CELL WALLS.* Journal of Texture Studies, 1996. **27**(5): p. 559-587.

96. William D. Callister, J., *Materials science and engineering: an introduction*. 7th ed. ed. 2007, New York, NY: John Wiley & Sons, Inc. 721.

97. Parnes, R., *Solid Mechanics in Engineering*. 2001, West Sussex, England: John Wiley & Sons Ltd. 528.

98. Santos, H.M., C. Lodeiro, and J.-L. Capelo-Martínez, *The Power of Ultrasound*, in *Ultrasound in Chemistry*. 2009, Wiley-VCH Verlag GmbH & Co. KGaA. p. 1-16.

99. Suslick, K.S., ed. *Ultrasound: its chemical, physical, and biological effects*. 1988, VCH Publishers: New York. 336.

100. Sapozhnikov, O.A., *2 - High-intensity ultrasonic waves in fluids: nonlinear propagation and effects*, in *Power Ultrasonics*, J.A. Gallego-Juárez and K.F. Graff, Editors. 2015, Woodhead Publishing: Oxford. p. 9-35.

101. Raso, J., et al., *Influence of different factors on the output power transferred into medium by ultrasound.* Ultrasonics Sonochemistry, 1999. **5**(4): p. 157-162.

102. Loning, J.M., C. Horst, and U. Hoffmann, *Investigations on the energy conversion in sonochemical processes.* Ultrasonics Sonochemistry, 2002. **9**(3): p. 169-179.

103. Faïd, F., et al., *Comparison of ultrasound effects in different reactors at 20 kHz.* Ultrasonics Sonochemistry, 1998. **5**(3): p. 119-124.

104. Contamine, R.F., et al., *Power measurement in sonochemistry.* Ultrasonics Sonochemistry, 1995. **2**(1): p. S43-S47.

105. Lauterborn, W. and R. Mettin, *3 - Acoustic cavitation: bubble dynamics in high-power ultrasonic fields*, in *Power Ultrasonics*, J.A. Gallego-Juárez and K.F. Graff, Editors. 2015, Woodhead Publishing: Oxford. p. 37-78.

106. Louisnard, O. and J. González-García, *Acoustic Cavitation*, in *Ultrasound Technologies for Food and Bioprocessing*, H. Feng, G.V. Barbosa-Cánovas, and J. Weiss, Editors. 2011, Springer. p. 13-64.

107. Louisnard, O. and J. González-García, *Acoustic Cavitation.* 2011: p. 13-64.

108. Kimura, T., et al., *Standardization of ultrasonic power for sonochemical reaction.* Ultrasonics Sonochemistry, 1996. **3**(3): p. S157-S161.

109. Luo, J., Z. Fang, and R.L. Smith Jr, *Ultrasound-enhanced conversion of biomass to biofuels.* Progress in Energy and Combustion Science, 2014. **41**: p. 56-93.

110. Yamamoto, K., et al., *Effect of ultrasonic frequency and power on the disruption of algal cells.* Ultrasonics Sonochemistry, 2015. **24**: p. 165-171.

111. Petosic, A., D. Svilar, and B. Ivancevic, *Comparison of measured acoustic power results gained by using three different methods on an ultrasonic low-frequency device.* Ultrasonics Sonochemistry, 2011. **18**(2): p. 567-576.

112. Mason, T.J., et al., *DOSIMETRY IN SONOCHEMISTRY - THE USE OF AQUEOUS TEREPHTHALATE ION AS A FLUORESCENCE MONITOR.* Ultrasonics Sonochemistry, 1994. **1**(2): p. S91-S95.

113. Bischoff, H.W. and H.C. Bold, *Some Soil Algae From Enchanted Rock and Related Algal Species*, in *Phycological Studies IV*. 1963, University of Texas, Austin. p. 1-95.

114. ATCC. *ATCC Medium: 5 Sporultation Agar*. 2014 [cited 2014; Available from: https://www.atcc.org/~/media/82DFAF3DA622404FA2137FB49F5E22E1.ashx.

115. ASTM, *Standard Test Method for: Automated Analyses of Cells - the Electrical Sensing Zone*. 2002, ASTM International. p. 4.

116. Saltelli, A., et al., *Global Sensitivity Analysis. The Primer*. 2008, England: John Wiley & Sons, Ltd. 292.

117. Ott, R.L. and M. Longnecker, *Probability and Probability Distributions*, in *An Introduction to Statistical Methods and Data Analysis*. 2010, Brooks/Cole: Australia. p. 140-219.

118. Darzins, A., P. Pienkos, and L. Edye, *Current Status and Potential for Algal Biofuels Production*, B.T. 39, Editor. 2010, International Energy Agency. p. 14-46.

119. Kanaga, K., et al., *Multi-objective optimization of media nutrients for enhanced production of algae biomass and fatty acid biosynthesis from Chlorella pyrenoidosa NCIM 2738.* Bioresource Technology, 2016. **200**: p. 940-950.

120. Sueoka, N., *Mitotic replication of deoxyribonucleic acid in Chlamydomonas reinhardi.* Proc Natl Acad Sci U S A, 1960. **46**(1): p. 83-91.

121. Bold, H.C., *The Morphology of Chlamydomonas chlamydogama, Sp. Nov.* Bulletin of the Torrey Botanical Club, 1949. **76**(2): p. 101-108.

122. Claus, G.W. and D. Blakwill, in *Understanding Microbes: A Laboratory Textbook for Microbiology*. 1989, W.H. Freeman. p. 203-204.

123. Hadj-Romdhane, F., et al., *Development and validation of a minimal growth medium for recycling Chlorella vulgaris culture.* Bioresource Technology, 2012. **123**: p. 366-374.

124. Gorman, D.S. and R.P. Levine, *Cytochrome F and Plastocyanin - thier sequence in photosynthetic electron transport chain of Chlamydomonas Reinhardi.* Proceedings of the National Academy of Sciences of the United States of America, 1965. **54**(6): p. 1665-1669.

125. Corrigan, R., J. Hawken, and B. Elder. *Simple Miracle Grow Isolation Media*. [Video] 2013; Available from: https://www.youtube.com/watch?v=avrpX2jlGbU.

126. Lee, K., et al., *Isolation and screening of microalgae from natural habitats in the midwestern United States of America for biomass and biodiesel sources.* Journal of Natural Science, Biology, and Medicine, 2014. **5**(2): p. 333-339.

127. Rice, E.W., et al., eds. *Standard Methods for the Examination of Water and Wastewater*. 22 ed. 2012, American Water Works Association. 1496.

128. Chiu, Y.-C., et al., *Alkaline and ultrasonic pretreatment of sludge before anaerobic digestion.* Water Science and Technology, 1997. **36**(11): p. 155-162.

129. Ott, R.L. and M. Longnecker, *Multiple Comparisons*, in *An Introduction to Statistical Methods and Data Analysis*. 2010, Brooks/Cole: Australia. p. 451-498.

130. Wood, M.A., R.C. Everroad, and L.M. Wingard, *Measuring Growth Rates in Microalgal Cultures*, in *Algal Culturing Techniques*, R.A. Andersen, Editor. 2005, Elsevier University Press: Burlington, MA. p. 269-285.

131. Griffiths, M.J., et al., *Interference by pigment in the estimation of microalgal biomass concentration by optical density.* Journal of Microbiological Methods, 2011. **85**(2): p. 119-123.

132. Metcalf & Eddy, I., *Anaerobic Suspended and Attached Growth Biological Treatment Processes*, in *Wastewater Engineering: Treatment and Reuse*, G. Tchobanoglous, F.L. Burton, and H.D. Stensel, Editors. 2003, McGraw Hill: Boston. p. 983-1034.

133. Ensminger, D. and L.J. Bond, *Applications of High-Intensity Ultrasonics: Basic Mechanisms and Effects*, in *Ultrasonics: Fundamentals, Technologies, and Applications*. 2011, CRC Press. p. 459-494.

134. Gao, S., et al., *Inactivation of microorganisms by low-frequency high-power ultrasound: 2. A simple model for the inactivation mechanism.* Ultrasonics Sonochemistry, 2014. **21**(1): p. 454-460.

135. Tzanakis, I., et al., *Characterizing the cavitation development and acoustic spectrum in various liquids.* Ultrasonics Sonochemistry, 2017. **34**: p. 651-662.

136. Spiden, E.M., et al., *Critical analysis of quantitative indicators of cell disruption applied to Saccharomyces cerevisiae processed with an industrial high pressure homogenizer.* Biochemical Engineering Journal, 2013. **70**: p. 120-126.

137. Wileman, A., A. Ozkan, and H. Berberoglu, *Rheological properties of algae slurries for minimizing harvesting energy requirements in biofuel production.* Bioresource Technology, 2012. **104**: p. 432-439.

138. de La Rochebrochard, S., et al., *Sonochemical efficiency dependence on liquid height and frequency in an improved sonochemical reactor.* Ultrasonics Sonochemistry, 2012. **19**(2): p. 280-285.

139. Maisonhaute, E., et al., *Surface acoustic cavitation understood via nanosecond electrochemistry. Part III: shear stress in ultrasonic cleaning.* Ultrasonics Sonochemistry, 2002. **9**(6): p. 297-303.

140. Moholkar, V.S., S. Rekveld, and M.C.G. Warmoeskerken, *Modeling of the acoustic pressure fields and the distribution of the cavitation phenomena in a dual frequency sonic processor.* Ultrasonics, 2000. **38**: p. 5.

141. Hori, T., R.E. Norris, and M. Chihara, *STUDIES ON THE ULTRASTRUCTURE AND TAXONOMY OF THE GENUS TETRASELMIS (PRASINOPHYCEAE) .1. SUBGENUS TETRASELMIS.* Botanical Magazine-Tokyo, 1982. **95**(1037): p. 49-61.